G. I. Zárate Garnica

Analysis of shear transfer mechanisms in concrete members without shear reinforcement based on kinematic measurements

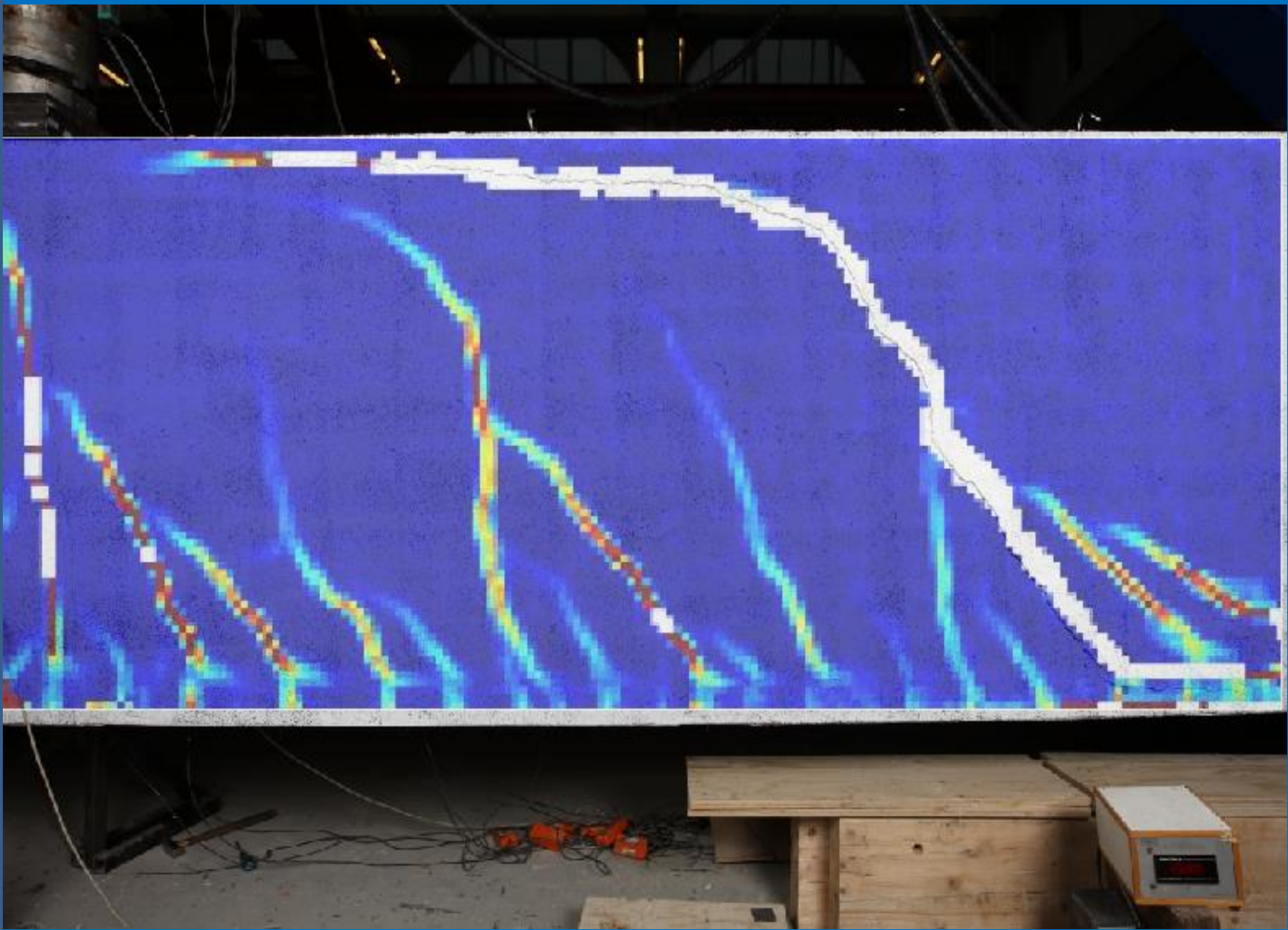

TU Delft

Analysis of shear transfer mechanisms in concrete members without shear reinforcement based on kinematic measurements

By

Gabriela I. Zárate Garnica

in partial fulfillment of the requirements for the degree of

Master of Science
in Structural Engineering

at the Delft University of Technology,
to be defended publicly on Monday, October 15, 2018, at 4:00 PM.

Supervisor:	Dr. ir. Y. Yang,	TU Delft
Thesis committee:	Prof. dr. ir. D.A. Hordijk,	TU Delft
	Dr. ir. M.A.N. Hendriks,	TU Delft

Contents

Preface

This master thesis is written as a partial fulfillment of the requirements for the degree of Master of Science in Structural Engineering, with a specialization in Concrete Structures at Delft University of Technology It represents the culmination of the two most challenging years in my life, but also the most enriching. It has been a constant learning experience not only in the professional but also in my personal life.

First, I would like to thank my daily supervisor, Yuguang Yang, for his help, patience, and guidance throughout the development of this project. I would like to express my sincere gratitude for the opportunity to work as an assistant in the laboratory of concrete structures and for trusting in my work. The last eight months have provided me with a wonderful opportunity to work in an international environment, to learn new skills and to apply concepts.

I would also like to thank the other members of the committee. I would like to thank Dick Hordijk for his support and encouragement. I would like to thank Max Hendriks for his engagement and interest in the project, especially for the valuable comments and remarks.

I would like to acknowledge the Alliance for training and research in Infrastructure for the development of Mexico (Formación e Investigación en Infraestructura para el Desarrollo de México, FiiDEM) and the Science and Technology Council of Mexico (Consejo Nacional de Tecnología, CONACYT) for the financial support throughout my Master Program.

Also, I would like to thank my colleagues in the lab who made this period enjoyable. Thanks to Albert Bosman for the support during the tests and for making lunchtime an entertainable moment. Thanks to Ulric Celada for introducing me to the field of Digital Image Correlation.

Thanks to my Mexican family in Delft, without you I would have not survived the first winter, thanks for the Mexican food and the long conversations. To my friends back home, thanks for the constant encouragement. Thanks to Gina for listening when I was sad and troubled, for lifting me up and believing in me when I didn´t even believe in myself, but most of all thanks for all the happy times.

Finally, I want to thank my dad and mom, thanks for supporting me in every decision I have made in my life. Thank you for always being there regarding the distance, for the daily text messages and the long calls. I cannot thank you enough for all the things you have done for me. I love you.

Gabriela Irene Zárate Garnica
Delft, October 2018

Abstract

Shear failure is one of the most critical failure modes of reinforced concrete members, especially for those without shear reinforcement. Despite the extensive research programs in the last decades, there is still no general agreement on a rational theory to assess their shear capacity. In the recent years, researchers have focused on developing mechanical models for shear design that are based on a predefined crack pattern and kinematics assuming that the shear force can be transferred through a critical shear crack by various shear transfer mechanisms. These mechanical models need to be validated by detailed kinematic measurements taken from experiments. This information could not be acquired before, however, in the recent years, new measurement technology has developed quickly, amongst others, Digital Image Correlation (DIC) provides new opportunities to obtain the crack pattern and kinematics through the displacement field of the whole surface of the target specimen.

In this research, the possibility of using DIC measurements to apply a detailed analysis on the contribution of the shear transfer mechanisms (uncracked concrete, aggregate interlock, dowel action, and arch action) is explored in order to obtain a better understanding of the shear failure process.

The analysis is based on ten representative tests on reinforced concrete beam specimens with a height of 1200 mm. The tests are selected from an experimental program designed to study the shear behaviour of reinforced concrete slab strips without shear reinforcement. A new algorithm is developed to automatically determine the contributions of the different shear transfer mechanisms along a crack from the displacement field obtained by DIC measurements. A comparison between the experimental results and the sum of the calculated contributions yield to a reasonable agreement, with an error of 40% when the shear failure is presented just after the formation of the flexural shear crack.

With the help of the new algorithm, new insights on the three different shear failure modes observed in the experiments (flexural shear failure, shear compression, and dowel failure) are discussed. Flexural shear failure is attributed to the loss of aggregate interlock when a sudden increase of the shear displacement of the critical shear crack is observed. However, such decrease occurs earlier before the actual failure occurs. Therefore, the actual shear failure mechanism should be studied at an earlier stage. In a shear compression failure, the arch action turns out to be dominating. For members with large depth and exceptionally low reinforcement ratio (< 0.3%), a different failure mode may occur: dowel failure. Which is defined by the opening of the secondary branch of a major flexural crack along the tensile reinforcement. In the three failure modes, the importance of the crack opening in vertical and longitudinal direction is demonstrated, since the increase of them directly result in the drop of shear force that can be transferred through aggregate interlock.

Finally, the results are a valuable input to further improve the Critical Shear Displacement theory. It is suggested that the assumed simplified crack profile is modified to a crack with an angle between 60° to 70° to represent more accurately the results and to allow for larger shear displacements. It is demonstrated that an increase of the shear displacement Δ is critical to triggering the shear flexural failure as proposed

by this theory and the actual value of the critical shear displacement is larger than the proposed value based on regression analysis.

Keywords: shear, concrete members, without shear reinforcement, DIC, kinematics, shear transfer mechanisms, critical shear displacement theory, aggregate interlock.

Notation

Abbreviations

CSDT	Critical Shear Displacement theory
DIC	Digital Image Correlation, a photogrammetry measurement technique to track the full deformation of a surface
LVDT	Linear Variable Differential Transformer, a sensor used to measure deformations in a single direction

Roman Upper Case

A_x, A_y	projected contact areas for a unit crack length, which are functions of the normal and tangential displacement (n,t) of the two crack faces
D	aggregate size
D_{max}	maximum aggregate size
E_c	elastic modulus of concrete
N_{ai}	resultant compressive force component carried by aggregate interlock
N_c	resultant compressive force component carried by uncracked concrete
P	applied load
P_{cr}	load level at which the critical inclined crack opens
P_u	maximum load level
P_y	load level at which yielding of the reinforcement is observed. It equals to P_u when no other failure occurred after a further increase of the deflection
R	distance from the center of the crack to the point with computed displacements
V	shear force
V_{ai}	shear force carried by aggregate interlock
V_c	shear force component carried in the uncracked concrete compression zone
V_{cr}	inclined cracking load, the shear force needed to open the critical inclined crack
V_d	shear force component carried by the dowel action
V_u	maximum shear force

Roman Lower Case

a	distance from the center of the support to the center of the loading point
b	width of the structural member
c	thickness of the concrete cover
d	effective height of the tested specimens
f_c	concrete compressive strength
$f_{c,cube}$	concrete compressive cube strength determined by testing concrete cubes with dimensions 150×150×150 [mm^3], casted during the casting of the specimens
f_{ct}	concrete tensile strength
k_c	slope of the stress line to distribute localized load/deformation to the whole section
h	total height of the tested specimen
$l_{cr,m}$	mean crack spacing of the major cracks
n	normal displacement along the crack profile
n_e	elastic stiffness ratio between E_s and E_c
s_{cr}	crack height after it is stabilized
t	tangential displacement along the crack profile
w	crack opening in the longitudinal direction
w_b, w_m	crack opening in the longitudinal direction at reinforcement and mid-height level
x_0	distance between the center of the support and the root of the crack profile
$x_{cr,b}$	distance between the shear crack at the bottom reinforcement level and the center of the support
$x_{cr,m}$	distance between the shear crack at the center line of the specimen and the center of the support.
x_{cr0}	distance between the center of the support and the root of the critical crack
z	length of the internal lever arm
z_c	height of the uncracked compressive zone

Greek Upper Case

Δ	relative vertical displacement of the crack faces
Δ_b, Δ_m	relative vertical displacements of the crack face at the reinforcement and mid-height level
Δ_{cr}	critical shear displacement of the crack faces at the level of the tensile reinforcement for the opening of the dowel crack

Greek Lower Case

α	crack angle
α_{cr}	crack angle of the critical shear crack
α_m	average angle of the major cracks
β	angle of direct compressive strut, from the point load to the support
ε_{xx}	strain of the cross-section in the longitudinal direction
ϕ	diameter
μ	coefficient of friction
ρ	reinforcement ratio of the specimens
ρ_k	relative aggregate volume fraction
σ	normal stress
σ_{pu}	crushing strength of the cement matrix under confinement
τ	shear stress

1 Introduction

1.1. Background and motivation

Shear failure is considered as one of the most critical failure modes in concrete structures, especially for members without shear reinforcement. In contrast to other failure modes, shear failure occurs without any warning and can be defined as a brittle failure that can lead to catastrophic events. Thus, the importance of understanding its behavior.

The shear strength of concrete members with and without shear reinforcement has always been a topic of interest, this has led to extensive experimental and theoretical research. There are some well-established theories to assess the shear capacity of members with transverse reinforcement such as the truss-analogy (Mörsch, 1909) and the Compression Field Theory (Vecchio & Collins, 1986; Bentz et al., 2006). On the contrary, for members without transverse reinforcement, there is still no general agreement on a rational theory. Some researchers have developed different theories to assess the shear capacity, however, most of them are empirical formulators (Zsutty, 1968; Bentz, 2005). In recent years, researchers such as Muttoni & Fernández Ruiz (2008); Mihaylov et al. (2013) and Yang (2014), have put special effort in understanding the shear transfer mechanisms and in developing mechanical models for shear design. These mechanical models are usually based on the interpretation of a crack pattern after failure and on measured kinematics before it happens using traditional measuring techniques such as LVDTs that fail in tracking the full development of the failure process. The developing of new measuring techniques, such as the Digital Image Correlation (DIC), provide a new insight to this problem since this tool allows having detailed information about the evolution of the cracks even an instant before failure. With DIC, information about the kinematics and crack pattern during the failure process can lead to a better understanding of the shear failure process.

This Master's Thesis will be based on the results of ten representative tests on reinforced beams selected from an experimental program designed to study the shear behavior of reinforced concrete slab strips without shear reinforcement. The main objectives of this thesis are to explain the observed failure modes based on the crack patterns and kinematics obtained from the DIC results concerning the role of the various shear transfer mechanisms and to give recommendations to improve the Critical Shear Displacement theory.

1.2 Objectives

The goals of this master's thesis are to explain the failure modes observed on an experimental program on concrete members without shear reinforcement based on Digital Image Correlation (DIC) results regarding the role of the different shear transfer mechanisms and to check some of the assumptions made in the Critical Shear Displacement theory. From these goals the following research questions arise:

- What is the contribution of each of the shear transfer mechanism? Which one is governing?
- Can the observed failure modes be explained with the analysis of the shear transfer mechanisms?
- How can the obtained insights be implemented to improve the available shear models?

1.3 Research Methodology

This research is based on the results of ten representative tests on reinforced concrete beam specimens selected from an experimental program designed to study the shear behavior of reinforced concrete slab strips without shear reinforcement. The program is an extension of the previous study reported in Yang (2016) on the transition between the flexural and shear failure modes.

Besides the traditional measuring techniques (LVDTs), DIC measurements were implemented for which several photographs were taken throughout the development of each of the test. The main results of this research were obtained by post-processing the data of the DIC using Matlab scripts.

To accomplish the research goal of explaining the observed failure modes in the experimental program, a new algorithm is developed to calculate the contribution of the shear transfer mechanisms based on the DIC measurements, which provide the crack pattern and the crack kinematics that are used as an input to compute the calculated shear transfer by the different actions. These steps or units are schematized in the following flowchart:

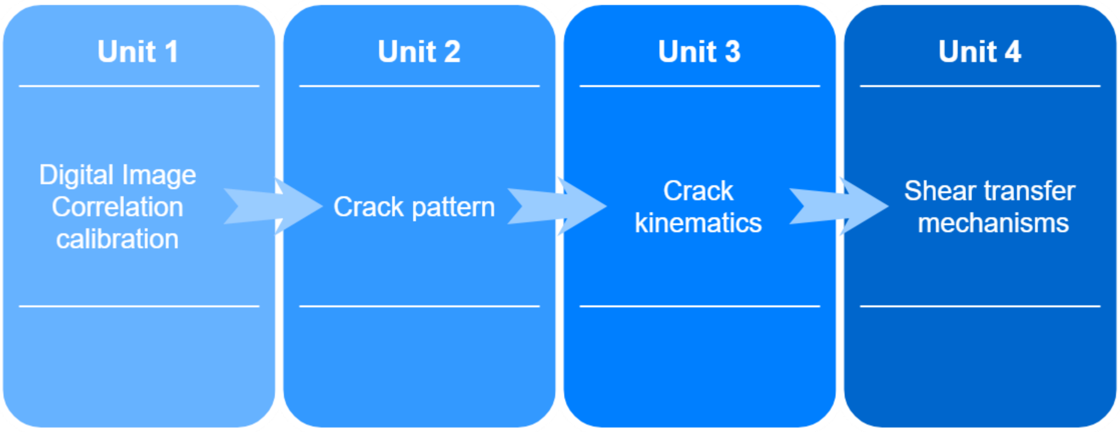

Fig. 1.3.1 Schematic diagram of the methodology

In Unit 1 the implementation and calibration of the DIC technique are explained. Then, in Unit 2, the crack pattern is identified from the distribution of the strains obtained using the DIC. Once the crack pattern and the angle of the cracks are found, the crack kinematics is obtained relating the displacements, this procedure is explained in Unit 3. Next, in Unit 4 the methodology followed to calculate the contribution of the shear transfer mechanisms is given.

1.4 Outline of the thesis

This thesis mainly contributes to gaining a more comprehensive understanding of the shear failure process through the kinematics that can be obtained using Digital Image Correlation in combination with an experimental study on concrete structures without shear reinforcement. A brief description of the organization of this thesis is provided below.

Chapter 2 is dedicated to reviewing the background knowledge on the different shear transfer mechanisms and to a literature review on the available shear mechanical models. It also contains an explanation of the fundamental principles of Digital Image Correlation.

In Chapter 3, the selected tests are presented. It also contains a summary of the properties of the specimens and the DIC test set up.

The objective of Chapter 4 is to explain the methodology followed to develop the algorithm that determines the contributions of the different shear transfer mechanisms. To do this, the methodology is divided into four units that include the calibration of the DIC results, the identification of the crack pattern, the calculation of the crack kinematics and finally the co.

Chapter 5 presents the results of cracking patterns and crack kinematics. On the basis of these results, an analysis of shear transfer mechanisms is performed where the governing shear transfer action is identified.

Chapter 6 provides recommendations to improve the Critical Shear Displacement theory based on the results in Chapter 5.

Finally, the main conclusions of this project and recommendations for further research are presented in Chapter 7.

2 Literature Review

This chapter provides a description of the shear transfer mechanisms and some of the available mechanical models to assess the shear capacity of reinforced concrete members without shear reinforcement. Finally, a revision of the fundamentals of Digital Image Correlation is given.

2.1 Shear transfer mechanisms

An effective technique to understand the forces acting on a concrete element is to draw a free body diagram along a certain section and ensure that the external and internal forces are in equilibrium.

Regarding the shear strength of reinforced concrete members without shear reinforcement, it has been generally accepted that if a free body diagram is taken from a beam along a flexural crack, the shear force can be transferred by the following four mechanisms (Fig. 2.1.1), as summarized by ACI-ASCE Committee 445 on Shear and Torsion:

1. Shear stress in the uncracked concrete zone
2. Aggregate interlock caused by the tangential displacement of the crack faces
3. Residual tensile stress occurring at limited normal opening of the cracks
4. Dowel action caused by the longitudinal bars

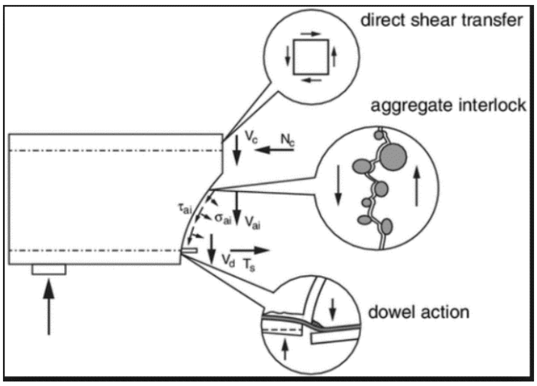

Fig. 2.1.1 Free body diagram with three shear transfer mechanisms (Yang, Walraven, & Den Uijl, 2016)

In addition to the shear transfer mechanisms list above, when the shear can be directly transmitted to the support by an inclined strut, arch action develops.

In the following sections, a description of these four mechanisms will be given. Information about the constitutive laws and their theoretical backgrounds will be presented.

2.1.1 Shear in the uncracked concrete zone

The uncracked concrete zone in a cracked concrete section contributes to the shear resistance, however, its contribution is limited to the depth of the compression zone of the cross-section. In a relatively slender beam, the shear contribution due to the uncracked compression zone becomes relatively small due to the small depth of the compression zone. (Transportation Research Board, 2006)

As long as a concrete cross section remains uncracked, the stress distribution will follow the elastic theory. Simplifications can be done, depending on whether the height of the compression zone varies or not. When the height of the compression zone is assumed to be more or less constant, the simplifications allow considering the boundary conditions between two flexural cracks. In the early 1900´s, Mörsch (1909) derived the shear stress contribution for reinforced concrete beams containing flexural cracks. Mörsch predicted that the shear stress reaches its maximum value at the neutral axis and then remains constant from the neutral axis to the flexural reinforcement level. Above the neutral axis, a parabolic stress distribution was assumed, see Fig. 2.1.2. Researchers like Taylor (1974), Fenwick & Pauley (1968) and Sherwood et al. (2007) have derived more complex expressions for the shear stress distribution curve but Mörsch´s formulation has proven to be accurate enough.

The shear force carried by the concrete compressive zone can be expressed by:

$$V_c = \frac{2}{3}\frac{z_c}{z}V \tag{2.1}$$

with

z : the lever arm equal

z_c : the height of the uncracked compression zone

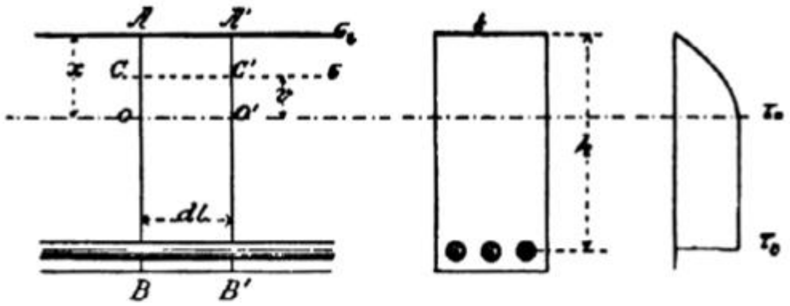

Fig. 2.1.2 Shear stress distribution (Mörsch, 1909)

When the variation of the lever arm is governing, the shear force is transfer by the mechanism denoted as ‘Arching action’. In this case, the flow of forces can be modeled using the Strut and Tie method, which was proposed in the late 1980’s (Marti, 1985; Schlaich et al.,1987). This method can describe the capacity of beams failing in shear compression, which is governing in members with *a/d* ratios less than 3.0. In this failure mode, after the critical crack has developed, an increase of the shear strength is observed since shear can be transmitted directly to the support by an inclined compressive strut in the uncracked concrete part and the rebar can be considered as a tension tie. The uncracked concrete part and the reinforcement form an arch-like structure, like the one illustrated in Fig. 2.1.3. The vertical component of the force is considered as the contribution for the uncracked concrete part.

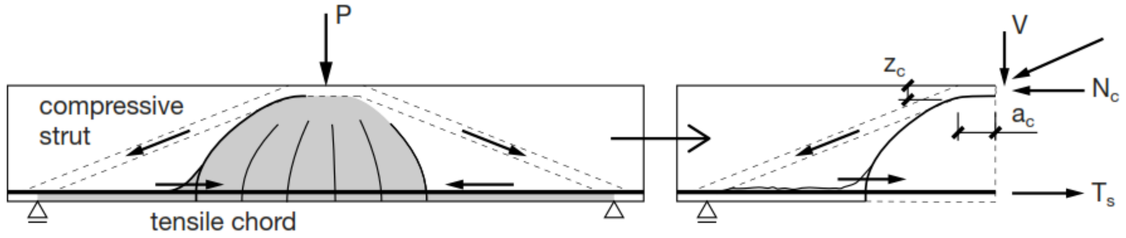

Fig. 2.1.3 Arch-like structure

2.1.2 Residual tensile strength

The residual tensile strength of concrete consists of the capacity to transfer tensile stresses across cracks. Concrete can transmit tensile stress when the crack widths are smaller than 0.1 mm. The relationship between tensile stress and crack widths was first investigated by Evans & Marathe (1968). The importance of the residual capacity to transfer tensile stress was recognized in the Fictitious Crack Model developed by Hillerborg et. al (1976). Since then, research has been carried out to study the tension softening behaviour of concrete. A widely accepted tensile stress – crack width relationship is the exponential relationship proposed by Hordijk (1991).

Regarding the contribution of the residual tensile strength to shear behaviour, its role is not widely agreed yet. In models based on fracture mechanics such as Jenq and Shah's model (1990) or Gustafsson and Hillerborg's model (1988), the contribution of the tensile stress along the crack plays a major role. However, according to some researchers like Reineck (1991), the tensile stress in shear cracks is very limited, since its presence is restricted to the vicinity of the crack tips of the inclined or flexural cracks. When the crack opening is small, the contribution is significant. However, in large concrete members, the contribution of the crack tip tensile stresses is minimal due to the large crack widths that occur before the failure of such members (Transportation Research Board, 2006).

Yang (2014) mentions that the contribution of the tension softening force to the shear resistance is about 10 times smaller than the aggregate interlock effect, thus in this thesis, it is neglected when the crack width is larger than 0.1 mm.

2.1.3 Dowel action

One of the principal types of shear transfer mechanisms is the so-called dowel action. The dowel force is a result of the interaction between the reinforcing bars and the surrounding concrete when the reinforcing bars resist forces perpendicular to their axis. Walraven (1978) described the dowel deflection (Δ) as the total distance between the axis of the un-deformed parts of the bar at both sides of the crack. (Fig. 2.1.4) The total deflection is the result of the deformation of the concrete surrounding the bar and the deformation of the bar over the free length (w).

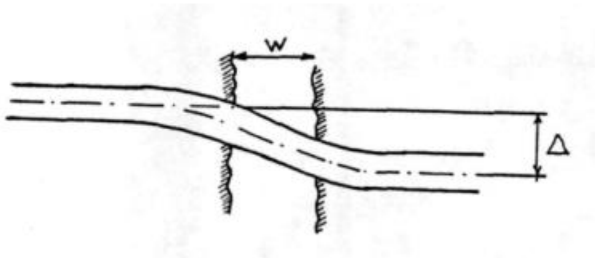

Fig. 2.1.4 Dowel deflection (Walraven J., 1978)

Paulay et al. (1974) identified three different mechanisms for the deformation of the bar occurring over the free length (Fig. 2.1.5):

- Bending: the capacity of this mechanism is limited by the formation of plastic hinges in the bar
- Shear: the load is transferred by pure shear
- Kinking: if there is a considerable shift between the two main bar axis, the axial force in the locally derived part results in a component perpendicular to the bar axis.

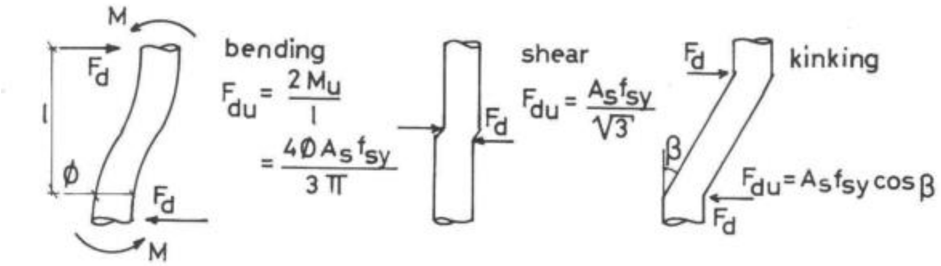

Fig. 2.1.5 Mechanisms of shear transfer over the free length according to Paulay *et al.* (1974)

There are two possible failure modes under the dowel action mechanism:

1. Failure Mode I: Yielding of the bar and concrete crushing under the dowel
2. Failure Mode II: Concrete splitting

According to Vinitzeleou & Tassios (1986), the concrete cover (c) is the main parameter upon the failure modes depend. When the concrete cover is greater than 6 to 7 times the bar diameter, the failure occurs due to failure mode I. When the concrete cover is smaller (which is the case of reinforced concrete beams), the governing failure mechanism is the concrete splitting, the splitting cracks can be present either at the faces of the section or at the bottom.

2.1.3.1 Empirical Formulas

Many researchers have carried out experiments (Fig. 2.1.6) to investigate the dowel strength when the failure mode is due to the splitting of concrete, thus only empirical formulas are available. The main parameters considered in most of these formulations are the bar diameter, concrete strength and concrete cover. Some of the expressions proposed for the prediction of the dowel force (V_d) are:

1 Krefeld and Thurston (1966)

$$V_d = b\sqrt{f_c}\left[1.30\left(1+\frac{180\rho}{\sqrt{f_c}}\right)c+d\right]\frac{1}{\sqrt{(x_1/d)}} \quad \textbf{(2.2)}$$

where

ρ : is the percentage of reinforcement

c : is the concrete cover

d : is the effective depth

x_1 : is the distance of the diagonal crack from the beam support

f_c : is the concrete compressive strength

2 Taylor (1969)

$$V_{d\max} = 9.1 + 0.0001\left[\sum (c_s + c_i)\right]^2 f_{ct} \quad \textbf{(2.3)}$$

where

c_s : is the side cover

c_i : is the horizontal distance between consecutive bars

f_{ct} : is the concrete tensile strength

The relationship between the dowel deflection and the load is defined by the following curve:

$$V_d = 1.55 V_{d\max} \Delta^{0.25} \quad \textbf{(2.4)}$$

3 Baumann and Rüsch (1970)

$$V_{d\max} = 1.64 b_n \phi \sqrt[3]{f_c} \quad \textbf{(2.5)}$$

where

b_n : is the net width of the beam $(b - n\phi)$

The relationship between Δ and V_d , for this set of experiments is:

$$V_d = \frac{\Delta}{0.08} V_{d\max}, \Delta < 0.08mm \quad \textbf{(2.6)}$$

4 Houde and Mirza (1974)

$$V_{d\max} = 37 b_n \sqrt[3]{f_c} \quad \textbf{(2.7)}$$

The load-dowel deflection relation is given by:

$$V_d = 78 \Delta V_{d\max} \quad \textbf{(2.8)}$$

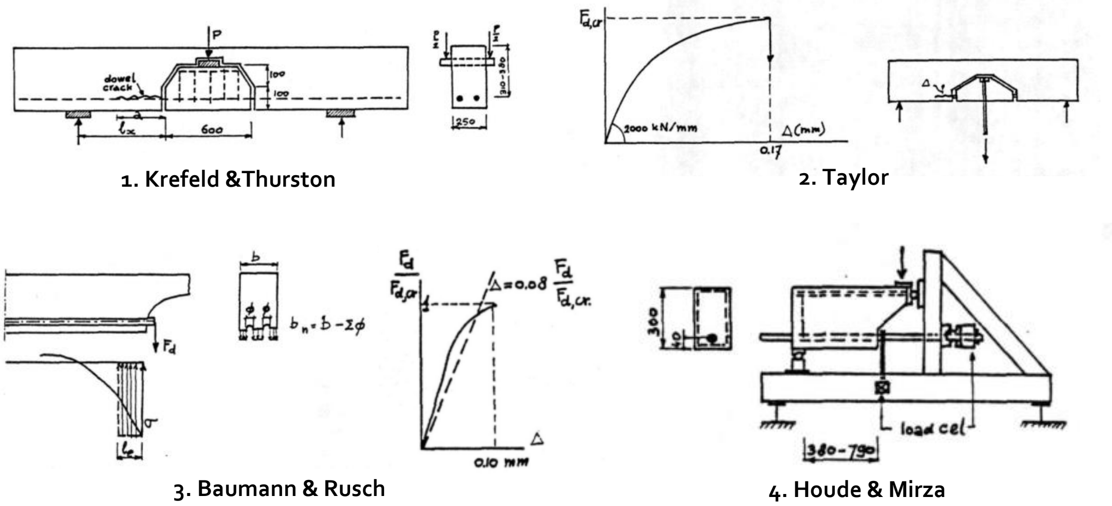

Fig. 2.1.6 Test experiments (Walraven J., 1978)

The typical results from Baumann and Rüsch (1970) experimental research are shown in Fig. 2.1.7. It can be observed that during the experiments the post-peak behavior was investigated. The results show that large plastic shear displacements can be expected after the peak load, which evolves into the splitting crack approximating to the support at the reinforcement level.

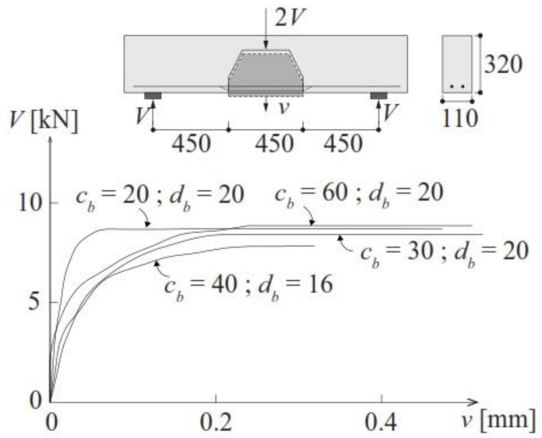

Fig. 2.1.7 Test results from Baumman and Rüsch (1970)

In this thesis, large shear displacements are expected similar to the results found by Baumman and Rüsch (1970) due to the dimensions of specimens (1200 mm of height), thus their equation will be used to calculate the contribution from dowel action.

2.1.4 Aggregate Interlock

Aggregate interlock is defined as the effect that allows developing shear and compressive stresses caused by the tangential and normal displacements between two cracked surfaces due to the protrude aggregates in the concrete.

Some researchers have proposed models to calculate the aggregate interlock stresses based on the relative displacements of the surface of the cracks ((Walraven J. C., 1981) and (Gambarova & Karakoc, 1983)). The model proposed by Walraven (1981) reflects the physical background of aggregate interlock, since it allows relating the opening (w) and slipping (Δ) between to cracked surfaces to the normal (σ) and shear (τ) stresses transferred along the crack (Fig. 2.1.8), thus this model will be used for the development of this thesis.

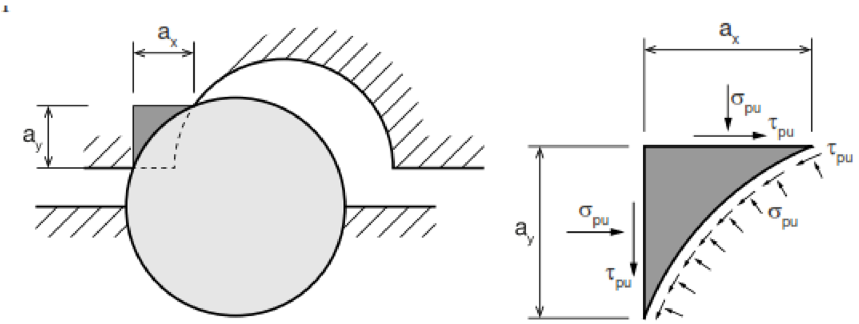

Fig. 2.1.8 Aggregate interlock scheme mechanisms (Walraven J. C., 1981)

The compression (N_{ai}) and shear (V_{ai}) forces acting at the crack can be calculated by integrating the stresses along the crack:

$$\begin{pmatrix} \sigma \\ \tau \end{pmatrix} = \sigma_{pu} \begin{pmatrix} A_y + \mu A_x \\ A_x - \mu A_y \end{pmatrix} \qquad \textbf{(2.9)}$$

where

σ_{pu} : is the compressive strength of the cement matrix

$\sigma_{pu} = 6.39 f_c^{0.56}$

μ : is the coefficient of friction

D : is the diameter of the aggregate

ρ_k : is the relative aggregate volume fraction

A_x, A_y : are the projected contact areas between the surfaces of the aggregates and the cement matrix, which are functions of the normal and tangential displacements in both axes (n,t) of the crack faces. The expressions to obtain the projected areas, depend on the magnitude of the normal (n) or tangential (t) displacements and are:

Case 1, normal situation when $t < n$:

$$A_y = \int_{\frac{n^2+t^2}{t}}^{D_{\max}} p_k \frac{4}{\pi} F\left(\frac{D}{D_{\max}}\right) G_1(n,t,D)dD$$

$$A_x = \int_{\frac{n^2+t^2}{t}}^{D_{\max}} p_k \frac{4}{\pi} F\left(\frac{D}{D_{\max}}\right) G_2(n,t,D)dD$$

Case 2, when $t > n$:

$$A_y = \int_{2n}^{\frac{n^2+t^2}{t}} p_k \frac{4}{\pi} F\left(\frac{D}{D_{\max}}\right) G_3(n,t,D)dD + \int_{\frac{n^2+t^2}{t}}^{D_{\max}} p_k \frac{4}{\pi} F\left(\frac{D}{D_{\max}}\right) G_1(n,t,D)dD$$

$$A_x = \int_{2n}^{\frac{n^2+t^2}{t}} p_k \frac{4}{\pi} F\left(\frac{D}{D_{\max}}\right) G_4(n,t,D)dD + \int_{\frac{n^2+t^2}{t}}^{D_{\max}} p_k \frac{4}{\pi} F\left(\frac{D}{D_{\max}}\right) G_2(n,t,D)dD$$

with

Aggregate size distribution as:

$$F(D) = 0.532\left(\frac{D}{D_{\max}}\right)^{0.5} - 0.2122\left(\frac{D}{D_{\max}}\right)^{4} - 0.0722\left(\frac{D}{D_{\max}}\right)^{6} - 0.0362\left(\frac{D}{D_{\max}}\right)^{8} - 0.0252\left(\frac{D}{D_{\max}}\right)^{10}$$

$$G_1(n,t,D) = D^{-3}(\sqrt{D^2-(n^2+t^2)}\,\frac{t}{\sqrt{n^2+t^2}}u_{\max} - nu_{\max} - u^2{}_{\max})$$

$$G_2(n,t,D) = D^{-3}\left\{\begin{array}{l}(t-\sqrt{D^2-(n^2+t^2)}\,\frac{n}{\sqrt{n^2+t^2}}u_{\max} + (u_{\max}+n)\sqrt{\frac{D^2}{4}-(n^2+t^2)} \\ -n\sqrt{\frac{D^2}{4}-n^2} + \frac{D^2}{4}\arcsin\left(\frac{w+u_{\max}}{D/2}\right) - \frac{D^2}{4}\arcsin\left(\frac{2n}{D}\right)dD\end{array}\right\}$$

$$G_3(n,t,D) = D^{-3}\left(\frac{D}{2}-n\right)^2$$

$$G_4(n,t,D) = D^{-3}\left(\frac{\pi}{8}D^2 - w\sqrt{\frac{D^2}{4}-n^2} - \frac{D^2}{4}\arcsin\frac{2n}{D}\right)$$

Additionally, accounting for the tension softening effect, the experimental research carried out by Keuser and Walraven (1989) showed that when the tangential displacement is smaller than the crack width and the crack width (n) is smaller than 0.2mm, it is possible to neglect the influence of aggregate interlock on the tension softening relationship.

The complexity of the integration of Walraven’s formulation makes it difficult to solve without numerical procedures, which cannot be implemented in the engineering practice. In most cases, researches proposed simplified formulations as in Reineck (1991), Vecchio & Collins (1986) and Yang (2014). In this thesis, the integration of the stresses is performed with the help of a Matlab script.

2.2 Mechanical models

A simple and widely accepted theory for the prediction of the shear strength of reinforced concrete members without shear reinforcement does not exist yet. There are several models that have been developed. Nevertheless, many of these theories are empirical formulas based on the available experimental data. In the last decades, researchers have focused on developing physical models that account for the contribution of the different transfer mechanism assuming a given crack pattern and kinematics at failure. Some of these physical models are the so-called "Tooth model" developed by Kani (1964) and Reineck (1991), the Critical Shear Crack theory by Muttoni & Fernández Ruiz (2008), the Two-parameter kinematic theory based on the deformation patterns of deep beams introduced by Mihaylov et al. (2013) and the Critical Shear Displacement theory by Yang (2014).

In the following sections, a review of the models mentioned previously will be given. A detailed review of the assumptions made for the Critical Shear Displacement theory (CSDT) (Yang, 2014) will be presented with the objective to give recommendations to improve them based on the observations obtained from the experimental program and the DIC results.

2.2.1 Tooth model

One of the first models was proposed by Kani (1964), where it is suggested that under an increasing load a reinforced concrete beam transforms into a comb-like structure. The flexural cracks create more or less vertical concrete teeth, while the compressive zone represents the backbone of the concrete comb.

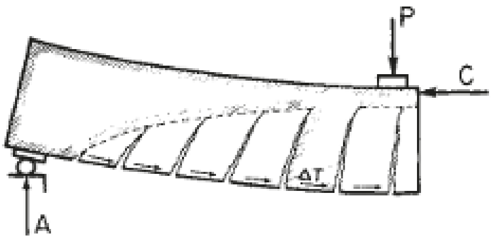

Fig. 2.2.1 Kani's teeth model (Kani, 1964)

Reineck (1991) inspired by the tooth model proposed by Kani (1964), developed a mechanical model where equilibrium is assessed in a "tooth" (Fig. 2.2.2b). The considered shear transfers mechanisms were:

- Friction in the cracks with the vertical component V_{ai}, which refers to the aggregate interlock
- Dowel force of the longitudinal reinforcement V_d
- The shear force component V_c in the compression chord

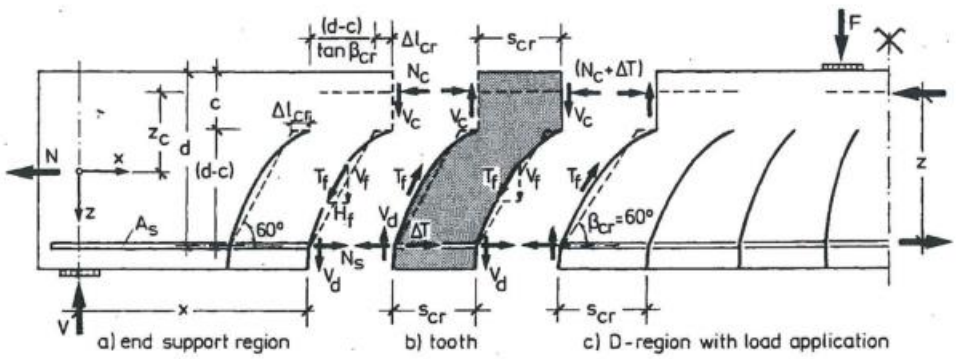

Fig. 2.2.2 Reineck's mechanical model (Reineck, 1991)

Reineck's model considers the crack shape as a straight line at an angle $\beta_{cr} = 60°$, which propagates horizontally by a length Δl_{cr} (Fig. 2.2.2). The crack spacing between primary cracks is derived as:

$$s_{cr} = 0.7(d - c) \tag{2.10}$$

The vertical force equilibrium was assessed considering a free body diagram of the end support region of the beam (Fig. 2.2.2a) as follows:

$$V = V_c + V_f + V_d \tag{2.11}$$

The shear force transfer in the compression zone V_c is the result of integrating the stress over the depth of the compression zone (c), considering a parabolic shear stress distribution, which yields in:

$$V_c = \frac{2}{3}\frac{c}{z}V \qquad \text{with } z = d - \frac{c}{3} \text{ and } c = 0.4d \tag{2.12}$$

The limiting value of dowel action V_{du} was derived by Reineck and corresponds to the one given in Baumann (1970) and Vintzeleou & Tassios (1986).

$$V_{du} = \frac{6}{fc^{1/3}} b_n d_b f_{ct} \qquad \text{with } b_n = b_w - \sum d_b$$

The V_f component must be determined by integrating the stresses along the crack. To simplify this integration, Reineck made some assumptions. The stress distribution due to friction along the cracks τ_f was divided into a constant part τ_{f1} and a parabolic part τ_{f2}. Considering equilibrium and the condition of maximum and equal shear stress at the neutral axis of a rectangular cross-section, the shear force component is defined as follows:

$$V_f = b_w(d - c)\tau_f - \frac{1}{4}V_d \tag{2.13}$$

The maximum value τ_{fu} follows from the constitutive relation from Walraven's proposal (Walraven, 1981) that states that for a constant crack width the friction in the cracks is linear and decreases with the increasing crack width (Δn).

$$\tau_{fu} = 0.45 f_{ct}\left(1 - \frac{\Delta n}{\Delta n_u}\right) \quad \text{with } \Delta n_u = 0.9mm \qquad \textbf{(2.14)}$$

The corresponding critical slip is:

$$\Delta s_u = 0.336\Delta n + 0.01mm \qquad \textbf{(2.15)}$$

The corresponding crack width (Δn) is derived from the kinematic considerations (see Fig. 2.2.3), where the crack width at mid-depth is considered to be half of the value of the longitudinal reinforcement.

$$\Delta n = 0.71\varepsilon_s s_{cr} \qquad \textbf{(2.16)}$$

The detailed derivation of can be found in Reineck (1991).

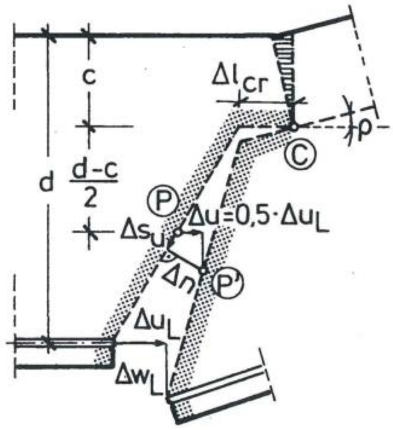

Fig. 2.2.3 Kinematic considerations (Reineck, 1991)

2.2.2 Critical shear crack theory

The Critical Shear Crack Theory (CSCT) was first introduced by Muttoni & Schwartz (1991) and since then further improvements have been made for shear of one and two-way slabs (Muttoni & Fernández Ruiz, 2008; Muttoni, 2008). This theory states that the shear strength of reinforced concrete members without shear reinforcement depends on the opening and roughness of a critical shear crack transferring shear (Muttoni & Fernández Ruiz, 2008).

This theory parts from the consideration that initially, the tensile stresses that lead to the development of the critical shear crack are initiated by the following shear transferred actions:

- Cantilever action (Fig. 2.2.4a). Refers to the shear carried by an inclined compression chord by means of the concrete between two flexural cracks, as a cantilever beam or the so-called "tooth" defined by Kani (1964).

- Aggregate interlock ((Fig. 2.2.4b)
- Dowel action (Fig. 2.2.4c)
- Residual tensile strength of concrete (Fig. 2.2.4d)

Once the critical shear crack develops, the mechanism responsible for transferring the shear is the arching action (Fig. 2.2.4e-f). This action accounts for the inclination of the compression chord and its strength depends on the aggregate interlock capacity (Muttoni & Fernández Ruiz, 2008). The parameters governing the arching actions and thus the shear strength are the location and crack width of the critical shear crack and the aggregate size.

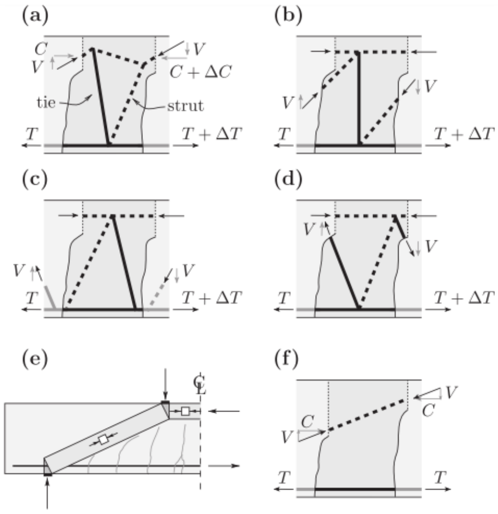

Fig. 2.2.4 Shear-transfer actions: (a) cantilever action; (b) aggregate interlock; (c) dowel action; (d) residual tensile strength of concrete; and (e-f) arching action (Fernández Ruiz, Muttoni, & Sageseta, 2015)

2.2.3 Two-parameter kinematic theory

The two-parameter kinematic theory (2PKT) for deep beams was first introduced by Mihaylov et al. (2013) and it can describe the deformed shape of deep beams and predict the ultimate shear strength of such members. It has been extended to the non-linear five spring model (Mihaylov B., 2014), which predicts the complete load-displacement response of shear-critical deep beams and the three-kinematic theory (3PKT) (Mihaylov et al., 2016) to account for the shortening of the members caused by axial forces.

The two-parameter kinematic theory assumes that the shear failure of a deep beam occurs along a crack that extends from the inner edge of the support to the loading plate (see Fig. 2.2.5). The concrete above the critical crack is modeled as a rigid block that has a critical loading zone (CLZ), which is the area located below the loading plate and is highly stressed. The concrete below the critical crack is represented as radial struts that connect the loading point to the longitudinal reinforcement.

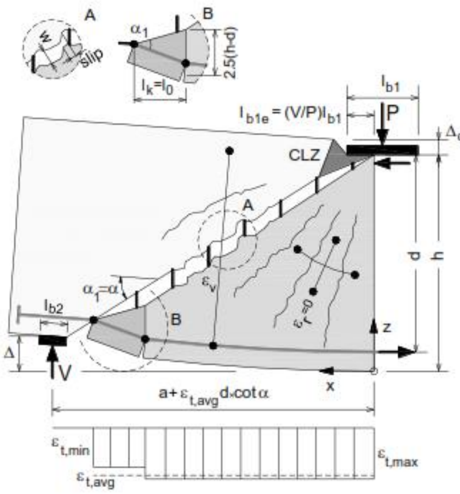

Fig. 2.2.5 Assumption of 2PKT (Mihaylov, Bentz, & Collins, 2013)

The main assumptions of this theory are that, with respect to the loading plate, the motion of the concrete block above the critical crack can be described as a rotation about the top of the crack and a vertical translation, as shown in Fig. 2.2.5. The rotation is proportional to the average strain in the bottom longitudinal reinforcement ($\varepsilon_{t,avg}$), while the translation equals the vertical displacement Δ_c of the critical loading zone (Mihaylov, Bentz, & Collins, 2013). Thus, the two degrees of freedom (DOF) are the $\varepsilon_{t,avg}$ and Δ_c (Fig. 2.2.6). The elongation of the longitudinal reinforcement causes the rotation of the radial struts around the loading point which increases the crack width, while the transverse displacement results in widening and slipping of the critical crack.

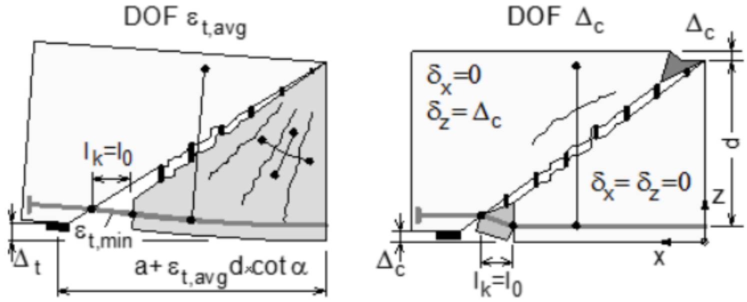

Fig. 2.2.6 Degrees of freedom (Mihaylov, Bentz, & Collins, 2013)

The angle of the critical crack (α_1) is related to the a/d ratio and should be determined as the smallest of the angles α or θ, see Fig. 2.2.7. The angle α forms when connecting the inner edge of the support to the outer edge of the effective width of the loading plate, while angle θ can be determined from the simplified Modified Compression Field Theory (MCFT) (Bentz, Vecchio, & Collins, 2006) or can be assumed to be equal to 35º. For deep beams, the angle α is governing while the angle θ represents the transition to slender beams when the a/d ratio increases.

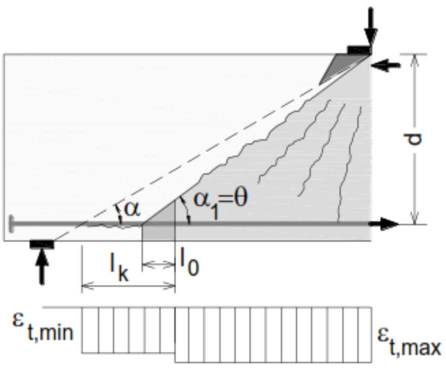

Fig. 2.2.7 Modification of the angle α_1 for long beams (Mihaylov, Bentz, & Collins, 2013)

Based on the above-mention assumptions, the vertical and horizontal displacements of each of the points in the shear span can be expressed in terms of the two DOFs, as shown in Mihaylov et al. (2013).

A free body diagram of a deep beam is shown in Fig. 2.2.8 and as it can be observed the shear resistance is expressed as:

$$V = V_{CLZ} + V_{ai} + V_s + V_d \tag{2.17}$$

where

V_{CLZ} : are the shear forces resisted by the critical loading zone, which depend on the effective width of the loading plate, the average compressive stress and a crack shape coefficient that accounts for the fact that in slender beams the critical crack is not straight.

V_{ai} : are the forces resisted by aggregate interlock and determined as expressed by Vecchio & Collins (1986)

V_s : is the shear resisted by the stirrups

V_d : is the shear resisted by the dowel action which depends on the number of bars, the bar diameter, the length of the dowels and an effective yield strength.

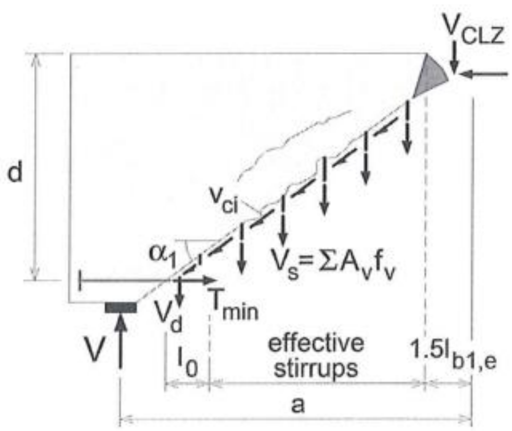

Fig. 2.2.8 Shear transfer mechanisms in deep beams (Mihaylov, Bentz, & Collins, 2013)

2.2.4 Critical shear displacement theory

Yang (2014) based on experimental observations, developed a new theory for the shear capacity of reinforced concrete members without shear reinforcement. The theory proposes that the shear displacement of the critical inclined crack can be considered as a failure criterion for the shear capacity of a structural member, it considers that the opening of the critical inclined crack starts with the opening of a dowel crack, that develops along the tensile reinforcement. The opening is triggered when the shear displacement of an already form flexural crack reaches a critical value. This process is illustrated in Fig. 2.2.9.

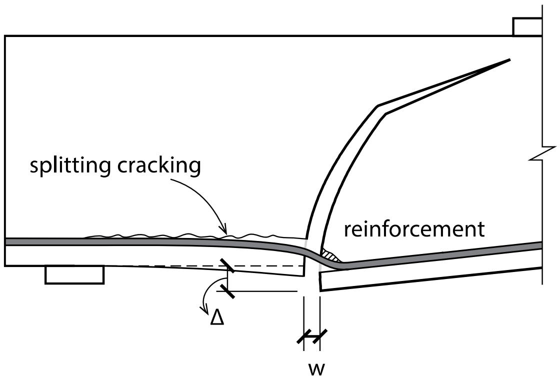

Fig. 2.2.9 Crack kinematics at failure, according to (Yang 2014).

Yang's theory is based on the following shear force transfer mechanisms that occur on a critical inclined crack or flexural shear crack:

- Shear force transferred in the compression zone (V_c) determined with Mörsch´s approach (1909)
- Dowel action (V_d) using the expression proposed by Bauman and Rüsch (1970)
- Shear force transfer by aggregate interlock (V_{ai}) adopting the expressions proposed by Walraven (1981)

Concerning aggregate interlock, the aspects that contribute the most to the shear force transmission are the crack shape and the normal and tangential displacements along the crack profile. Since Walraven's formulations must be solved with numerical integrations, a simplified crack profile was proposed to facilitated and simplify the relationship between V_{ai}, the crack width (w) and the shear displacement (Δ).

To arrive at the simplified crack pattern some assumptions were made:

1. The crack is composed of two branches: the major crack or main branch and the secondary branch located in the compressive zone. The latter contributes to increasing shear displacement in the major crack part when the shear force increases
2. The major crack can be simplified as perpendicular to the longitudinal direction of the beam.

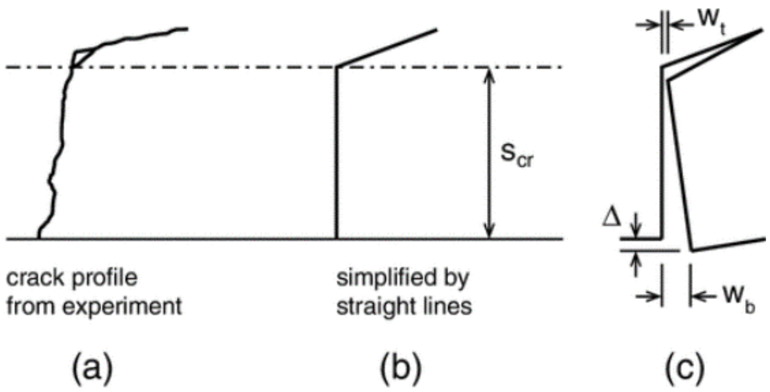

Fig. 2.2.10 Simplified crack profile (Yang, Walraven, & Den Uijl, 2016)

Based on these two assumptions, the simplified crack profile shown in Fig. 2.2.10(b) was derived. In the main branch of the crack, the shear displacement generates aggregate interlock stresses while the secondary branch allows additional shear displacement in the major crack. This simplification allows the normal crack opening and the shear displacement of the major crack to be independent.

To simplify the shear force-displacement relationship, the distribution of the crack opening was assumed to vary linearly, with a crack width at the top of the main branch (w_t) equal to 0.01 mm. While the crack width at the reinforcement level (w_b) is estimated considering the crack spacing and the steel stress as follows:

$$w_b = l_{cr,m}\varepsilon_s \tag{2.18}$$

If the height of the fully develops crack is s_{cr} and the slope of the stress line is k_c , the space between a fully developed crack and the next possible cracked section is:

$$l_{cr,m} = \frac{s_{cr}}{k_c} \tag{2.19}$$

It is assumed that for a major crack, its total height is reached directly after its formation and determined by cross-sectional equilibrium, the height is equal to:

$$s_{cr} = \left[1 + \rho_s n_e - \sqrt{2\rho_s n_e + (\rho_s n_e)^2}\right]d \tag{2.20}$$

The simplification of V_{ai} is based on the shear stress-crack width relationship under constant shear displacement, where at the same shear displacement, the smaller crack widths result in larger shear stresses. Thus, the total V_{ai} was estimated considering the upper part of the crack (where the crack width is much smaller compared to the one at the reinforcement level) to a chosen w_{b0} of 0.04mm. Thus, the expression for aggregate interlock is simplified into a function depending just on the shear displacement, as follows:

$$V_{ai} = 6.39 f_c^{0.56} b \frac{0.003}{w_b - 0.01}(-978\Delta^2 + 85\Delta - 0.27) \tag{2.21}$$

The remaining unknown is the critical shear displacement Δ_{cr}. Yang (2014) carried out a back analysis based on the shear test results from existing databases, more information can be found in the reference document. With the results, a plot of the Δ_{cr} against the depth of the beams was constructed, as shown in Fig. 2.2.11

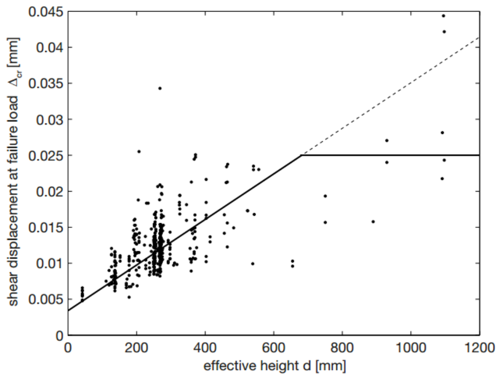

Fig. 2.2.11 Calculated critical shear displacement against effective height (Yang, 2014)

These results show that the values of Δ_{cr} fall in a range between 0.005 and 0.05 mm presenting a relatively large scatter. An expression for Δ_{cr} based on a regression analysis was formulated as follows:

$$\Delta_{cr} = \frac{d}{29800} + 0.005 \leq 0.025mm \tag{2.22}$$

To account for the influence of the rebar diameter on Δ_{cr} , Eq. (2.22) was adjusted to:

$$\Delta_{cr} = \frac{25d}{30610\phi} + 0.0022 \leq 0.025mm \tag{2.23}$$

Considering the advantages of DIC, the simplification of the crack profile and the assumed kinematics of the crack at failure will be analyzed in Chapter 6.

2.3 Digital Image Correlation

Despite the large number of experimental programs conducted to test specimens in shear, there was almost no information about the actual crack development during the failure process until recent years, when the use of photogrammetric techniques started to be used in experimental programs to investigate the actual crack patterns and kinematics (Cavagnis et al., 2015). One of these techniques is the Digital Image Correlation (DIC) which can be defined as a digital measurement method that provides measurements of an entire specimen surface by comparing a reference image in an un-deformed state to a series of deformed images tracking points or patterns between them.

This method has some advantages over traditional measurements (LVDTs) since it is a non-contact technique that provides full-field measurements and allows to continuously track the evolution of each individual crack, even an instant before failure. Fig. 2.3.1 shows the typical output results in terms of displacements in pixels and equivalent strains obtained from DIC.

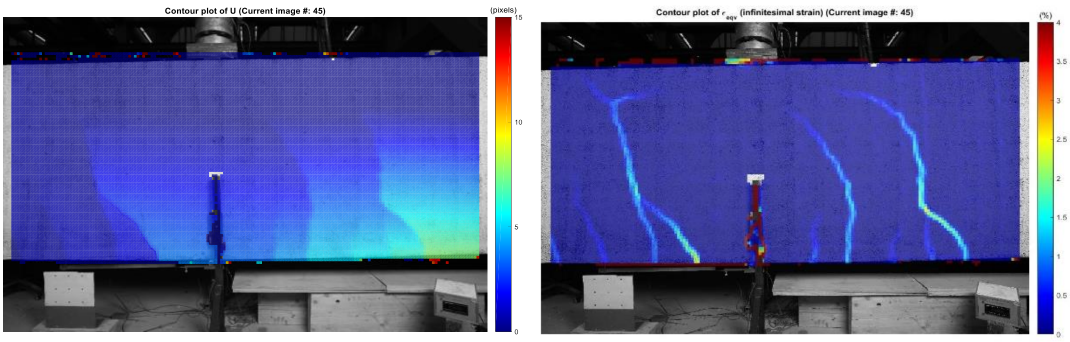

Fig. 2.3.1 Typical results from DIC. Displacement field in pixels (left). Equivalent strains (Right)

DIC has proven to be an adequate tool to help to track and to understand the shear failure process of reinforced concrete members without shear reinforcement as demonstrated by Campana et.al., 2013; Cavagnis et al.,2017, 2018; and Huber et al., 2016, where experimental programs in combination with DIC measurements were carried out to study the various shear transfer mechanisms.

The following sections present a review of the fundamental principles of 2D DIC and the implementation of the technique.

2.3.1 2D Digital Image Correlation

In general, the implementation of 2D digital image correlation method is simple and can be summarized in the following three steps, as shown in Fig. 2.3.2 (Pan, Qian, Xie, & Asundi, 2009):

1. Specimen and experimental preparations
2. Recording images before and after loading
3. Processing the acquired images using a computer program to obtain the displacements and strains.

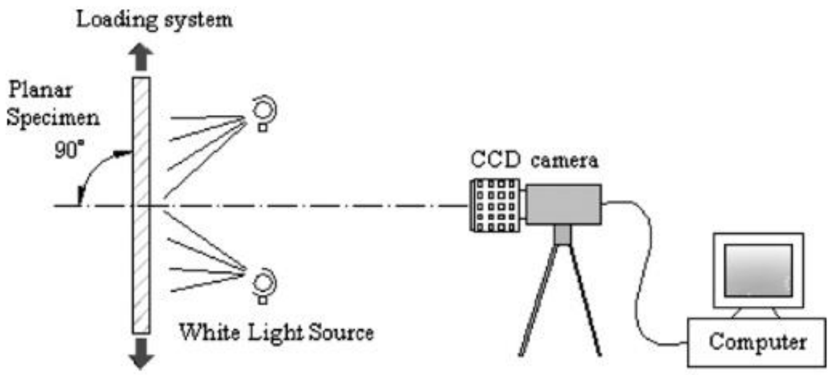

Fig. 2.3.2 Typical experimental setup using 2D DIC technique (Pan et al.,2009)

The typical DIC set up used in this research is explained in Section 3.2.

2.3.1.1 Specimen preparation and image recording

Regarding the preparation of the specimen, its surface must have a random speckle pattern, which can be the natural texture of the specimen or made by applying black and/or white paint to increase the contrast. The quality of the speckle pattern is highly related to the accuracy of the DIC results, it must reflect image contrast and the size depends on the test requirements and the resolution of the camera. The ideal pattern must be non-periodic and without a preferred orientation. Fig. 2.3.3 shows examples of patterns with different properties found in the literature.

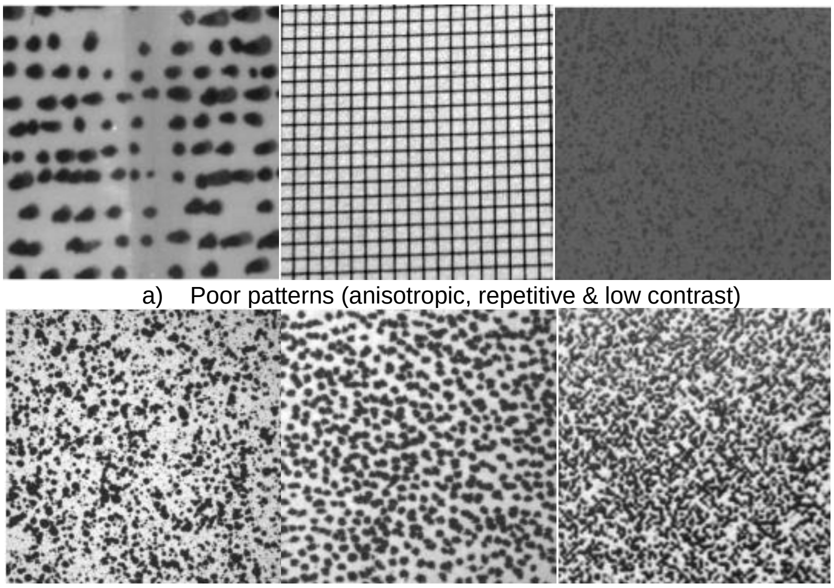

a) Poor patterns (anisotropic, repetitive & low contrast)

b) Good patterns

Fig. 2.3.3 Examples of patterns with poor and good properties (AN-1701)

It is important to note that the quality of the pattern affects the selection of the subset size, the subset must be large enough to ensure that there is enough distinctive pattern to be distinguished from other subsets. The pattern used in the tested specimens can be found in Section 3.2 Fig. 3.2.1.

To ensure accurate results, the camera must be placed with its optical axis perpendicular to the specimen surface (see Fig. 2.3.2) and a stable and even illumination must be guaranteed during the loading procedure. It is also important to use a high-resolution camera with high-quality low noise charge-coupled device sensors (CCD) and telecentric lens. The details of the camera and lens used to record the images in this thesis are given in Section 3.2.

Since the image is a 2D projection of the specimen surface, to ensure that the estimated displacements and the actual displacements are the same, the following requirements must be met (Pan, Qian, Xie, & Asundi, 2009):

- The surface of the specimen must be flat and remain parallel to the charge-coupled device sensors (CCD) of the camera and the out of plane motions of the specimen should be small enough to be neglected.
- The image should be distortion free. However, if the influence of the distortion cannot be neglected, correction techniques should be implemented to provide accurate measurements.

In this research, the influence of the radial distortion was corrected using the distortion function of the length along the radius direction as:

$$r_1 = ar_0^{\,4} + br_0^{\,3} + cr_0^{\,2} + dr_0 + e \quad \textbf{(2.24)}$$

Where r_1 and r_0 are the distances from the center of the image to the center of define points in the image using the real coordinates and the photo coordinates respectively. The results from this calibration are shown in Section 4.1

When all the above requirements are met, highly accurate results can be obtained as reported in (Tung et al., 2008; L Reu et al., 2009) where accuracies in a range of 0.01 to 1 pixel were found.

2.3.1.2 Fundamental principles

DIC technique is performed between two digital images acquired before and after deformation during the test of a specimen, these images are referred as the reference (or undeformed image) and the target (or deformed) image, respectively (Pan, Xie, Guo, & Hua, 2007). It uses random speckle patterns applied on the surface of the specimen to obtain full-field displacements by tracking and matching subsets before and after deformation. A subset, as illustrated in Fig. 2.3.4, is a square of (2M+1) x (2M+1) pixels taken from the reference image where the center point $P(x_0, y_0)$ is tracked to determine its corresponding location at the deformed image.

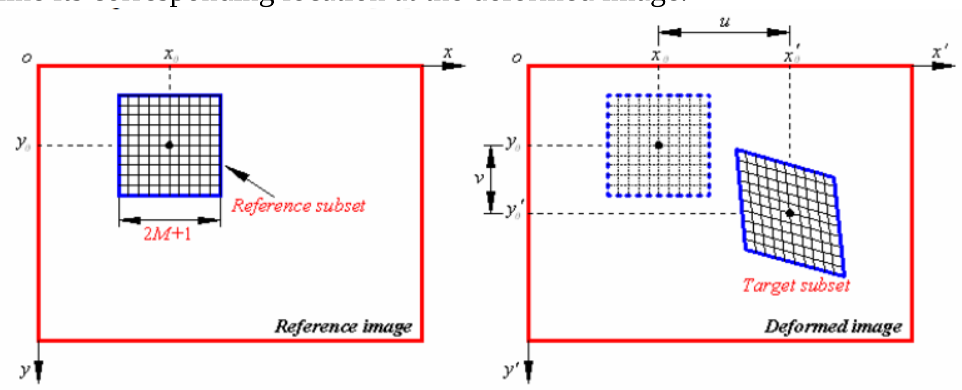

Fig. 2.3.4 Reference and target subsets (Pan, Xie, Wang, Qian, & Wang, 2008)

To evaluate the degree of similarity between the reference subset and the deformed subset, a cross-correlation (CC) criterion or sum-squared difference (SSD) correlation criterion must be predefined (Pan, Qian, Xie, & Asundi, 2009). The matching procedure is performed by searching the peak position of the distribution of correlation coefficients. Once the maximum or minimum correlation coefficient is detected, the position of the deformed subset can be determined. The difference in the locations between the subsets results in the in-plane displacement u and v.

The images used in this thesis are post-processed using the Matlab-based DIC code programmed by Jones (2015). The code computes the normalized cross-correlation coefficient, C, for a range of theoretical displacements (u', v') (see Fig. 2.3.5), in 1-pixel increments by convolving the deformed subset with the reference subset according to:

$$C(u',v') = \frac{\sum x',y'\left[(r(x',y') - \bar{r}_{u',v'})(d(x'-u',y'-v') - d)\right]}{\left\{\sum x',y'\left[(r(x',y') - \bar{r}_{u',v'})^2\right]\sum x',y'\left[(d(x'-u',y'-v') - d)^2\right]\right\}^{1/2}} \quad \textbf{(2.25)}$$

where

r : is the intensity of the pixels in the reference subset
d : is the intensity of the pixels in the deformed subset
(x', y') : are the local subset coordinate axes with origin at the center point

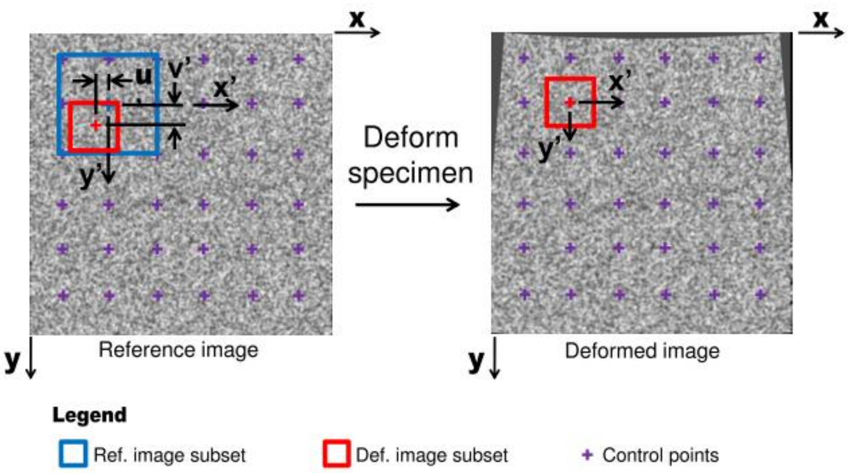

Fig. 2.3.5 Schematic of DIC method used in Matlab code (Jones, 2015)

A grid of control points (purple crosses in Fig. 2.3.5) must be defined, at this points the displacements are computed. Then the strains are calculated by interpolating the displacements using finite element shape functions. Fig. 2.3.6 shows a schematic example using a 16-node finite element (green box) which is drawn through the control points (black circles). The element is mapped to a master element, with local coordinates ξ and η, and the displacements are interpolated over the master element using bi-cubic element shape functions. The derivatives of the interpolated displacements are calculated at the nine Legendre-Gauss points (green stars), and then mapped back to the original element (Jones, 2015).

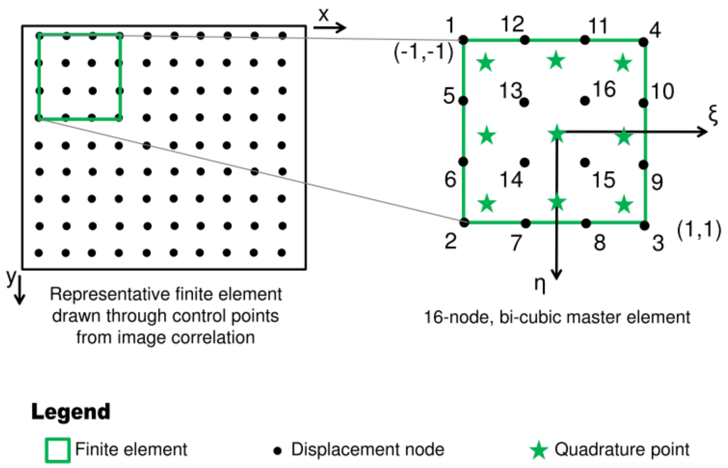

Fig. 2.3.6 Schematic of finite element used for strain calculations (Jones, 2015)

The procedure followed to carry out a typical DIC using the code developed by Jones (2015) is summarized in the following figure.

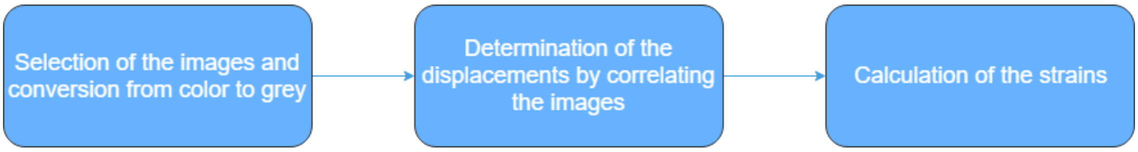

Fig. 2.3.7 Steps for a typical DIC

In this thesis, first, the reduced images were correlated using a large subset size and grid. Then the full-sized images were correlated using a denser grid, a typical subset size consisted of 121 pixels. The displacements were computed at grid points located every 50 pixels in the region of interest, as shown in Fig. 2.3.8. The region of interest had a dimension of approximately 3850 x 5500 pixels.

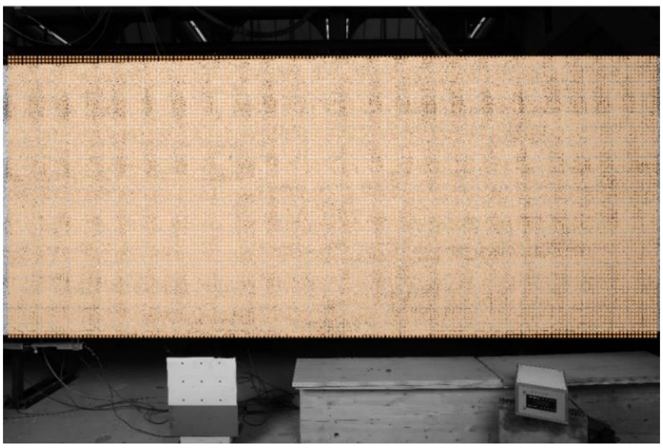

Fig. 2.3.8 Typical grid size of 50 pixels

The strains were calculated by interpolating the raw displacements using 4-noded elements with linear shape functions for the identification of discrete cracks in the specimens. Fig. 2.3.9 shows a scheme of a 4-noded rectangular element.

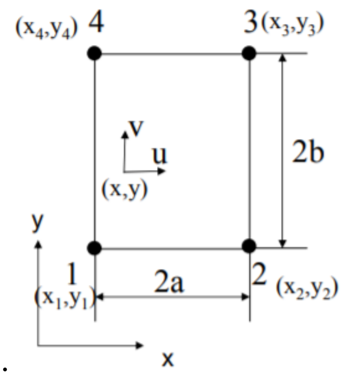

Fig. 2.3.9 Four-node rectangular element

With N_1, N_2, N_3, and N_4 as the bilinear shape functions described as:

$$
\begin{aligned}
N_1 &= \frac{1}{4ab}(x-x_2)(y-y_4) \\
N_2 &= \frac{1}{4ab}(x-x_1)(y-y_3) \\
N_3 &= \frac{1}{4ab}(x-x_4)(y-y_2) \\
N_4 &= \frac{1}{4ab}(x-x_3)(y-y_1)
\end{aligned}
\qquad \textbf{(2.26)}
$$

Then, the strain-displacement relationship is given by:

$$
\varepsilon = \begin{bmatrix} \varepsilon_x \\ \varepsilon_y \\ \gamma_{xy} \end{bmatrix}
$$

$$
= \begin{bmatrix}
\frac{\partial N_1(x,y)}{\partial x} & 0 & \frac{\partial N_2(x,y)}{\partial x} & 0 & \frac{\partial N_3(x,y)}{\partial x} & 0 & \frac{\partial N_4(x,y)}{\partial x} & 0 \\
0 & \frac{\partial N_1(x,y)}{\partial y} & 0 & \frac{\partial N_2(x,y)}{\partial y} & 0 & \frac{\partial N_3(x,y)}{\partial y} & 0 & \frac{\partial N_4(x,y)}{\partial y} \\
\frac{\partial N_1(x,y)}{\partial y} & \frac{\partial N_1(x,y)}{\partial x} & \frac{\partial N_2(x,y)}{\partial y} & \frac{\partial N_2(x,y)}{\partial y} & \frac{\partial N_3(x,y)}{\partial y} & \frac{\partial N_3(x,y)}{\partial x} & \frac{\partial N_4(x,y)}{\partial y} & \frac{\partial N_4(x,y)}{\partial x}
\end{bmatrix}
\begin{bmatrix} u_1 \\ v_1 \\ u_2 \\ v_2 \\ u_3 \\ v_3 \\ u_4 \\ v_4 \end{bmatrix}
\qquad \textbf{(2.27)}
$$

2.3.2 DIC in shear tests

The application of DIC in concrete structures has been continuously increasing due to the evolution of the technology (high-resolution digital cameras) and the advantages that it has over traditional measuring techniques.

In recent years, DIC has been implemented in several research programs (Campana et al., 2013; Huber et al., 2016 and Cavagnis et al.,2017, 2018) to investigate the shear failure process of reinforced concrete members without shear reinforcement. The investigations are usually focused on providing the calculated contribution of the various shear transfer actions based on the measured kinematics and by using constitutive laws.

Campana et al. (2013) carried out an experimental program to investigate the activation of the various shear transfer mechanism for one way RC members. The details of the crack pattern and crack kinematics were obtained using a high-precision distance measurement device gluing metallic targets on the concrete surface. Similar calculations were performed by Huber et al. (2016), implementing the DIC technique using two cameras of 2352 by 1728 pixels resolution. The results from these studies showed that the governing shear transfer action depends on the crack shape and kinematics. The studies considered the following transfer mechanisms: the aggregate interlock contribution, the residual tensile strength, dowel action and the contribution of the stirrups. Huber et al. (2016) neglected the contribution of the uncracked concrete zone because of the limited measurements in the compression zone.

The most extensive research program was carried out by Cavagnis et al.,2017, where the governing contribution at failure (peak load) was investigated. The DIC technique was implemented using two cameras of 36.3 megapixels with a speckle pattern of approximately 0.35 mm. The considered transfer mechanisms were: inclination of the compression chord, arching action, residual tensile strength, dowel action, and aggregate interlock. The comparison between the calculated actions and the experimental shear force had a good agreement (average ratio of 1.01). With the results from the analysis, a mechanical model consistent with the main assumptions of the CSCT was developed.

These studies focused on the behavior governing the shear strength during the final instant before failure. However, limited information is available on the moment of the opening of the unstable crack along the tensile reinforcement which has been found to be critical to the shear failure process and occurs earlier before the final failure. This thesis will focus on analyzing this critical moment.

2.4 Conclusion

The following aspects have been learned from exploring the topics discussed in the previous sections:

- The main shear transfer mechanism considered in the mechanical shear models are mainly the shear transfer in the uncracked concrete zone, the dowel action, and aggregate interlock. The dowel action is usually calculated with empirical formulas and aggregate interlock with Walraven's formulation. The contribution of the uncracked concrete zone depends on the variation of the lever arm and is either calculated with Mörch´s approach or with a strut and tie model.
- The most important aspects considered in the available shear models are the shape of the critical crack and the kinematics involved, which were usually developed based on measurements obtained from traditional measuring techniques and need validation using detailed kinematic measurements from experiments.

- A simplification of the crack pattern allows simplifying the relation of the displacements along the crack and thus, facilitates the calculation of the aggregate interlock stresses.
- To ensure accurate DIC measurements, the following requirements need to be met: Good speckle pattern (random and high contrast), high-resolution camera, parallelism between the camera and the surface and a proper calibration.
- Digital Image Correlation presents the advantage of providing a full field of continuous measurements that can be used to obtain kinematic measurements and crack patterns of individual cracks. Combining these measurements with constitutive laws the contribution of the various shear transfer mechanisms can be computed.

3 Experimental Program

In this section, a summary of the properties of the specimens and the test set up is presented. This project is based on the results obtained from an experimental program proposed to study the size effect of reinforced concrete members without shear reinforcement. This experimental program is an extension of the previous study reported in Yang (2016) on the transition between the flexural and shear failure modes. For this project, the results from 10 beams are selected for the analysis, the data for the complete experimental program can be found in the lab measurement report (Zarate Garnica & Yang, 2018).

3.1 Test set up and properties of the specimens

The tested specimens were simply supported and loaded by a point load. The position of the supports and loading points are given in Fig. 3.1.1

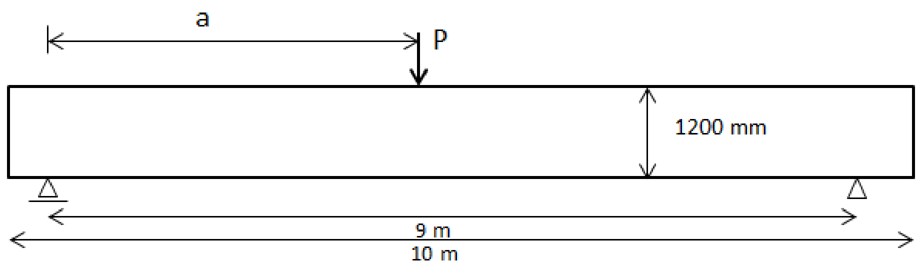

Fig. 3.1.1 Test set up

Regarding the dimensions, the specimens of this experimental program have a height h=1200 mm with a length of 10000 mm and 300 mm wide.

The reinforcement configurations of the specimens vary among the test series. In general, the reinforcement ratios are roughly indicated by the number of the specimen. A detailed drawing is given in Fig. 3.1.2 and Table 3.1-1 presents the information of the selected specimens. The reinforcement consists of plain bars (test with the letter I) with an average yield strength of f_{ym} = 296.8 MPa and an average tensile strength of f_{um} = 425.9 Mpa and for ribbed bars (test with letter H) usual steel bars grade 500 MPa are utilized.

Table 3.1-1 Summary of selected specimens

Specimen No.	Rebar config	$f_{c,max}$ [MPa]	h [mm]	d [mm]	ρ [%]
H301A	3 ϕ 20	86.92	1200	1160	0.27
H352A	4 ϕ 20	78.33	1200	1160	0.36
H401A	3 ϕ 25	80.15	1200	1158	0.42
H402A	3 ϕ 25	80.15	1200	1158	0.42
H403A	3 ϕ 25	78.33	1200	1158	0.42
H404A	3 ϕ 25	78.33	1200	1158	0.42

H121A	8 ϕ 25	80.15	1200	1151	1.14
H121A	8 ϕ 25	80.15	1200	1151	1.14
I60A2	4 ϕ 25	78.75	1200	1158	0.57
I60A3	4 ϕ 25	78.75	1200	1158	0.57

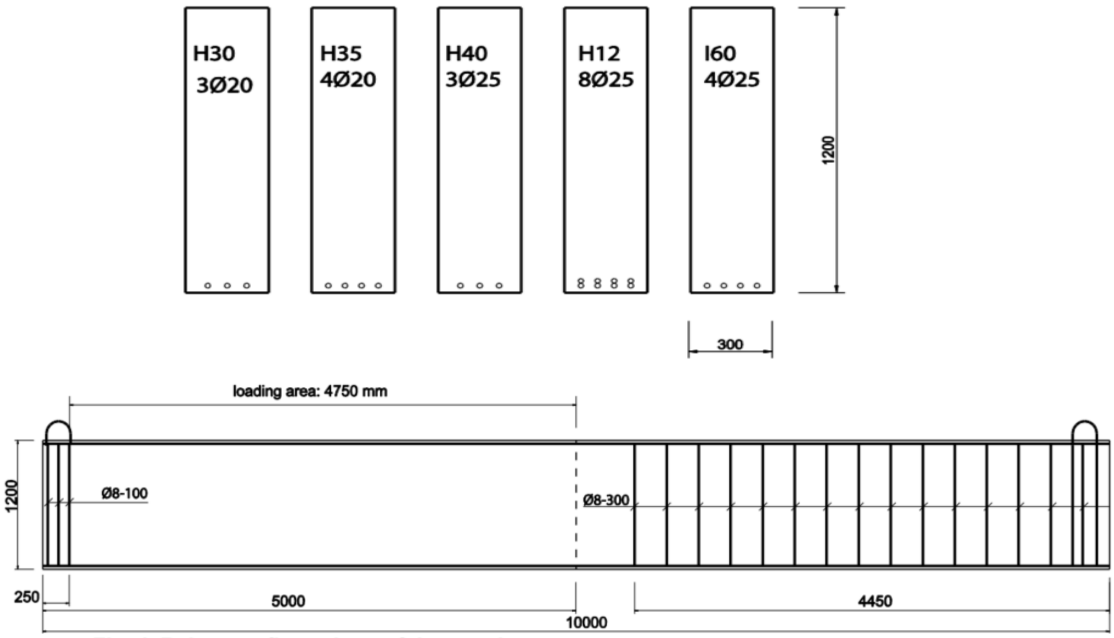

Fig. 3.1.2 Reinforcement layout

During all test, several measurements were performed, for the complete information refer to (Zarate Garnica & Yang, 2018). In the list below, some of the measurements are indicated:

1 The force in the actuator measured by a load cell (1 in Fig. 3.1.3)
2 The maximum deflection under the loading point, measured by a pair of laser triangulation displacement sensors at both sides of the member (2 in Fig. 3.1.3)
3 Crack opening in an LVDT array, which consists of longitudinal LVDT's at the level of reinforcement, and at the mid-height of the specimen with vertical LVDT's in between. (3 in Fig. 3.1.3)

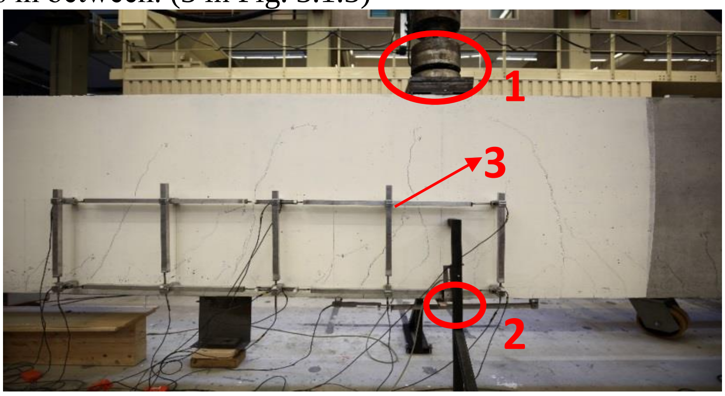

Fig. 3.1.3 Measurements

3.2 Digital Image Correlation measurements

In addition to the conventional LVDTs, the use of Digital Image Correlation (DIC) measurement was implemented. For this purpose, images were recorded during the entire experiment and post-processed to find displacements and strains.

To implement the DIC technique, a paint roller was used to uniformly apply a random speckle pattern with black and white paint on one of the faces of the specimen. The size of the speckle pattern varies from 1 to 2 millimeters, a detail of the pattern is shown in Fig. 3.2.1.

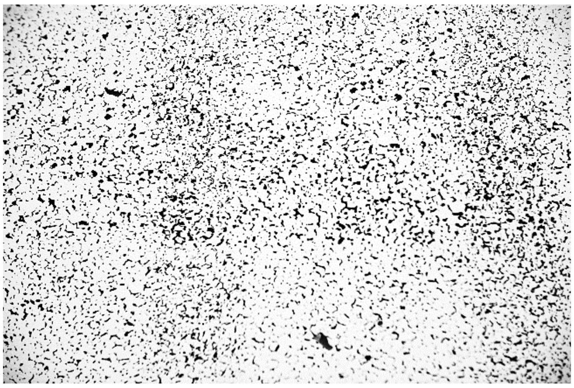

Fig. 3.2.1 Detail of the applied speckle pattern

The typical DIC set up used during the experimental program is shown in Fig. 3.2.2 and it consisted of a high-resolution camera of 8688 by 5792 pixels (Canon EOS 5DS R) with a wide-angle lens (Sigma 20 mm), two studio flashes (Falcon eyes TE-500A) to keep a constant illumination and a LED screen to record the applied force during the experiment. The parallelism between the camera and the planar specimen surface was guaranteed by mounting the camera in rigid metallic support fixed to the floor. The flash was controlled with a remote to avoid vibrations caused by the manual operation of the camera.

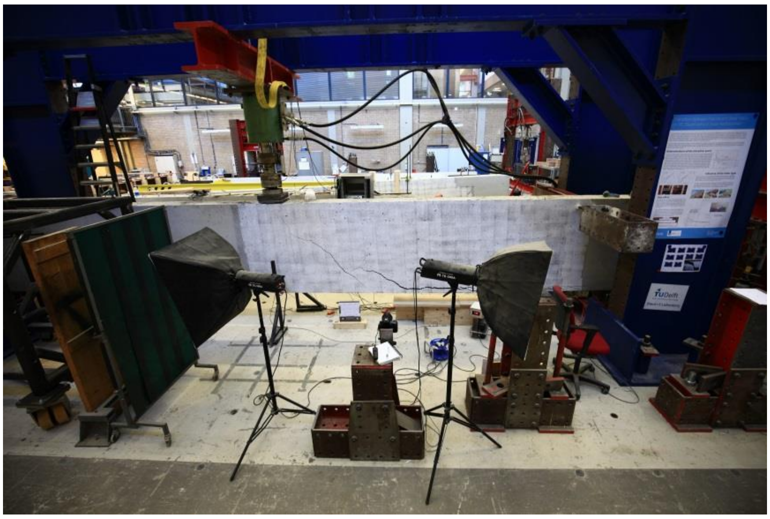

Fig. 3.2.2 Typical DIC test set up

At each load step, photos were taken of the surface with the pattern, for instance, Fig. 3.2.3 shows the loading scheme and the moment of the photo shooting.

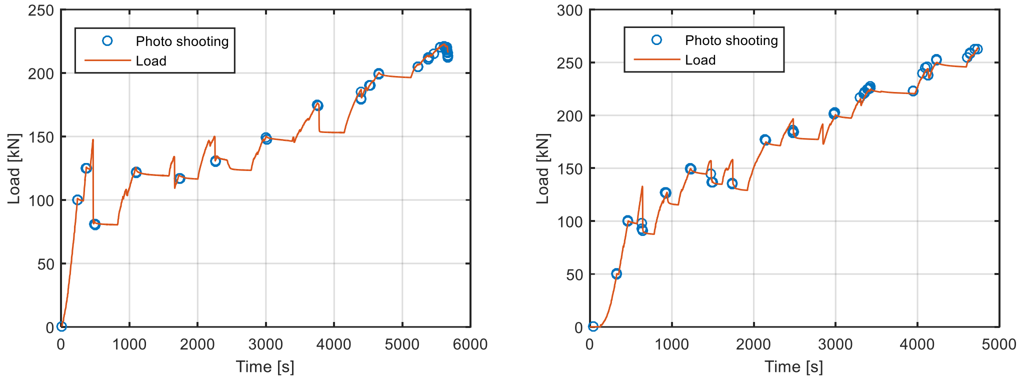

Fig. 3.2.3 Loading schemes (applied load vs time) and the moment of the photo shooting for test H301A(left) and H401A(right)

4 Methodology

This chapter presents the details of the methodology carried out to develop the algorithm that calculates the contribution of the shear transfer mechanisms. The general procedure is divided into four steps or units as shown in the flowchart presented in Fig. 1.3.1 and are as follows:

- Unit 1: DIC calibration
- Unit 2: Crack pattern
- Unit 3: Crack kinematics
- Unit 4: Shear transfer mechanisms

In the following sections, each unit is described. The Matlab codes designed for the computation of the contribution of the shear transfer mechanisms can be found in the repository as an additional file.

4.1 Unit 1: DIC calibration

The aim of this unit is to explain the implementation and calibration of the DIC measurements. The process starts with the correlation of the images using the Matlab-based DIC code programmed by Jones (2015), which was described in Section 2.3.1.2. The direct output of this correlation is the full-field displacements of the surface in units of pixels. Thus, an accurate scale for the conversion from pixels to millimeters must be obtained.

The scale is found by employing a target of nine red markers (see Fig. 4.1.1) that is set perpendicular to the camera and is in the same plane as the specimen. The distance between the red points is known (80 mm), thus the relationship between the pixels and millimeters can be found. The typical relation for the tested specimens is of approximately 0.31 mm/pixel.

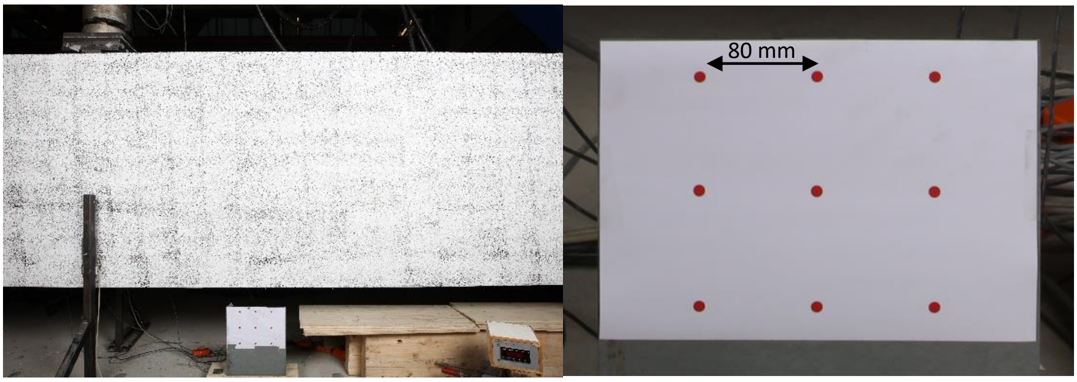

Fig. 4.1.1 Location of the target (Left) and detail of red markers (Right)

As learned in the literature review, to achieve accurate results, it is important that the images are distortion free. In this research, the influence of the radial distortion was corrected using Eq.(2.24) and the image with 532 red markers shown in Fig. 4.1.2. The distance between each marker is of 10 mm.

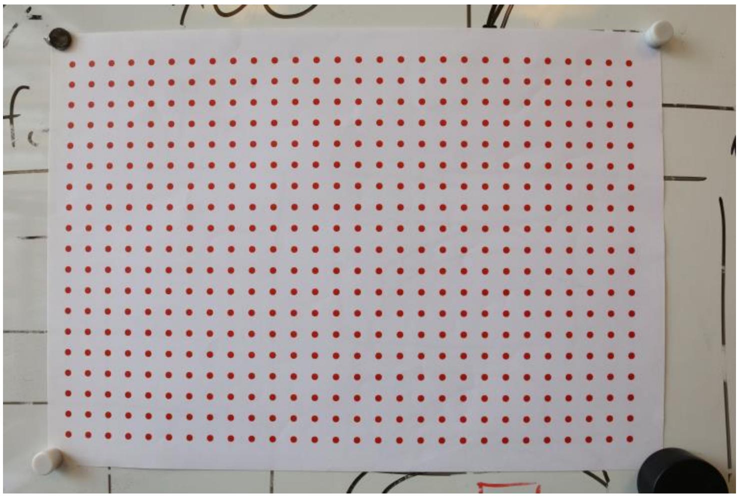

Fig. 4.1.2 Picture of 532 red markers used for the correction of radial distortion.

The coefficients of the 4^{th} order polynomial were: 6.777848e-14, 5.838949e-10, -5.680687e-06, 1.010089e+00, -5.719554e+00. These coefficients were used to evaluate the function and correct the pictures from radial distortion. It is important to note that the coefficients fit the data of a picture taken with the same characteristics as the pictures taken during the experiments:

- F-stop:f/13
- Exposure time: 1/80 sec
- ISO:100

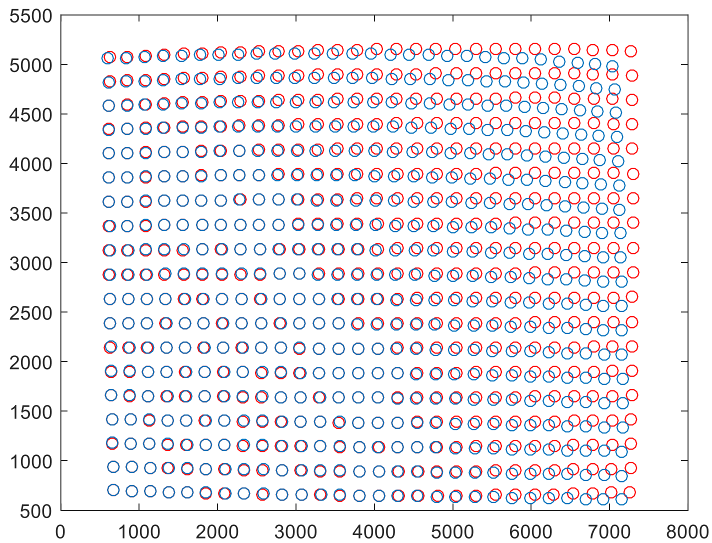

Fig. 4.1.3 Influence of radial distortion. In red markers without correction and in blue corrected markers.

Finally, before performing any further analysis, the accuracy of the displacement measurements from DIC analysis must be evaluated and compared with the LVDT readings. For example, taking test H301A, for which Fig. 4.1.4 presents the LVDT array and the determination of the location of the nodes of the LVDT grid in the DIC side. At these locations, the relative displacements in the horizontal direction of the nodes are compared with the measurements of the LVDT1-4. Fig. 4.1.5 shows the comparison between the LVDT and DIC measurements, it can be observed that the difference relays mostly within 0.1 mm (0.3 pixels). Considering that the crack pattern and the displacement field are not completely the same for both sides of the specimen, the accuracy is considered as acceptable. Comparable results were found on the other specimens; therefore, it is considered that the DIC analysis is accurate for this research.

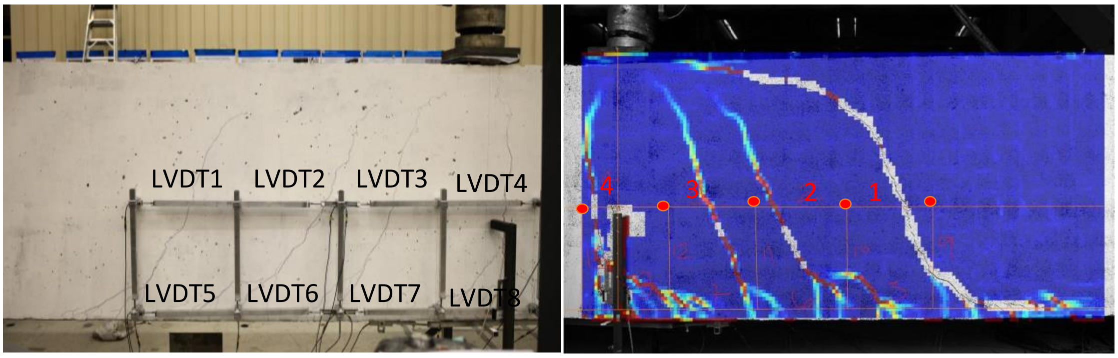

Fig. 4.1.4 LVDT array of H301A (left) and location of nodes on DIC side (right)

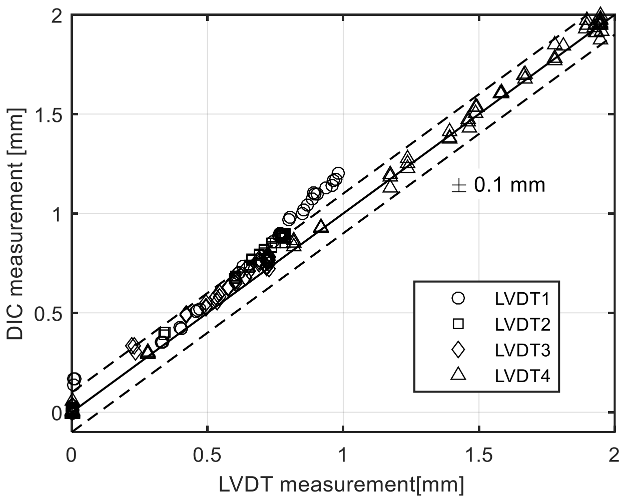

Fig. 4.1.5 Comparison between LVDT and DIC measurements for Test H301A

4.2 Unit 2: Crack pattern

One of the most important aspects of this project is the determination of the crack pattern. For that purpose, the raw output of the DIC (strains) is filtered to remove the noise and reveal a defined crack profile. The filtering is performed by dividing the region of interest into squares and then applying the mean, dispersion and standard deviation filtering, this was performed using a Matlab script developed by Celada (2017).

The filtering transforms the image into a binary image by changing each pixel according to whether the original value is inside or outside a specific range. The threshold values of mean, standard deviation and dispersion are set by the user. The result from this process is a filtered crack profile that consists of several pixels that are transformed in x and y coordinates that represent the various small segments that constitute the filter crack profile. Fig. 4.2.1 illustrates the procedure for the test H122A.

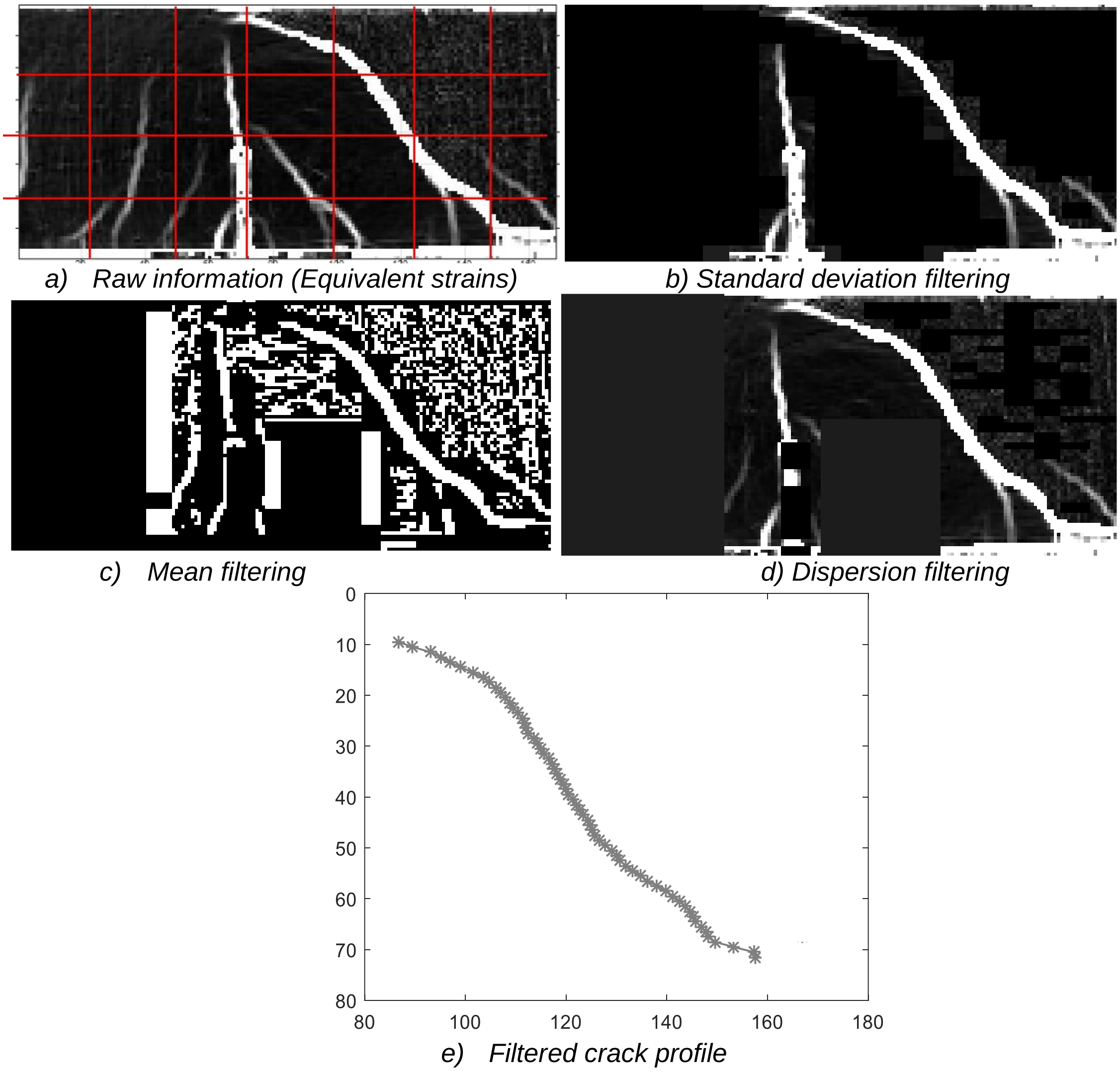

Fig. 4.2.1 Filtering procedure for beam H122A

The script from Celada (2017) was modified to fit the coordinates of the filtered crack profile with piecewise linear interpolation. Thus, the crack profile is approximated to a series of continuous linear segments (see Fig. 4.2.2), this is done with the aim of smoothing the crack profile by eliminating any abrupt changes that could result in an overestimation of the forces transferred through the crack. Each segment has its own pair of x and y coordinates as illustrated in Fig. 4.2.2 and the angle of each segment can be calculated with the following relation:

$$\tan \alpha_i = \frac{dy_i}{dx_i} \quad \textbf{(4.1)}$$

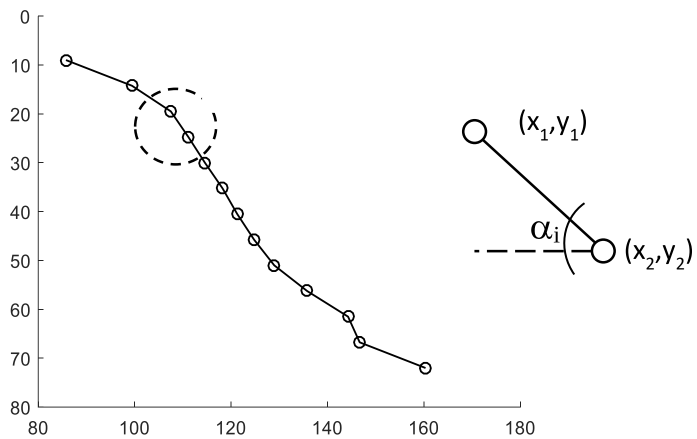

Fig. 4.2.2 Approximation of crack profile for beam H122A

The total angle α of the crack is determined by calculating the average of the angles of the segments located at the mid-region of the crack.

A Matlab script was developed to manually select the coordinates or points in the crack pattern when a specific part of the crack needs to be analyzed. These points are approximate into a polyline. Fig. 4.2.3 shows an example of this manual selection of points for beam H401A.

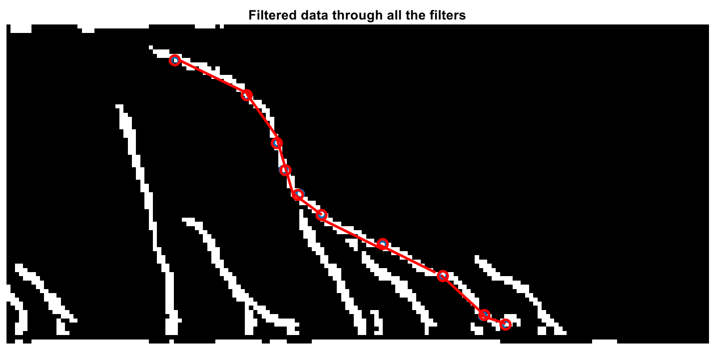

Fig. 4.2.3 Manual selection of crack profile for beam H401A

4.3 Unit 3: Crack kinematics

The crack kinematics are computed using the DIC measurements that provide full-field displacement of the surface of interest. The crack kinematics can be divided into two depending on the method in which they are computed: Projected displacements along the crack profile and the displacement difference in x and y-direction, as shown in Fig. 4.3.1.

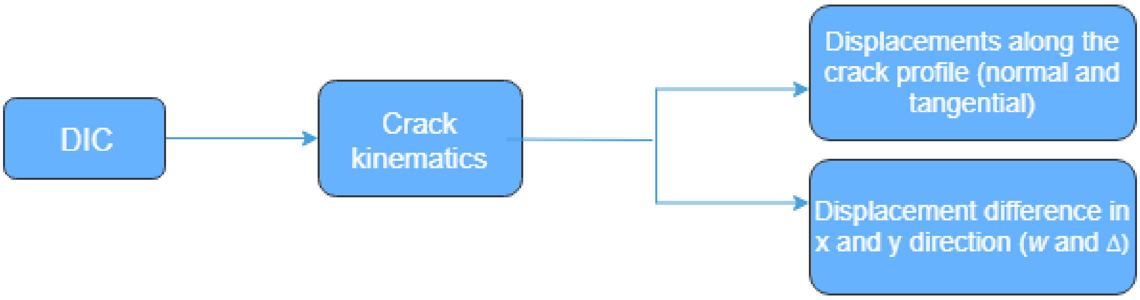

Fig. 4.3.1 Division of the crack kinematics

Displacements along the crack profile (normal and tangential)

Once the crack pattern and the crack angle of each of the segments are obtained, the next step is to compute the displacements along the crack profile since these projected displacements are needed as an input for Walraven's formulation (Eq. 2.9) for the computation of aggregate interlock stresses. The algorithm developed to get these displacements requires that once the center of the crack is found, a distance R is set to find a point to the right (P_R) and to the left (P_L), as illustrated in Fig. 4.3.2a. R is an important parameter since the points (P_R and P_L) cannot be located within the pixels that conform the contour of the crack profile, choosing points adjacent to the center would lead to wrong results which would cause an overestimation of the forces transferred along the crack, this influence will be discuss further in Section 4.4.2.

Then, the displacements at each point are calculated by linearly interpolating the measurements of a pair of points P_1-P_2 for the left side and P_3-P_4 for the right side of the grid. The displacements along the crack profile can be derived from the relative displacements in the x and y direction. Fig. 4.3.2b shows the relationship between relative displacements (dx , dy) and the normal and shear displacements (n , t) and it can be calculated by:

$$\begin{pmatrix} n \\ t \end{pmatrix} = \begin{pmatrix} \sin\alpha & -\cos\alpha \\ \cos\alpha & \sin\alpha \end{pmatrix} \begin{pmatrix} dx \\ dy \end{pmatrix} \quad \textbf{(4.2)}$$

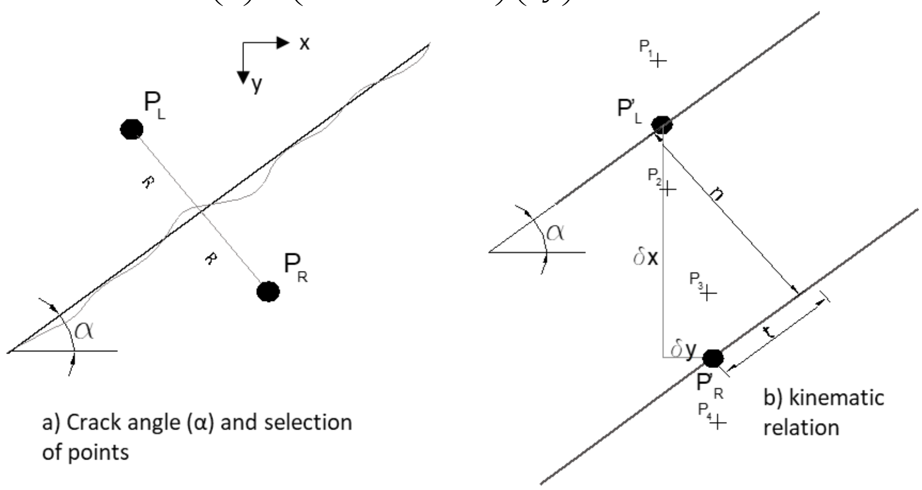

Fig. 4.3.2 Kinematic relationship of a crack

Displacement difference in x and y-direction (*w* and *Δ*)

In some mechanical models (Reineck, 1990; Yang, 2014) the crack kinematics are expressed as the displacement difference in x and y-direction. For a given crack, the crack opening *w* is defined as the displacement difference in the x-direction and the shear displacement *Δ* refers to the displacement difference in the y-direction as illustrated in Fig. 4.3.3. Moreover, *Δ* is an input parameter to describe the dowel action in Baumman and Rüsch formulation (see Eq. 2.5)

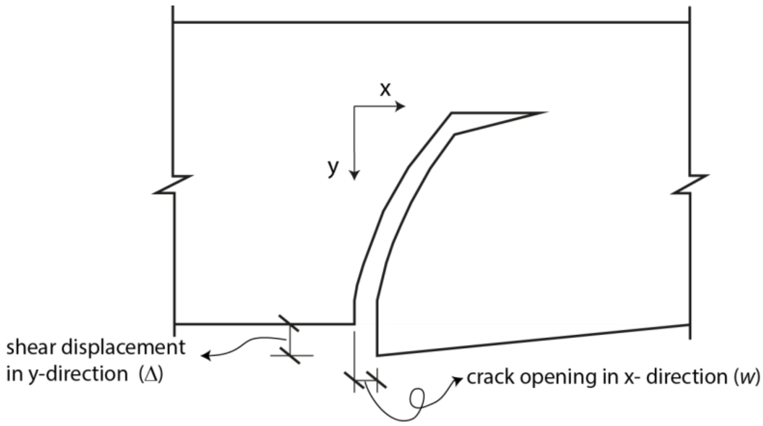

Fig. 4.3.3 Crack opening and shear displacement for a given crack

The first step to obtain these displacements is to recognize the crack of interest from the strain distribution in the longitudinal direction (ε_{xx}) and to select the level at which the information is required. Then, the ε_{xx} distribution along the longitudinal direction of the beam is plotted (see Fig. 4.3.4b), the peaks represent the center of a crack and the location of the two measuring points to the left and right can be determined considering that whenever the strains become zero the edge of the pixels that conform the contour of crack is found. An example of the measuring points is given in Fig. 4.3.4 for H401A.

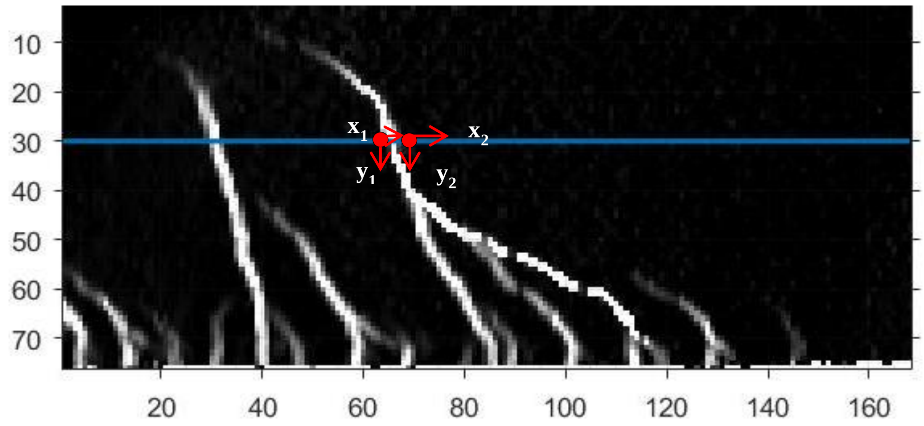

a) ε_{xx} distribution to identify the cracks

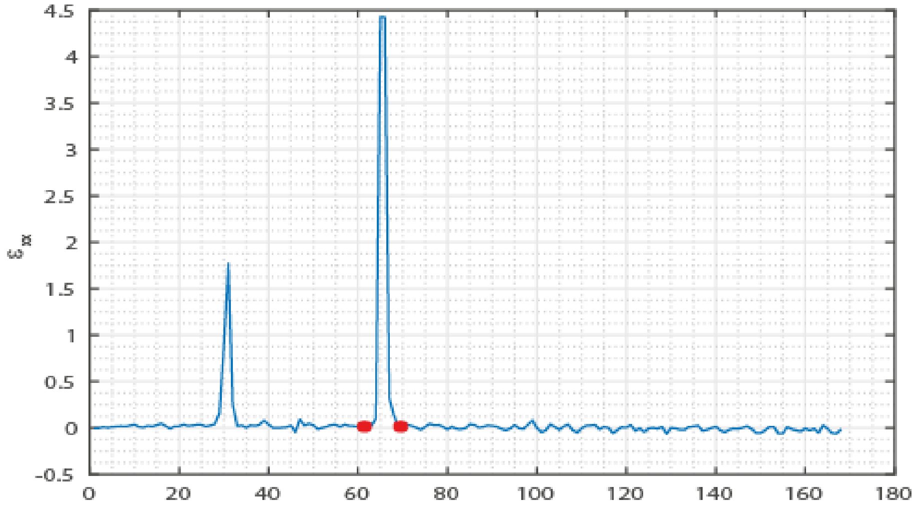

b) ε_{xx} distribution along the longitudinal axis of the beam at the selected level

Fig. 4.3.4 Strain distribution ε_{xx} and selection of points for *w* and *Δ*

4.4 Unit 4: Shear transfer mechanisms

The algorithm developed to calculate the contributions from the shear transfer mechanisms uses as an input the crack profile and kinematics of the final critical shear crack of each specimen, which is obtained from the DIC results.

The forces considered to be acting along the shear flexural crack are illustrated in Fig. 4.4.1:

- V_c shear transfer in the uncracked concrete
- V_{ai} aggregate interlock
- V_d dowel action.

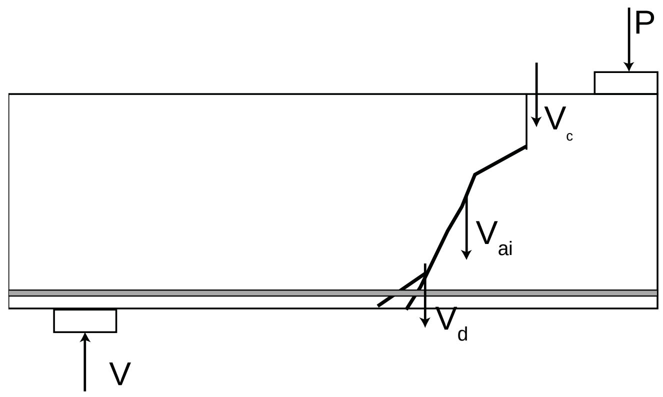

Fig. 4.4.1 Shear transfer mechanisms

The methodology followed to calculate the amount of shear transferred is summarized in the flowchart below and it is based on the measured crack kinematics and using the constitutive models described in Chapter 2.

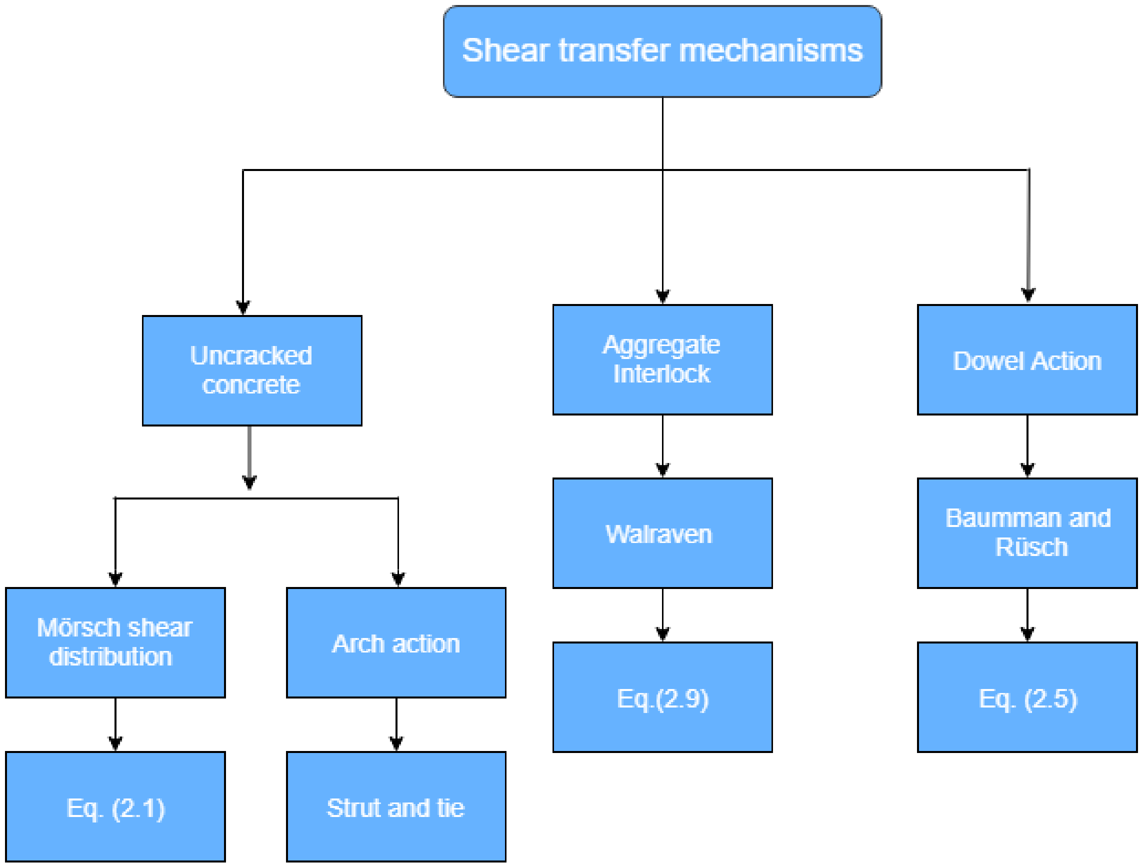

Fig. 4.4.2 Methodology to calculate the contribution of the considered shear transfer mechanisms

In the following subsections, the methodology will be explained in more detail.

4.4.1 Uncracked concrete compression zone

The contribution of the uncracked concrete zone is computed depending on the development of the flexural cracks. When a tooth-like structure is observed (see Fig. 4.4.4) and the variation of the internal forces can be assumed to be acting over a constant lever arm, the shear is calculated with Mörsch's formulation (Eq. 2.1). In this case, the height of the uncracked compression zone is computed from the coordinates of the crack profile and the lever arm is taken as $0.9d$.

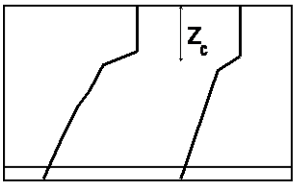

Fig. 4.4.3 Tooth-like structure

On the other hand, when the internal forces are considered to be acting over a variable lever arm and an arch structure develops, its contribution is calculated from the section located at the tip of the critical crack (see Fig. 4.4.4). This is performed by computing the strains in the longitudinal direction (ε_x) using the nodal displacements obtained from the DIC measurements considering one four-node element at the compression zone with a width of approximately 70 mm and implementing the strain-displacement relationship given in Eq. (2.27) .

The ε_x strain is used to calculate the concrete horizontal force N_c as:

$$N_c = \varepsilon_{xx} E_c A_c \qquad \textbf{(4.3)}$$

where,

- E_c is Young's modulus of concrete
- A_c is the area of the compression zone

Assuming N_c is acting at a distance equal to $1/2z_c$ from the top compressive fiber, the vertical component of the force acting in the uncracked concrete zone is calculated by:

$$V_c = N_c \tan(\beta) \qquad \textbf{(4.4)}$$

where

- β is the angle of the direct strut that forms from the point of application of the load to the support.

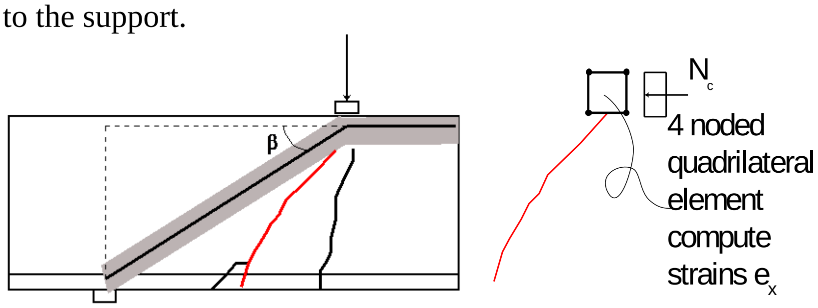

Fig. 4.4.4 Arch action and detail of the 4-node quadrilateral element

4.4.2 Aggregate interlock

The aggregate interlock stresses are computed using the normal and tangential displacements obtained directly from the DIC results as an input to Walraven's formulation (Eq. (2.16)). The forces are obtained by integrating the stresses along the crack profile. Additionally, to the two cases presented for aggregate interlock in Chapter 2, a third case is included to assume that no aggregate interlock stresses are active when the crack width is smaller than 0.1 mm. This with the aim of considering that the sections with small crack widths are closed and avoid overestimation of the forces.

During this analysis, it was noted that the results of aggregate interlock are sensitive to the magnitude of the distance k. This sensibility was studied by analyzing the influence of R on the aggregate interlock forces for a given crack profile. As an example, the results for specimen H401A using the crack pattern shown are given in the following figure.

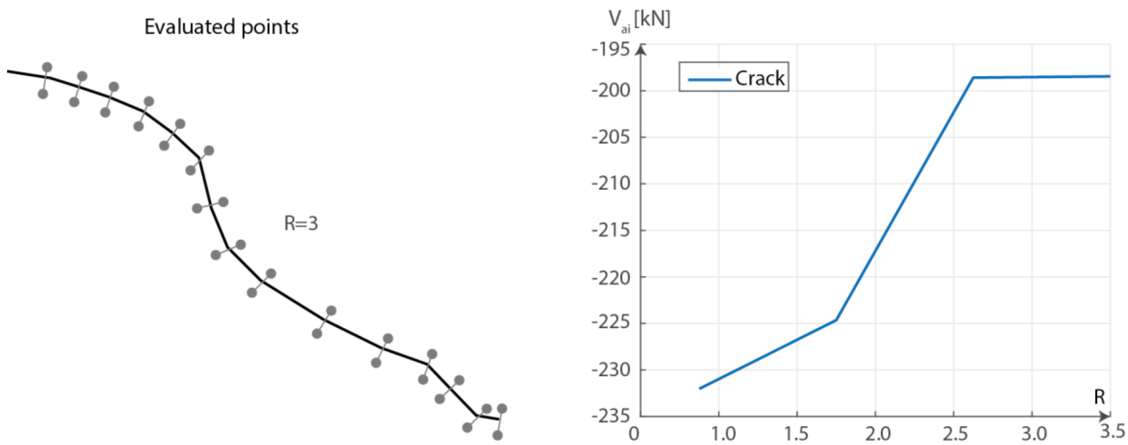

Fig. 4.4.5 Crack profile (Left) and influence of R for aggregate interlock forces (Right)

As it can be observed, as the value of the parameter R increases, at first there is a linear decrease in the aggregate interlock forces but after a value of R is reached, the aggregate interlock forces become constant with respect to any further increment of the value of R. In this case, R is chosen to be equal to 3. It is important to note that the units of R are based on grid points or positions where displacements are computed. This analysis was always performed before computing the aggregate interlock forces to choose the most suitable value for each case. The range of R in the tested specimens is between 1.2 and 3.5. This shows that choosing two points close to the center of the crack results in inaccurate displacements that produce an overestimation of the aggregate interlock forces. The displacements must be located at a reasonable distance from the center.

4.4.3 Dowel action

The contribution of the dowel action is calculated using Baumman and Rüsch formulation (see Eq. (4.5)). The vertical displacement (Δ) used as an input to the equation is obtained directly from the DIC results as the displacement difference in y-

direction of a pair of points located at the reinforcement level. The model assumes a linear elastic behaviour up to a Δ of 0.08 mm, after that, the shear force is constant with respect to any further shear displacement. Thus, when $\Delta > 0.08$ mm, V_d is equal to V_{dmax} and calculated using Eq. (2.4).

5 Results

In this section, the results from the analysis of the failure modes and the shear transfer mechanisms will be presented. The results are based on ten beams which represent the failure modes observed in the test series.

5.1 Test results

5.1.1 Typical failure modes

In the tested beams, four types of failure modes were typically observed: Flexural shear failure, flexural failure, shear compression failure, and dowel failure. Further explanation will be given in the following subsections.

5.1.1.1 Flexural Shear failure

In this thesis, the shear failure is referred to as a flexural shear failure, since it denotes its origin. The definition is that a critical inclined crack originates from a flexural crack and then develops two secondary branches (see Fig. 5.1.1), one at the rebar level approaching the support and the other at the compression zone. The specimen loses its capacity when the unstable secondary branches develop.

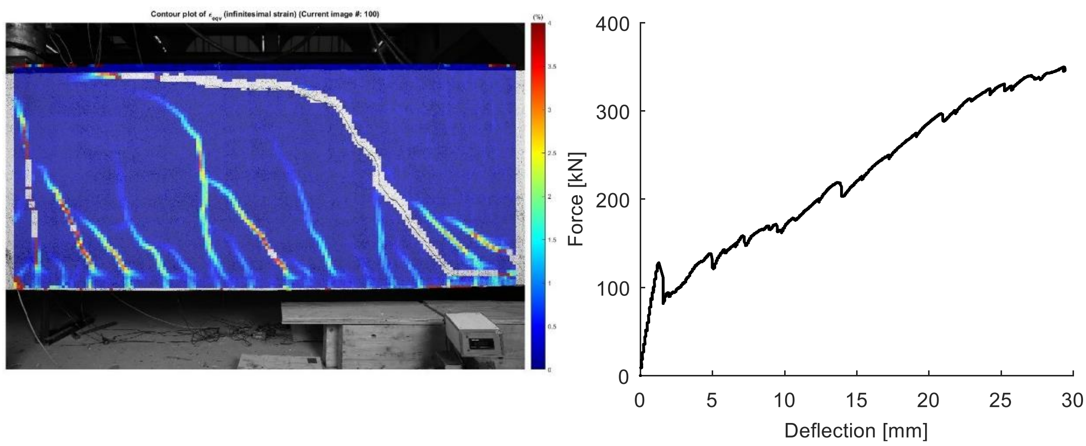

Fig. 5.1.1 Flexural shear failure test H403A. Equivalent strain distribution an instant before failure (Left). Load vs deflection (Right)

5.1.1.2 Flexural failure (yielding of tensile reinforcement)

The flexural failure mode is defined by the yielding of the tensile reinforcement during the loading process. Once this failure mode was obtained, the specimen was unloaded, and the point load was moved. The same procedure was repeated until the flexural shear failure was obtained.

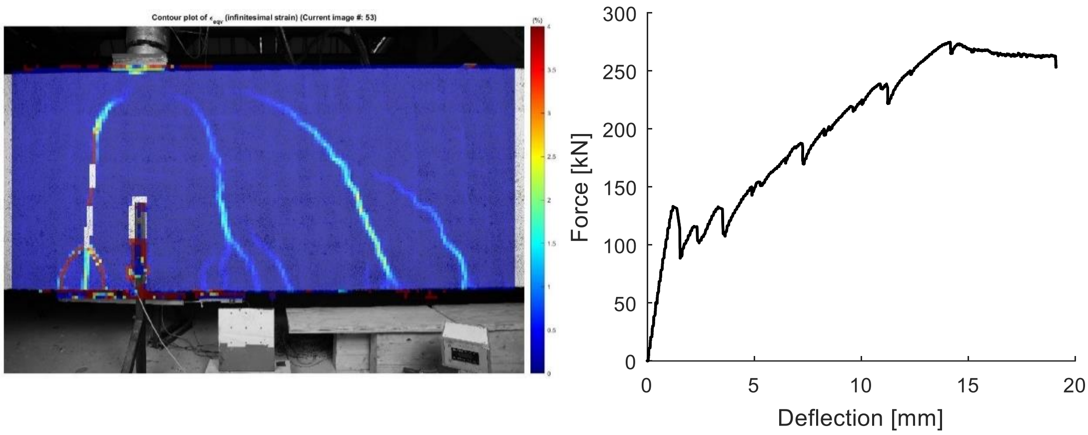

Fig. 5.1.2 Flexural failure test I604A. Equivalent strain distribution an instant before failure (Left). Load vs deflection (Right)

5.1.1.3 Shear compression failure

This failure mode occurs when the specimen does not lose its capacity after the formation of the flexural shear crack. Instead, a compressive strut is formed from the loading point to the support, allowing a much higher load level.

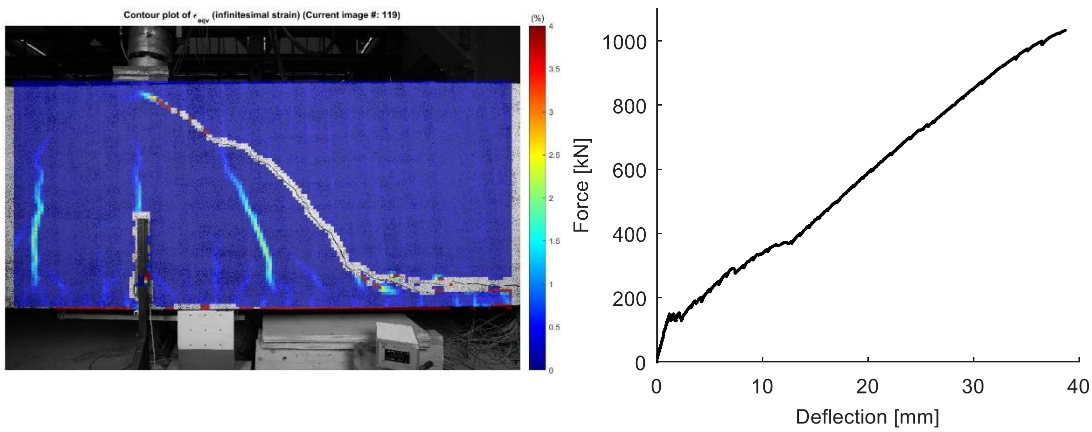

Fig. 5.1.3 Shear compression failure test H122A. Equivalent strain distribution an instant before failure (Left). Load vs deflection (Right)

5.1.1.4 Dowel failure

In this failure mode, the detachment of the tensile reinforcement from a flexural crack close to the loading point was observed. Due to the proximity to the loading point, no secondary branch was developed in the compression zone and during the loading process, the applied load could not increase further, while the dowel crack developed on the longitudinal direction until it reached the support, see Fig. 5.1.4. In this failure mode, the detachment is attributed to the dowel action.

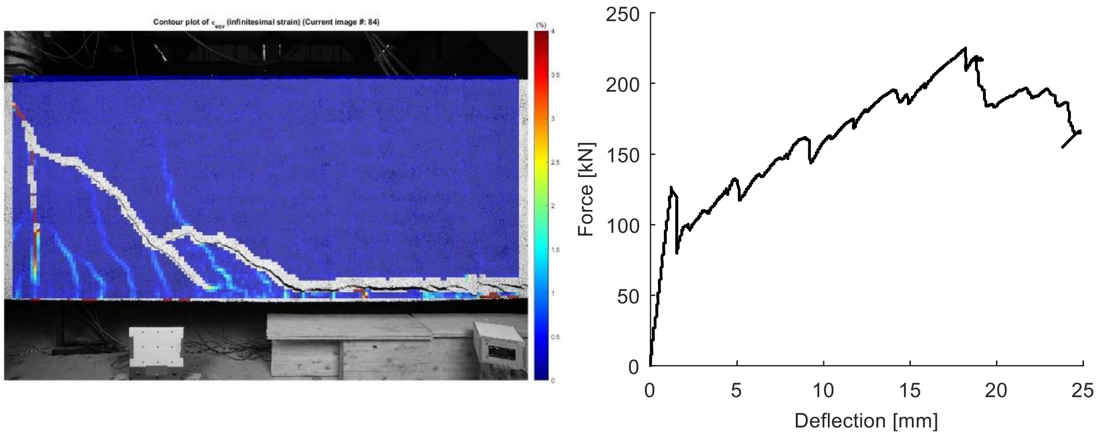

Fig. 5.1.4 Crack pattern after dowel failure beam H352A

5.1.2 Summary of test results

In total 15 tests were carried out, 8 of them presented a flexural shear failure, 1 was shear compression, 1 dowel failure and the remaining were flexural failure. From the DIC results, it was possible to identify the shear force level just before the opening of the unstable crack along the reinforcement level and it was denoted as V_{cr} .

Table 5.1-1 shows a summary of the 10 specimens considered. In the table, the values of $x_{cr,b}$ and $x_{cr,m}$ indicate the position of the critical flexural shear crack at the reinforcement level and at the middle of the beam as indicated in Fig. 5.1.5. x_{crm} is used to calculate the resulting shear force V_u or V_{cr} considering the self-weight of the specimen at the location of the shear crack. In the table, a is the shear span, d is the effective depth, ρ is the longitudinal reinforcement ratio, P_u is the maximum load and P_y is the load at which the yielding of the reinforcement is observed.

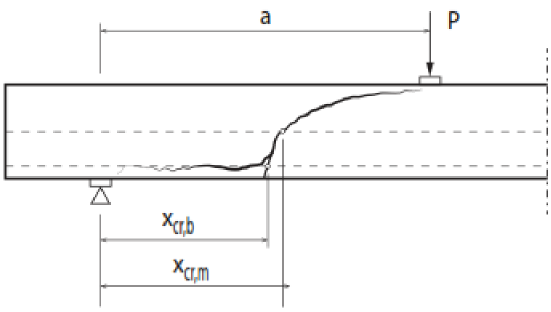

Fig. 5.1.5 Definition of the shear crack location at the bottom reinforcement and center of the specimen

Table 5.1-1 Summary of tested specimens

Test no.	P_u [kN]	P_y [kN]	Mode	$x_{cr,m}$ [mm]	$x_{cr,b}$ [mm]	V_u [kN]	V_{cr} [kN]
H301A	222		S	2530	2260	**136.0**	
H352A	225		D	3989	2979	**116.9**	
H401A	264		S	3070	2350	**142.5**	
H402A	322		S	3180	2860	**172.9**	
H403A	350		S	2563	2161	192.4	**142.4**
H404A	269		S	2949	2277	**158.4**	
H121A	341		S	1955	1710	**236.7**	
H122A	1032		SC	2160	1710	695.6	**190.9**
I602A	274		F				
I602B	279		F				
I602C	298	295	F	2144	1851		**174.4**
I602D	337	333	F				
I602E	40		S	2144	1851	36.6	
I603A	299	298	F	2216	1691		**157.1**
I603B	5		S				

These results show that the test that presented dowel failure had the lowest capacity of this test series and it is presented in the specimen with a reinforcement ratio of less than 0.4 %.

Fig. 5.1.6 shows the cracking patterns of the selected beams, drawn from the DIC results taken at the final instant before failure. It can be observed that the patterns differ between the specimens, even for the beams with the same rebar configurations and *MV/d* ratios. However, the major and secondary cracks can be identified. In Fig. 5.1.6, the cracks in blue represent the major cracks; the cracks in black indicate the secondary cracks and the cracks in red are the critical shear cracks. The line in grey indicates the possible formation of the direct strut form from the location of the applied load to the support.

The change in the inclination of the cracks is linked to the *MV/d* ratio of the cracked cross-section, larger *M/Vd* results in steeper cracks, this will be discussed further in Chapter 6.

As it can be seen in Fig. 5.1.6, the location of the tip of the critical shear crack determines whether the direct strut of the arch action develops or not. Regarding the beams reinforced with plain bars, the flexural cracks develop at cross sections closer to the loading point, allowing the formation of a direct strut however since they presented a flexural failure, the loading point was moved, and they finally failed by flexural shear failure.

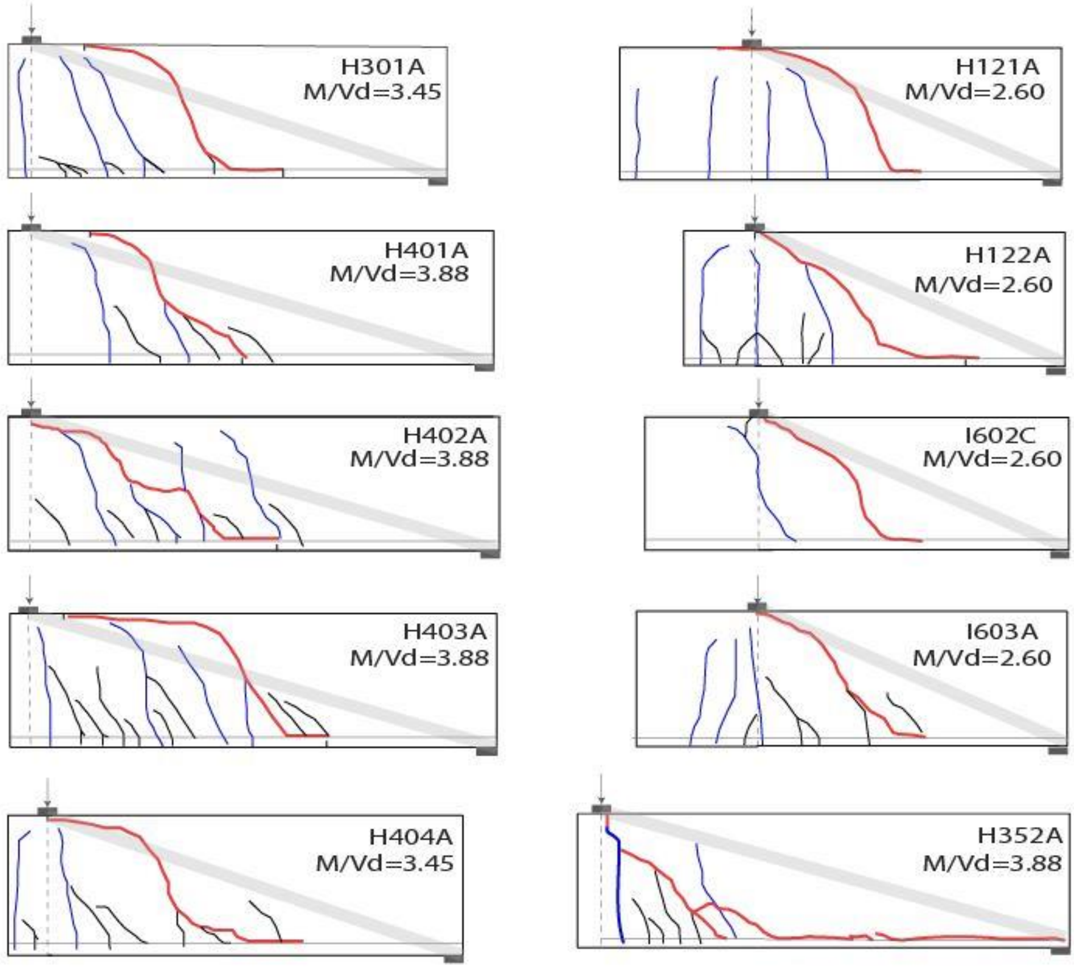

Fig. 5.1.6 Observed cracking patterns for selected beams at an instant before failure.

In the following sections, selected examples of the different failure modes will be presented and discussed further.

5.2 Flexural shear failure

H401A

From the eight test that presented a flexural shear failure, test H401A is selected since it failed in shear just after the formation of the critical inclined crack. As it can be observed in Fig. 5.2.1, the critical inclined crack originated from a major crack that merged into two secondary cracks, which allowed larger displacements. Then, the major crack developed two secondary branches one approaching the support and the other approaching the load point. The measurements on the crack relative displacements show that large tangential displacements occurred at the top steep part of the crack, which indicates that aggregate interlock stresses are activated in this region. This can be checked by looking at the shear and normal stresses computed along the critical crack profile. For example, Fig. 5.2.2 shows the shear and normal stresses at the instant just before failure, it can be observed that aggregate interlock stresses are active in the steep and upper sections of the crack profile.

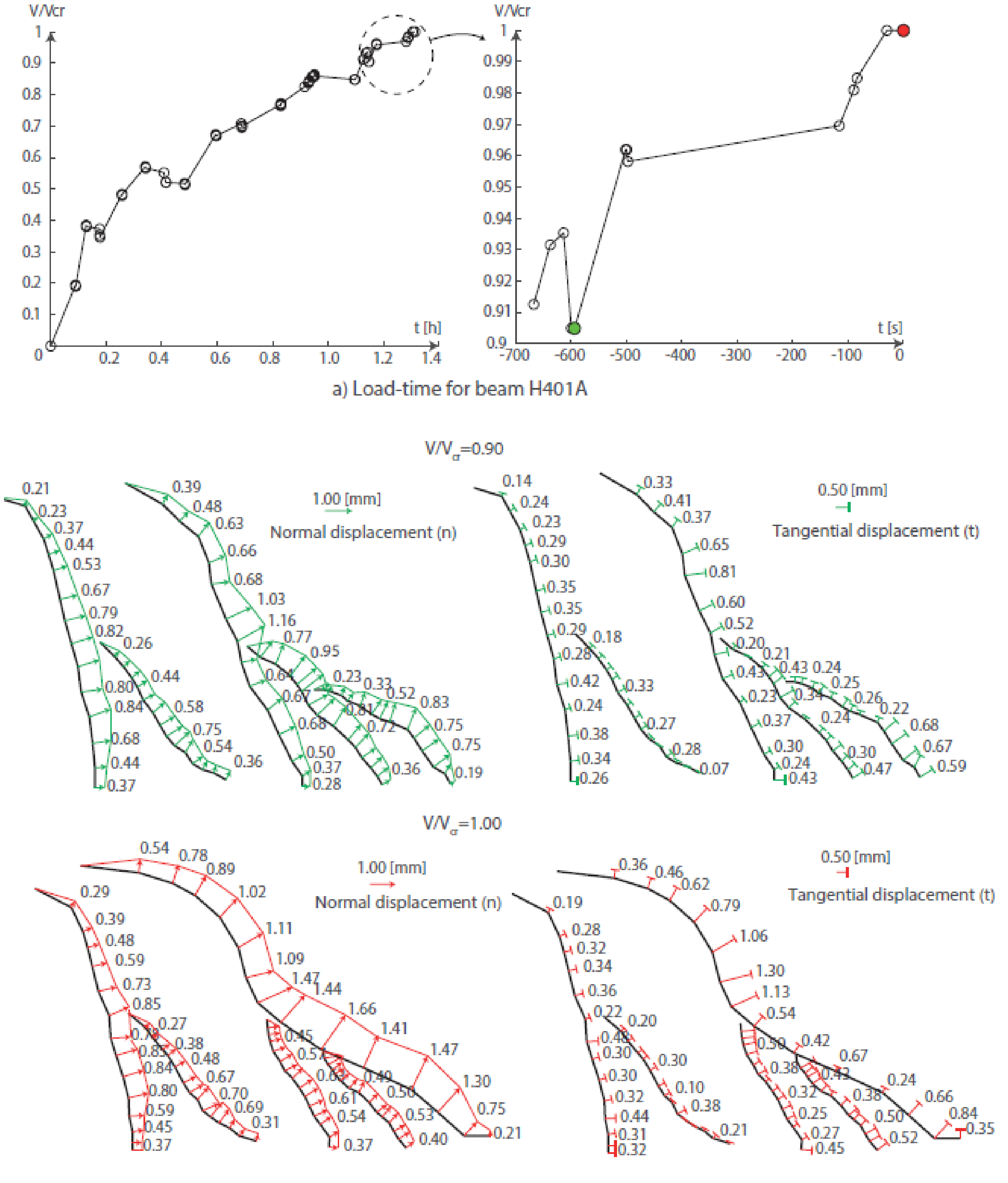

Fig. 5.2.1 a) Loading procedure and b) development of normal (left) and tangential (right) displacements for H401A

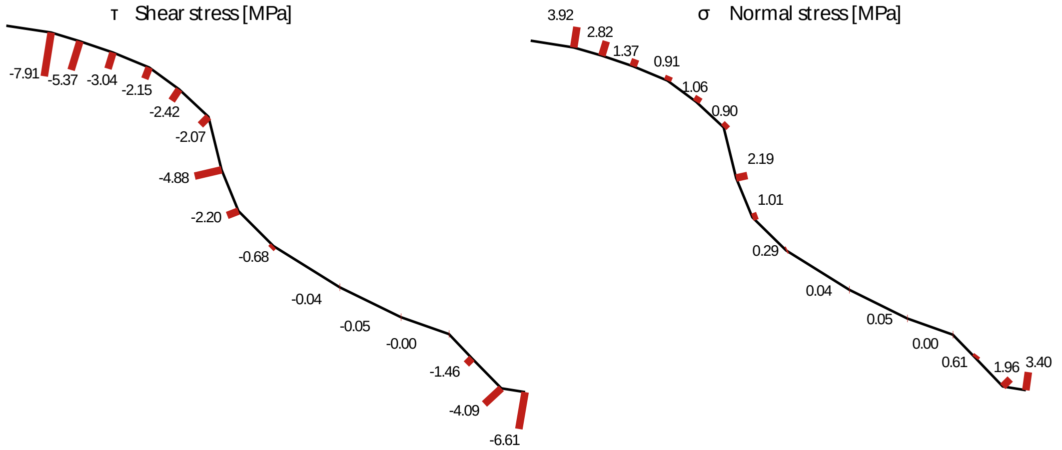

Fig. 5.2.2 Shear and normal stresses along the crack profile for H401A at V/Vcr=1

Investigating further, the contribution of the shear transfers mechanisms is computed based on the profile of the critical shear crack obtained from the moment just before failure and considering that the crack pattern of the beam resembles a tooth-like structure, the contribution of the uncracked concrete zone was calculated using Mörsch's formulation with a constant z_c of 100 mm found from the coordinates of the critical crack profile. Fig. 5.2.4 shows the contribution of the considered shear transfer mechanisms during the loading procedure, for comparison, the shear force is also plotted and Fig. 5.2.3 illustrates the crack evolution at the chosen representative load levels.

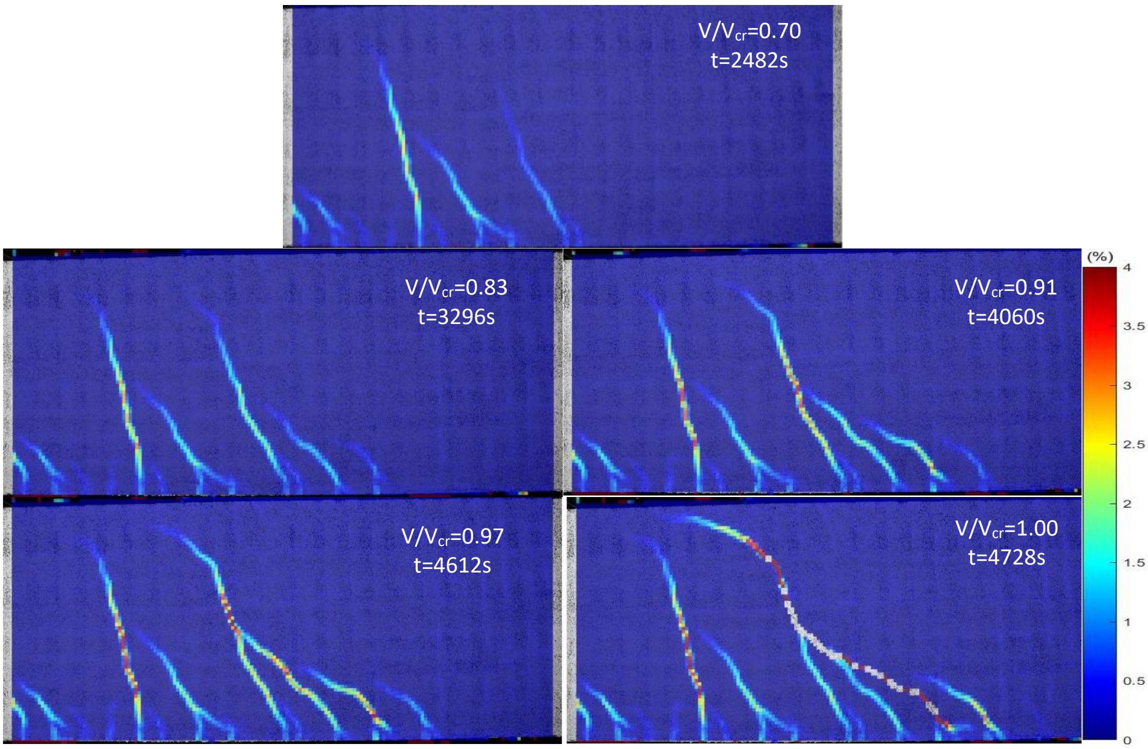

Fig. 5.2.3 Equivalent strain distributions at some representative load levels for beam H401A

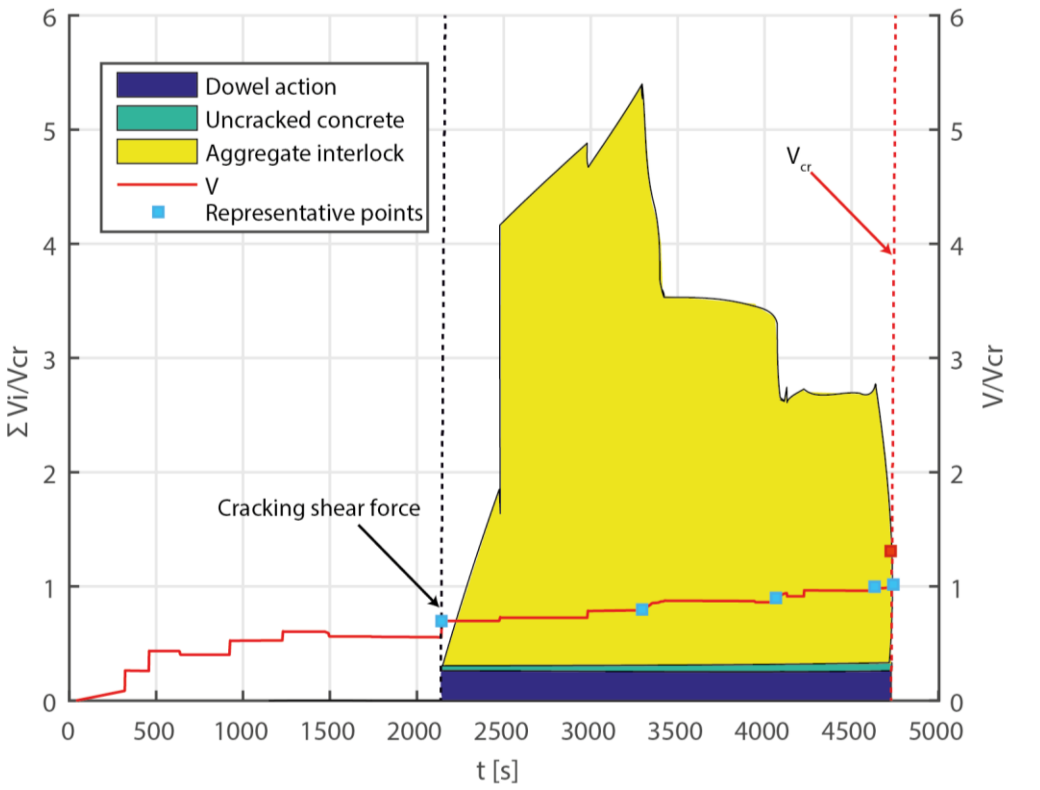

Fig. 5.2.4 Contribution of shear transfer mechanisms for H401A vs time

It can be observed that shear is mainly carried by aggregate interlock, which is activated just after the cracking shear force is reached. The first peak of the aggregate interlock forces corresponds to the formation of the secondary cracks and it is followed by a sudden decay, then the contribution stays constant until the major crack merges with the secondary cracks, at this moment the relative displacements between the crack increase and as a result, the force from aggregate interlock decreases significantly. Comparing the contribution of the different transfer mechanisms with the capacity of the beam at this final moment, the result is $\Sigma V_i/V_{cr}$=1.3.

H403A

Another specimen that presented a flexural shear failure was the beam H403A, however, this specimen could increase about a 7% of the load after V_{cr} was reached, while the secondary branches gradually developed (see Fig. 5.2.5). The crack pattern of this beam shows that 3 major cracks developed in the shear span and according to the relative displacements comparable aggregate interlock stresses were active along them before V_{cr} was reached. Investigating further, two of these potential critical shear cracks are considered: Crack 1, which is a major crack that did not become governing and Crack 2, which is the critical shear crack. Fig. 5.2.8 shows the contribution of aggregate interlock during the loading procedure for both cracks and the applied shear force. The crack profiles considered for the computation of these results are highlighted in Fig. 5.2.6.

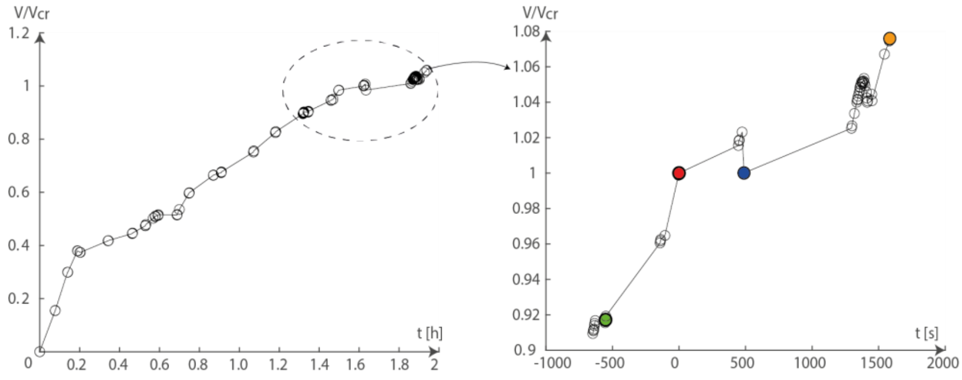

a) Load-time for beam H403A

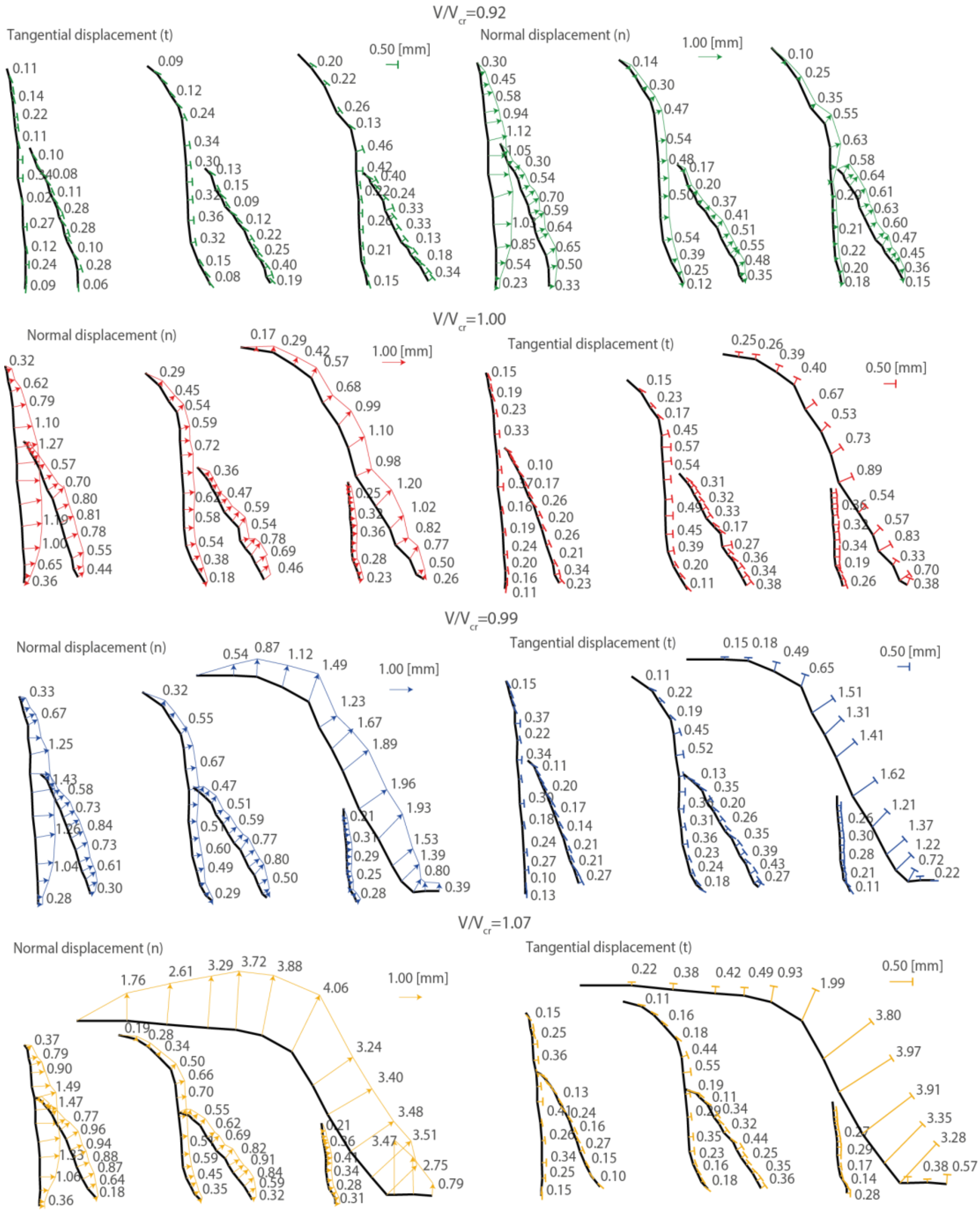

b) Crack kinematics for beam H403A

Fig. 5.2.5 a) Loading procedure and b) development of normal (left) and tangential (right) displacements for H403A

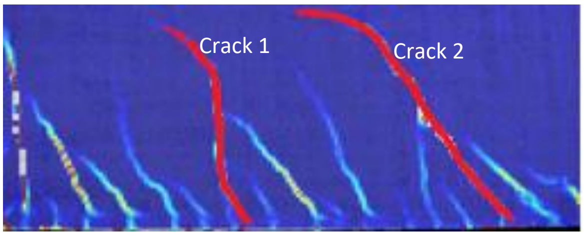

Fig. 5.2.6 Identification of Crack 1 and Crack 2 for beam H403A

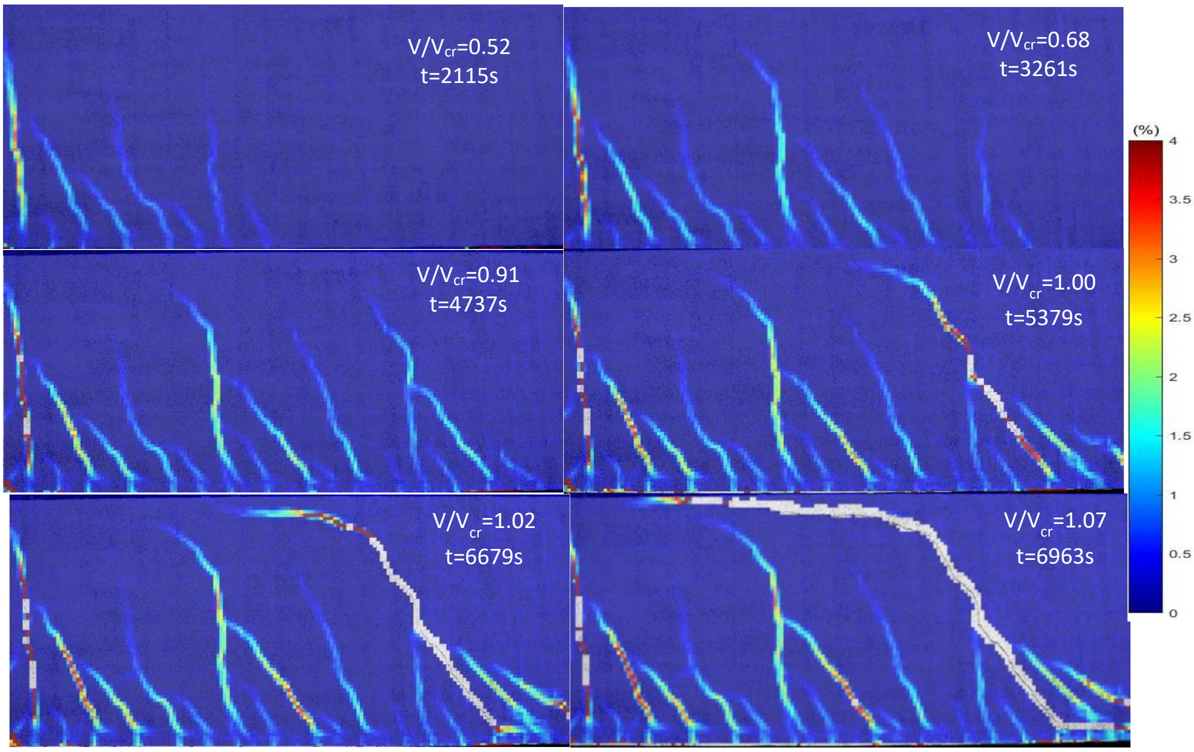

Fig. 5.2.7 Equivalent strain distributions at representative load levels for beam H403A

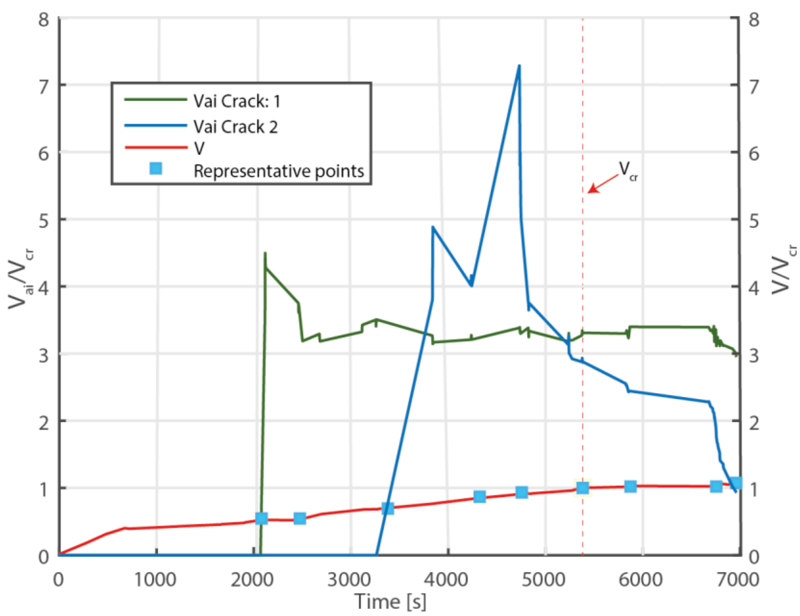

Fig. 5.2.8 Contribution of aggregate interlock for H403A vs time

It can be observed that just after the cracking shear force is reached both cracks present a comparable amount of aggregate interlock contribution. However, while Crack 1 presents a constant amount of aggregate shear contribution, which is about three times more than the applied shear force, Crack 2 presents a peak of high stresses that correspond to the moment when the major crack joins the associated secondary crack followed by a decay in the contribution that accentuates after V_{cr} is reached. At the moment just before failure, the contribution of Crack 1 was less than the applied shear.

These differences can be explained by looking at the crack stresses along the crack profile, for instance, see Fig. 5.2.9. Crack 1 due to its steep shape was able to develop aggregate interlock stresses along its full crack profile, while for Crack 2 the stresses are mainly localized in the top section of the crack. In general, shear stresses are higher when the crack width is small, where the larger contact area can be expected, and this will result in the largest contribution. It is important to note that the crack kinematics results showed that Crack 1 presented significantly less amount of normal and tangential displacements than Crack 2 after V/V_{cr}=1 and until failure.

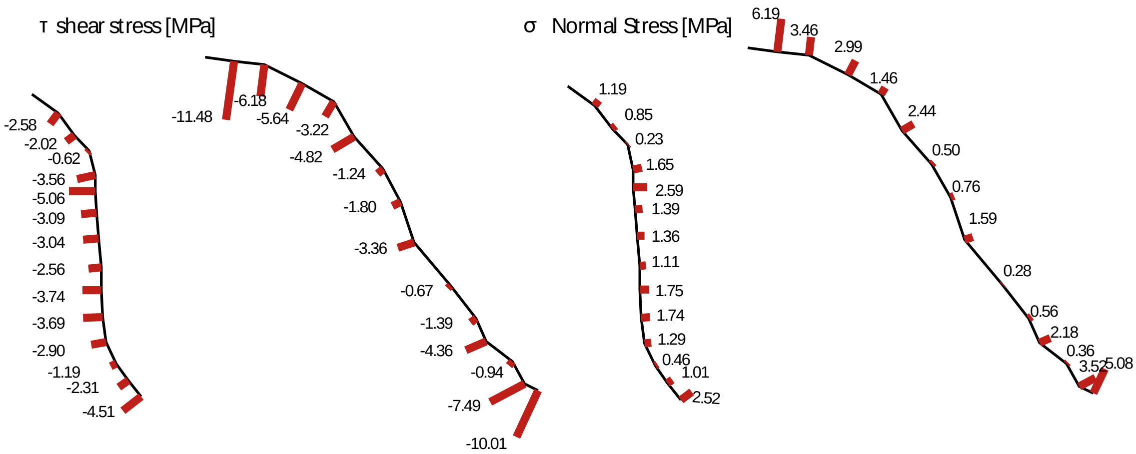

Fig. 5.2.9 Shear and normal stresses along the crack profile for H403A at *V/Vcr*=1

I603B

Specimen I603 failed in shear at a load level of just 5kN after the point load was moved 500 mm further from the support since the first test, I603A, presented a flexural failure. Investigating the causes of this sudden failure, the aggregate interlock contribution of test I603A is plotted with the applied shear force in Fig. 5.2.10. Comparing this figure with Fig. 5.2.11, it can be observed that after $V/V_{cr}=1$ the aggregate interlock contribution decreases significantly until it is equal to zero and the relative displacements between the crack faces were significantly large. Despite this, the beam did not fail and resisted even higher load levels. This is attributed to the formation of a direct strut in the uncracked concrete zone, however, when the point load was moved, the major cracks interfered with the formation of the strut and the beam failed because of the lack of aggregate interlock.

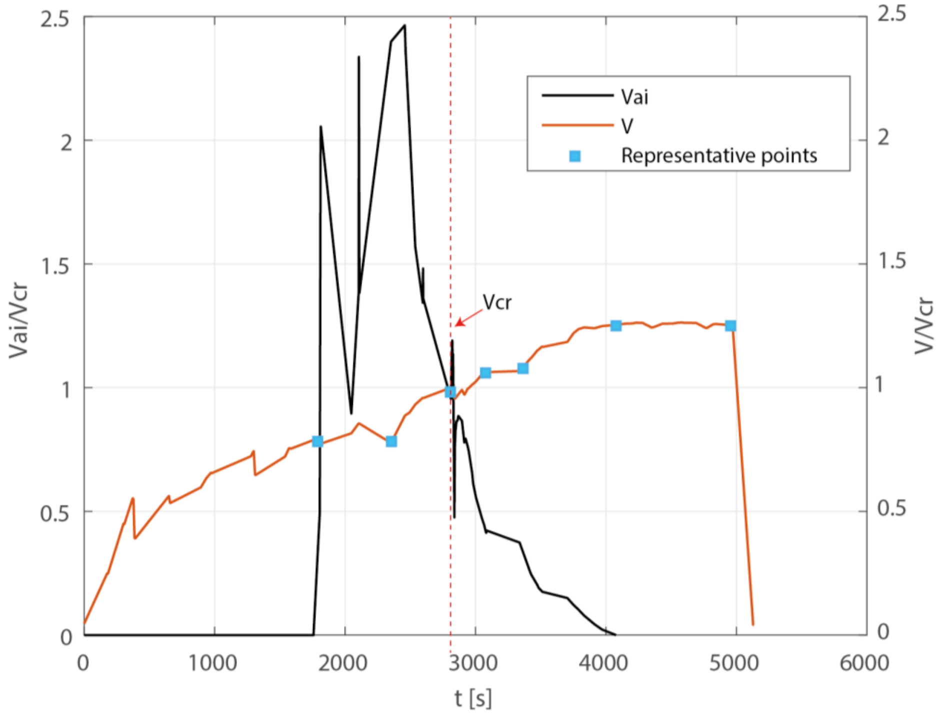

Fig. 5.2.10 Contribution of aggregate interlock for I603A vs time

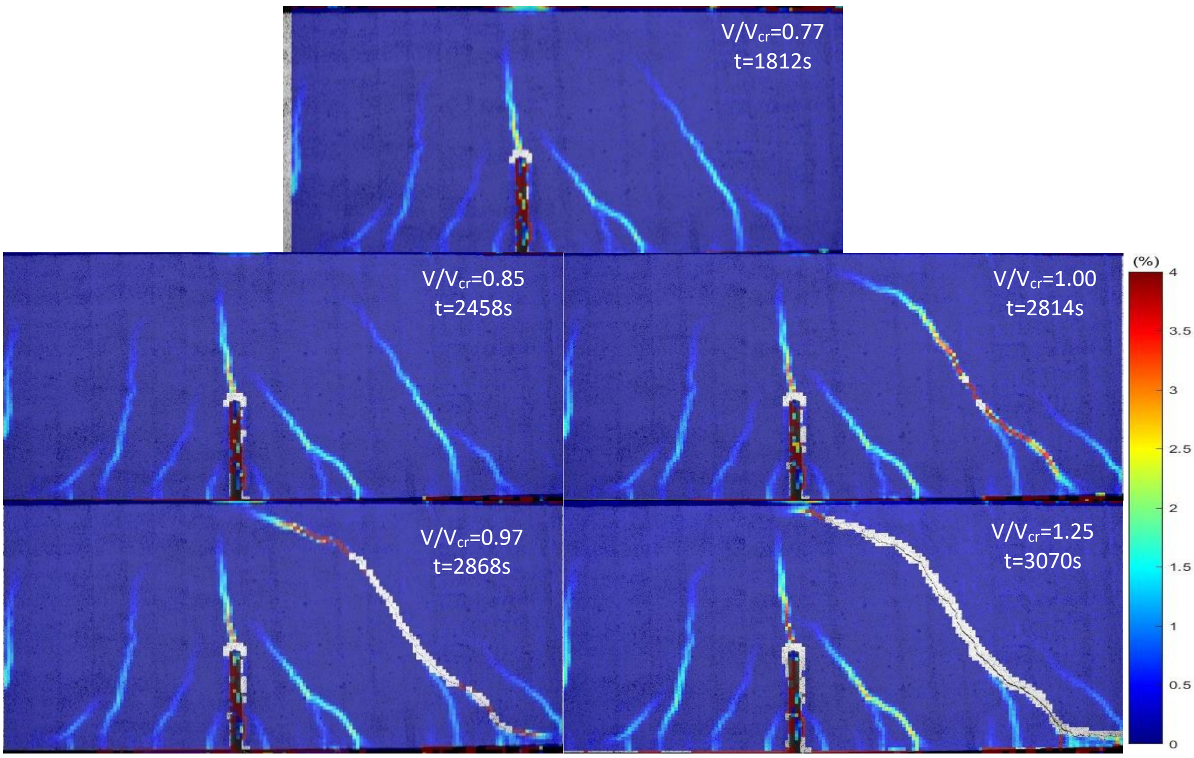

Fig. 5.2.11 Equivalent strain distributions at representative load levels for beam I603A

5.3 Shear compression failure

Specimen H122A was the only one that failed in shear compression, it can be observed that the critical inclined crack developed at an early stage during the loading procedure (approximately 30% of V_u) however the beam could resist significantly higher load levels (see Fig. 5.3.2a). The crack tip of the critical shear crack is located just under the loading plate, allowing the development of a direct strut in the uncracked concrete zone increasing the shear capacity. It is important to note that the results of the crack normal displacements are significantly high, which indicates that the contribution of aggregate interlock is minimal. Fig. 5.3.1 illustrates the shear and normal stresses along the crack profile at the moment that V/V_{cr} is equal to one. It shows that the amount of tangential stresses is almost negligible, which means less contribution of aggregate interlock.

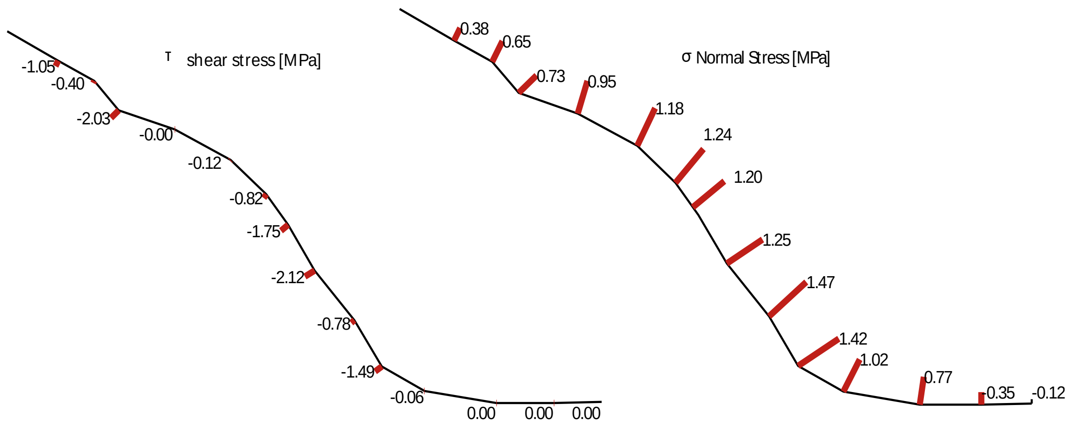

Fig. 5.3.1 Shear and normal stresses along the crack profile for H122A at V/V_{cr}=1

Fig. 5.3.3 presents the results of the contribution of each of the shear transfer mechanisms, they were calculated considering the crack profile formed at the moment just before failure. Since a direct strut developed, the contribution of the uncracked zone was computed as explained in the Section 4.4.1, considering the evolution of strains in the longitudinal direction at the section located at the top of the tip of the crack. As it can be observed in the figure, despite the contribution of aggregate interlock decreased and even became zero, the apply load was able to increase up to more than 3 times V_{cr} because the arching action became the main contributor. The beam finally failed when the contribution of arch action decreased.

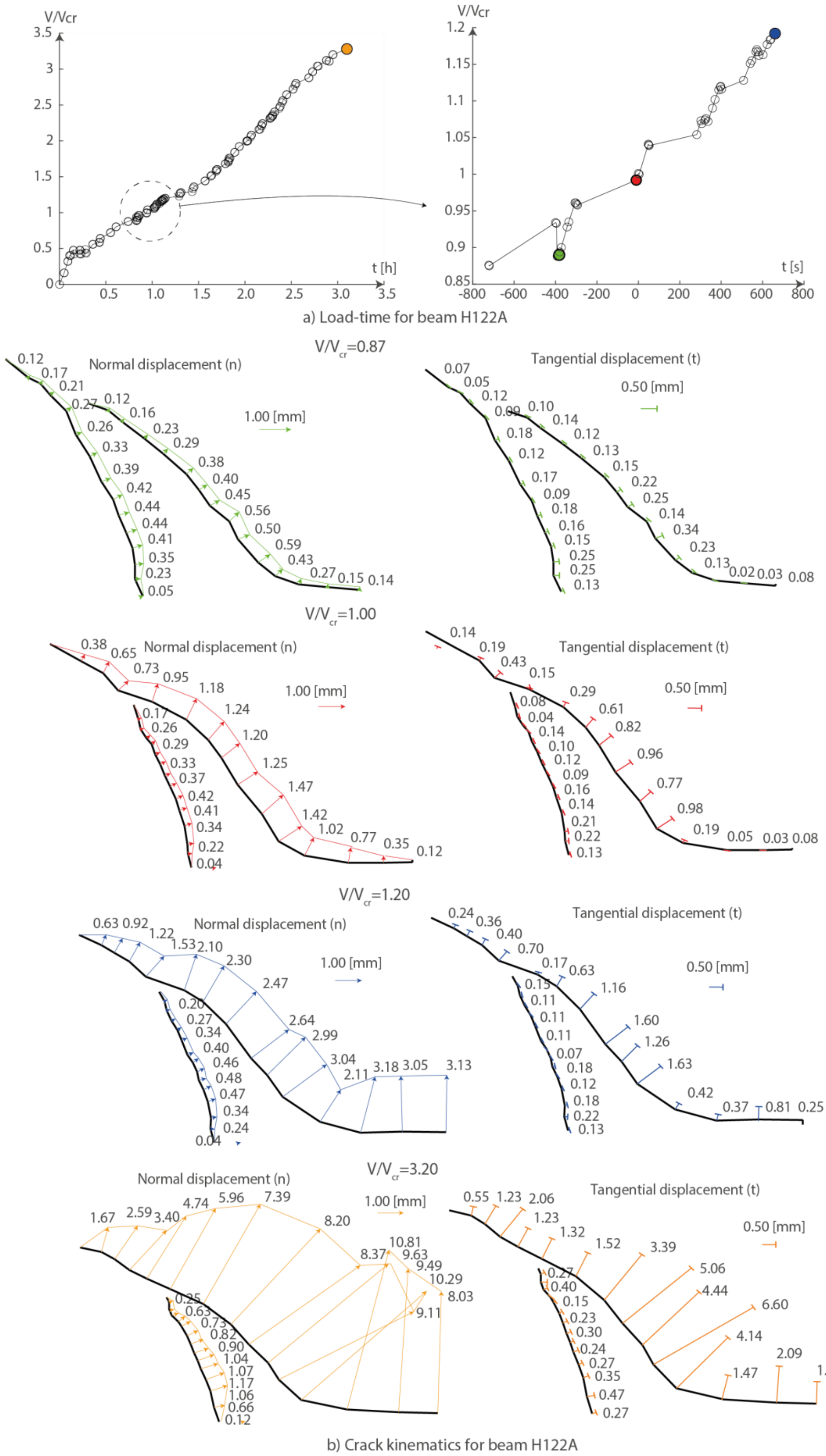

Fig. 5.3.2 a) Loading procedure and b) development of normal (left) and tangential (right) displacements for H122A

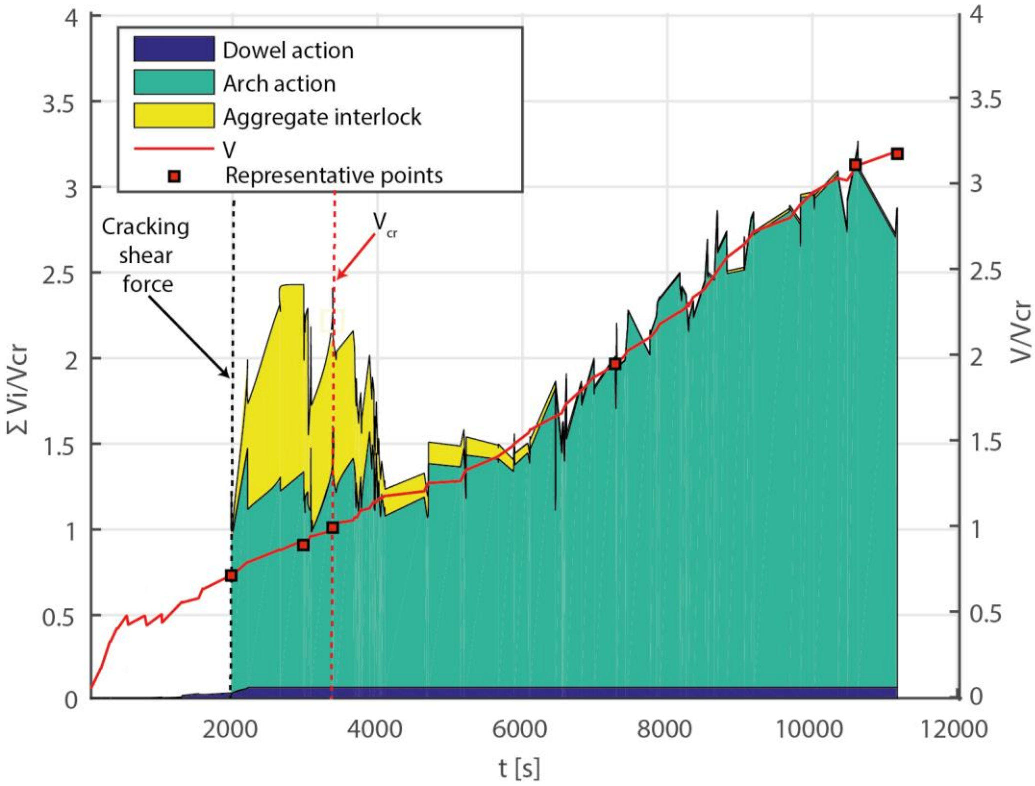

Fig. 5.3.3 Contribution of shear transfer mechanisms for H122A vs time

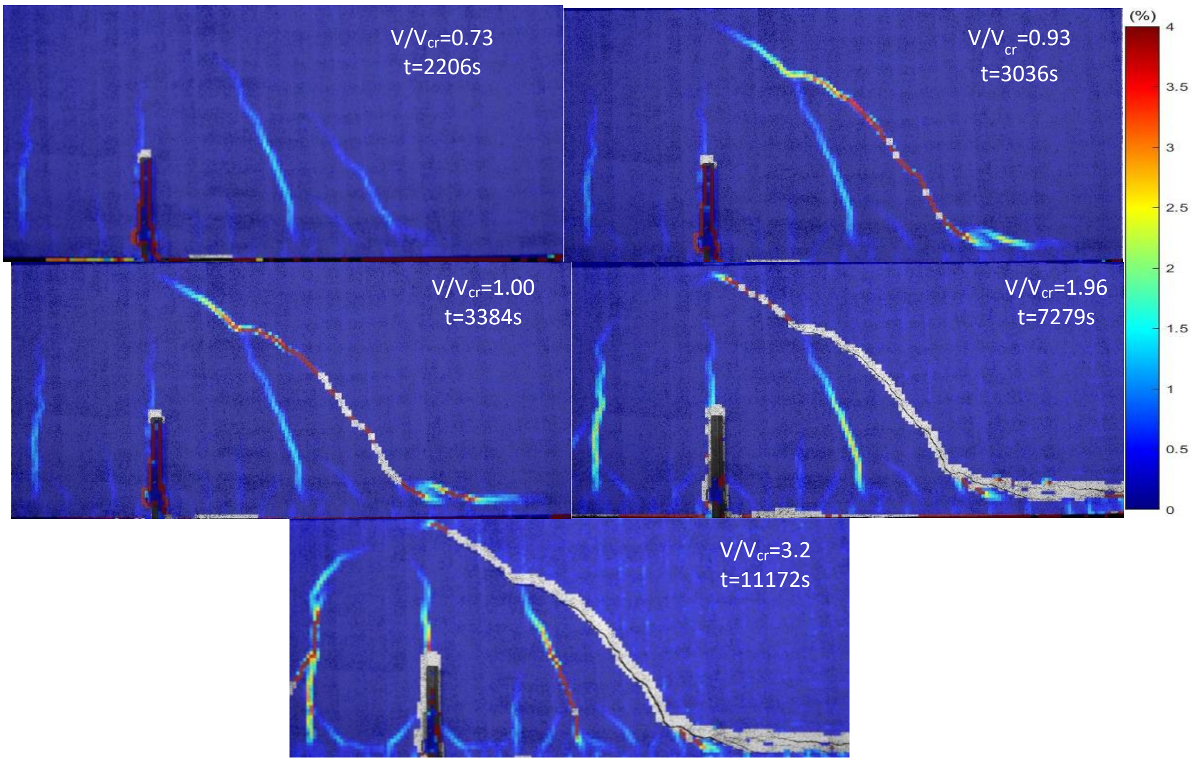

Fig. 5.3.4 Equivalent strain distributions at representative load levels for beam H122A

5.4 Dowel failure

Specimen H352A presented a dowel failure. The kinematic results are shown in Fig. 5.4.2 and represent five moments between the reaching of V_{cr} to the moment of failure during the loading procedure. Three major cracks and three secondary cracks or dowel cracks can be identified, the latter presents a pronounced inclination (average of 41°). The major crack located near the loading point presents higher displacements and as the loading procedure develops, the secondary cracks merge allowing even higher displacements. It is observed that the applied load could not increase further than the value of V_{cr} and the load dropped as the dowel crack approached towards the support at the reinforcement level. From these results, it can be assumed that the critical crack is formed by the first flexural crack and two secondary cracks and the rotation of this system can be located at the tip of the major crack (see Fig. 5.4.1).

Fig. 5.4.1 Critical crack for H352

The calculation of the contribution of each of the shear transfer mechanisms was performed considering the assumed crack profile and the contribution of the uncracked concrete zone was computed using Mörsch´s formulation with a z_c of 200 mm. The results are shown in Fig. 5.4.3. The equivalent strain distributions at representative load levels are shown in Fig. 5.4.4.

It can be observed that after V_{cr} is reached, there is a sudden decay of aggregate interlock forces followed by an attempt to increase the load but as the secondary branch opens in the longitudinal direction towards the support, the displacements increase and the aggregate interlock forces decrease until failure. It is important to note that as aggregate interlock decreases, dowel action becomes the main contributor, and this results in a relative plastic behavior.

Investigating further, in Fig. 5.4.5, the vertical displacements along the longitudinal axis of the beam at the reinforcement level are plotted for three different load levels. It can be observed that the relative displacements are considerably large. The figure shows that the blue block that is formed by the joining of the secondary cracks (see Fig. 5.4.1) is applying a force perpendicular to the longitudinal axis of the beam that causes large displacements in the vertical direction, pushing down the reinforcement and triggering the opening of the dowel crack along the reinforcement level.

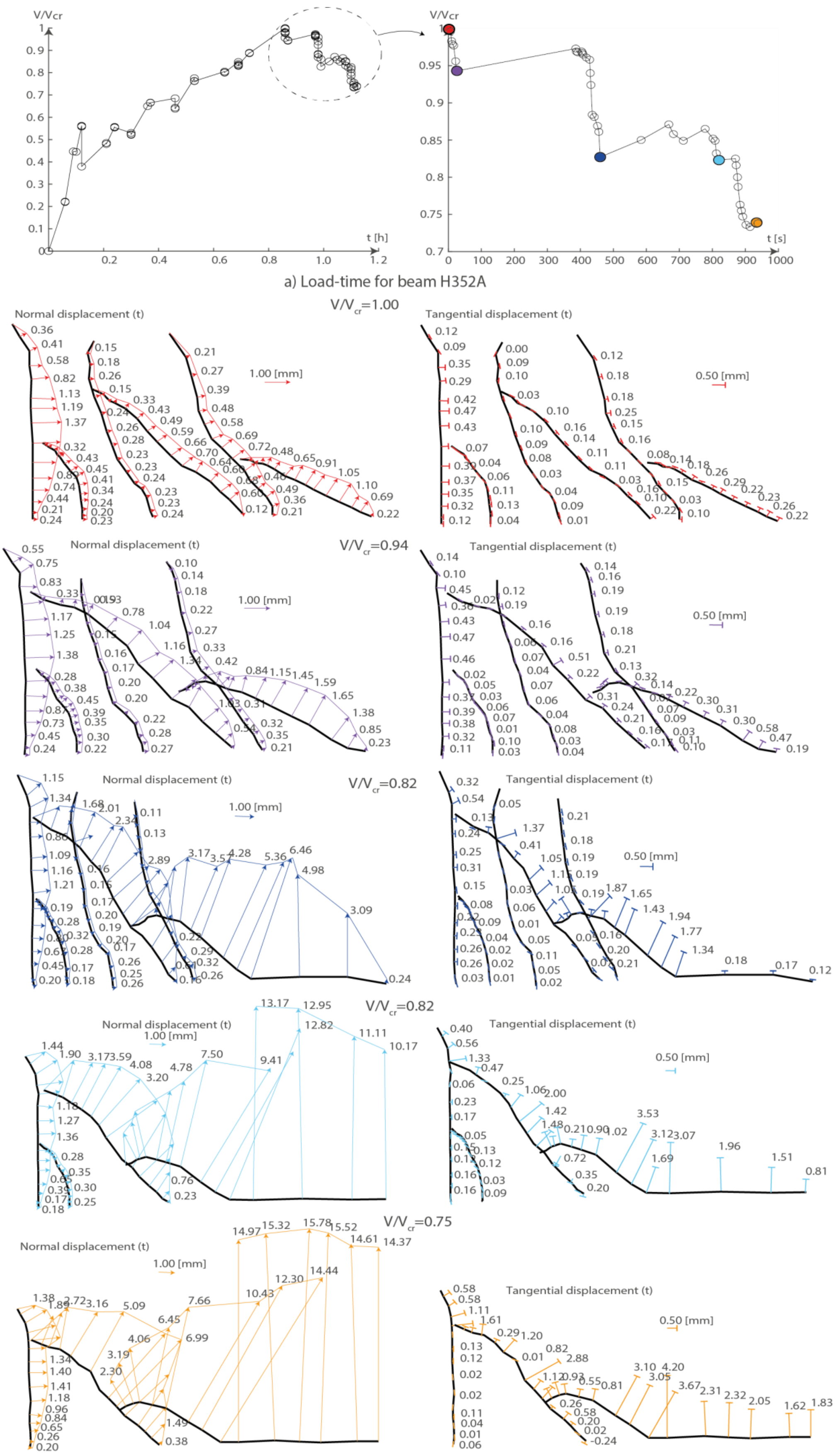

a) Load-time for beam H352A

b) Crack kinematics for beam H352A

Fig. 5.4.2 a) Loading procedure and b) development of normal (left) and tangential (right) displacements for H352A

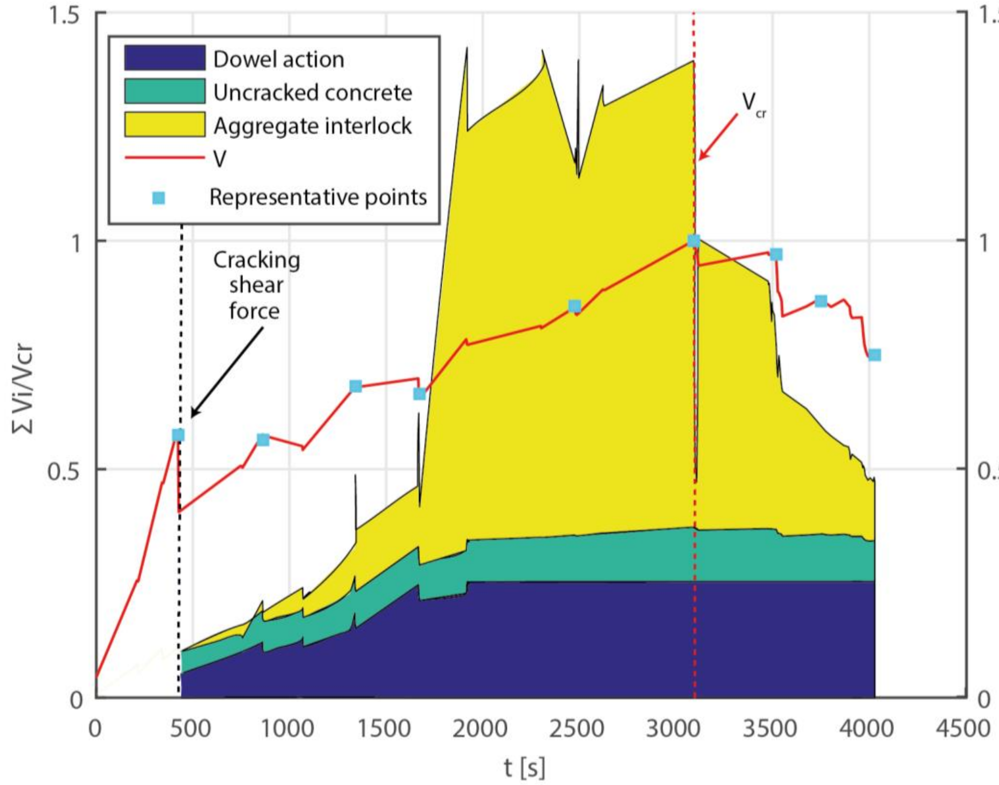

Fig. 5.4.3 Contribution of shear transfer mechanisms for H352A vs time

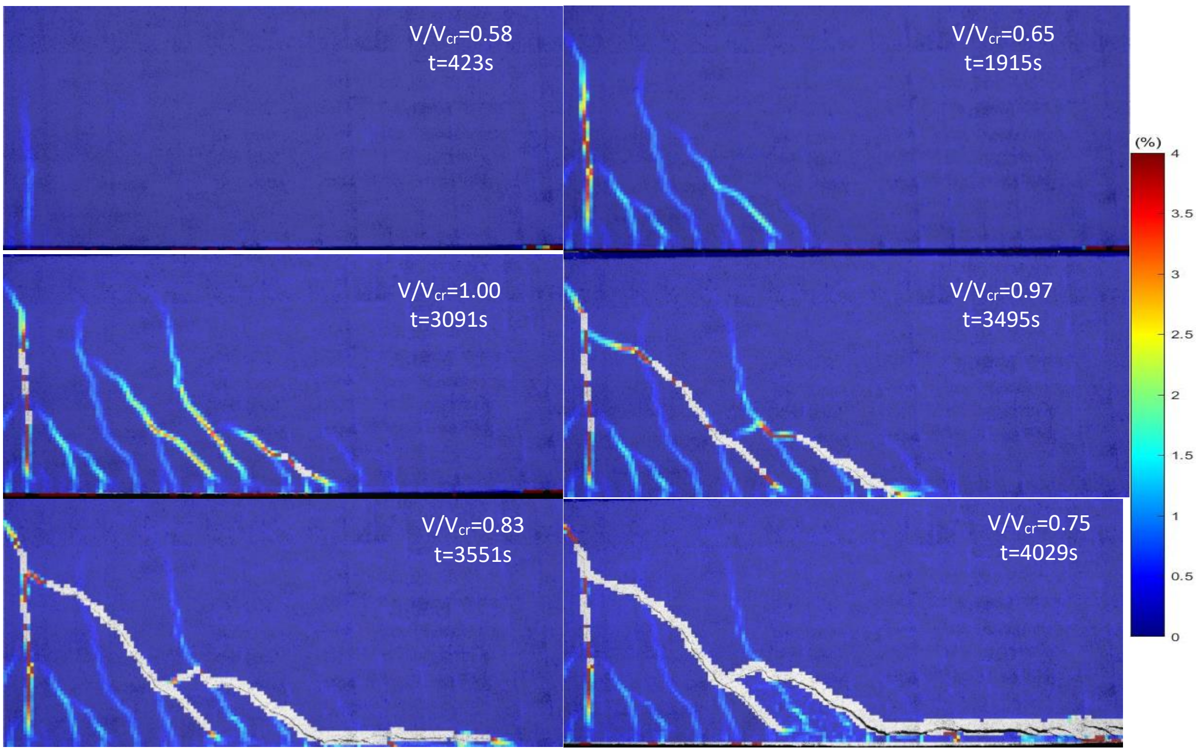

Fig. 5.4.4 Equivalent strain distributions at representative load levels for beam H352A

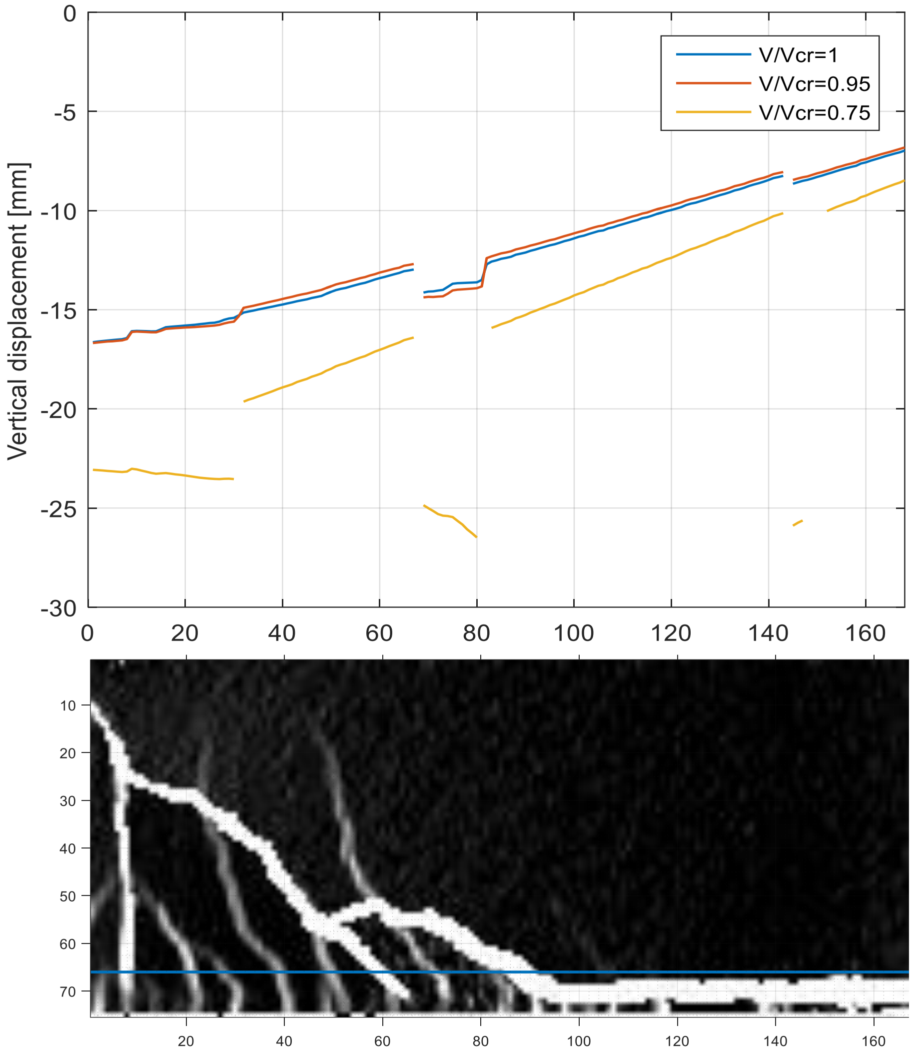

Fig. 5.4.5 Vertical displacements along the longitudinal axis of the beam H352

5.5 Discussion

This section presents the results of the calculated shear transfer mechanisms based on the measured crack kinematics of the selected beams. The contribution is illustrated in Fig. 5.5.1, which shows the amount of shear carried by each mechanism for the specimens at the instant just before the opening of the secondary branch (taken as V_{cr}), this moment was identified using the DIC results. The experimental inclined cracking load V_{cr} is represented by the red line and it is compared to the sum of the vertical components of the calculated forces. This moment was selected since it has been found to be critical to the shear failure process and the decay of aggregate interlock forces and occurs earlier before the final failure.

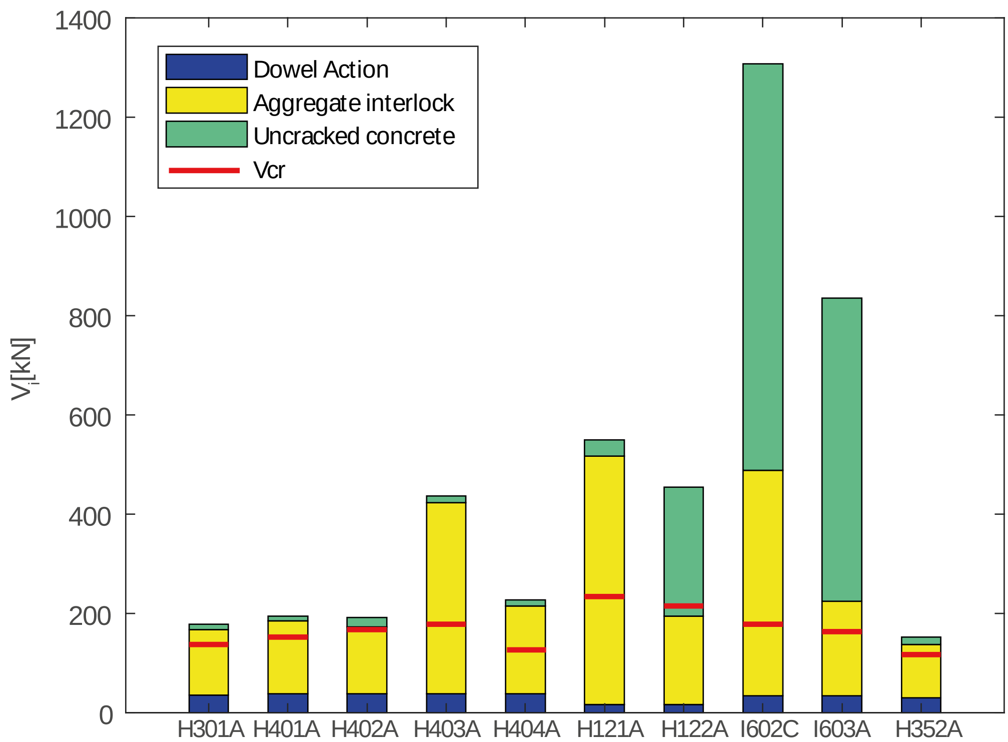

Fig. 5.5.1 Amount of calculated shear carried by each mechanism at the instant of the opening of the unstable crack compared to V_{cr}

As pointed out by Yang (2014), the effect of aggregate interlock predicted with Walraven's model overestimates the contribution and provides significantly higher shear forces than the shear measured during the test, that is why the calculated V_{cr} is always higher.

Table 5.5-1 shows the values of the calculated shear contribution and the comparison with the experimental V_{cr}. When a flexural shear failure is presented just after the formation of the critical shear crack (H301A, H401A, H402A, and H404A) the average ratio of the sum of the estimated contributions to the experimental V_{cr} is equal to 1.4, disregarding the specimen that developed dowel failure.

From these results two behaviors can be identified, one where the shear strength is governed by aggregate interlock and other where the governing mechanism is the arch action. In case the cases where aggregate interlock is governing, a contribution of up to 91% to the shear resistance was found. When the arch action is governing, the calculated capacity is significantly higher, reflecting the main contribution of the direct compressive strut and the increase in the shear capacity. The contribution from dowel action depends on the reinforcement configuration of the beams and it usually represents 20% of the shear resistance.

Another observation is that despite the final failure mode, the experimental values of V_{cr} are comparable for beams with the same properties.

Table 5.5-1 Amount of calculated shear contribution and comparison with V_{cr}

Test no.	V_{ai} [kN]	V_d [kN]	V_c [kN]	ΣVi [kN]	V_{cr} [kN]	$\Sigma Vi/V_{cr}$
H301A	75%	20%	6%	**177**	**131**	**1.4**
H401A	76%	20%	5%	**193**	**144**	**1.3**
H402A	71%	20%	10%	**191**	**171**	**1.1**
H403A	88%	9%	3%	**437**	**177**	**2.5**
H404A	78%	17%	5%	**226**	**127**	**1.8**
H121	91%	3%	6%	**549**	**234**	**2.3**
H122	39%	4%	57%	**454**	**215**	**2.1**
I602	35%	3%	63%	**1308**	**180**	**7.3**
I603	23%	4%	73%	**836**	**163**	**5.1**
H352	71%	20%	9%	**152**	**117**	**1.3**

5.6 Concluding remarks

Four different failure modes were observed during the experimental program: Flexural shear failure, flexural failure, shear compression, and dowel action. An analysis of the failures modes was presented based on the measured crack kinematics obtained from the DIC and in combination with constitutive models, the calculation of the contribution of each of the transfer mechanism was performed. Several remarks are drawn:

1) Regarding the crack kinematics and despite the final failure mode, the general observation is that the path that the critical shear crack will follow can be anticipated by observing the relative displacements: the cracks with the larger tangential displacements join to form the critical shear crack and the major crack with the larger displacements will develop to be the governing critical shear crack.
2) The contribution of aggregate interlock plays a decisive role during the failure process and it depends on the crack kinematics which directly depends on the crack profile. The steepest parts of the cracks, which are usually located at the top sections, present larger tangential displacements, thus the largest contribution of aggregate interlock is presented there.
3) When several flexural cracks develop in the shear span, the system can be related to a comb-like structure where the contribution of the compression zone is minimal, and the governing failure mechanism is aggregate interlock. This behavior is observed on beams that failed in flexural shear failure which can be attributed to the sudden loss of aggregate interlock.
4) Shear compression occurs when a direct compressive strut forms from the loading point to the support. In this case, the aggregate interlock is completely lost after the secondary branch along the longitudinal reinforcement reaches the support, however, the beam is able to increase its capacity because the governing mechanism is the arch action.
5) Specimens reinforced with plain bars were first tested with an *MV/d* ratio smaller than 3 and developed the critical shear cracked near the point of application of the load allowing the development of arch action, however, they presented a flexural failure (yielding of the reinforcement). Then, after the point

load was moved, they failed in flexural shear due to the loss of aggregate interlock and arch action.

6) Dowel failure was observed in the specimen with a reinforcement ratio of less than 0.4% and was found to be the most critical failure mode. In this case, the tensile reinforcement detached from the critical crack that was formed by the merge of the major crack and two secondary cracks. The development of the horizontal crack can be attributed to the dowel action which increased the displacements and reduced the force generated by aggregate interlock. This results in a relative plastic behaviour.

6 Improvements to the CSDT

In this section, some suggestions will be made with the aim of improving the Critical Shear Displacement theory, this will be based on the DIC results and the insights gained in Chapter 5. The analysis is focused on investigating the simplification of the crack pattern and on validating the kinematics proposed at failure.

6.1 Crack kinematics at failure

An important observation of the results presented in Chapter 5 was that despite the final failure mode the shear force at which the critical shear opens is comparable for the specimens with the same properties. This can be attributed to the kinematics presented at failure and hence to the behaviour of aggregate interlock.

In recent years, theoretical and experimental work (Yang, 2014; Cavagnis, Ruiz et al.,2017) have reported that shear behaviour of reinforced concrete members without shear reinforcement can be associated to the opening of a critical shear crack that leads to failure.

Among the physical models developed to assess the shear behaviour of reinforced concrete members without shear reinforcement, the CDST explicitly attributes the flexural shear failure to the unstable crack opening at the tensile reinforcement level. According to the model, the shear failure is triggered when the shear displacement (Δ) of a major flexural crack reaches the critical value Δ_{cr}. Since there is very limited information about the actual kinematics during the failure process, Yang (2014) derived the value of Δ_{cr} from a back analysis based on the test results from existing databases.

Considering the advantages of DIC, this section presents the results of the longitudinal and transverse crack openings of the critical shear cracks of the selected beams, the results are shown in Table 6.1-1. In the table w_m and Δ_m refer to the crack opening (w) and shear displacement (Δ) at the reinforcement level while w_m and Δ_m are taken at the mid-height of the beam. The results are of the critical shear crack when V/V_{cr}=1.

Table 6.1-1 Results of crack opening and shear displacement

Test no.	V_{cr} (kN)	w_b (mm)	Δ_b (mm)	w_m (mm)	Δ_m (mm)
H301A	136	0.77	0.88	0.60	1.05
H401A	143	0.22	0.91	0.91	1.42
H402A	173	0.32	0.94	0.60	0.99
H403A	142	0.21	0.70	0.81	1.26
H404A	158	0.30	0.76	0.46	0.61
H121A	237	0.15	0.40	0.40	0.66
H122A	191	0.13	0.44	0.47	1.47
I602C	174	0.45	0.76	0.38	1.06
I603A	157	0.29	0.61	0.54	0.99
H352A	117	0.21	0.77	0.18	0.28

6.1.1 Determination of critical moment

The results show that the values of w_b and Δ_b are equivalent for the beams with the same properties, however, the values of Δ_b are almost 20 times larger than the upper limit of the range proposed in CSDT (see Fig. 2.2.11).

It is important to note that the results were found to be quite sensitive to the level identified as the reinforcement since usually at this location several cracks develop close to each other and this can disturb the results regarding the relative displacements. For instance, specimen H401A was selected and the vertical displacements along the longitudinal axis of the beam were plotted at the reinforcement level and at a steep upper section, which was chosen based on the results found in Chapter 5 where it was concluded that the upper parts of the cracks are where the main contribution of aggregate interlock is locate. The results are shown in Fig. 6.1.1, it can be observed that the displacements at both levels present the same tendency with comparable relative displacements. Based on this finding, the results of crack width and shear displacements found from a section located at the top part of the crack profile (500 mm from the top fiber) are used to investigate the connection between the displacements and the failure process. The results from this analysis are shown in Fig. 6.1.2, Fig. 6.1.3 and Fig. 6.1.4, where Δ and w are plotted in combination with the aggregate contribution and the applied shear force for beams H401A, H403A and H122A.

In Fig. 6.1.2 through Fig. 6.1.4, the general observation is that regarding the development of w, it becomes more or less stable with the increase of load level. In contrast to Δ, which is unstable and presents an increase in the values as the load level increases.

In these figures, the sudden decay of aggregate interlock forces is attributed to the triggered of the shear displacements and correspond to the opening of the secondary branches approaching the support at the reinforcement level and the point load. In the figures, the red dash line represents the moment when aggregate interlock forces suddenly decay, at this point the applied shear forces were in average 94% of V_{cr} and the shear displacements are comparable independent of the final failure at around 1 mm. This observation supports the assumption proposed by Yang (2014) that the flexural shear failure occurs when the shear displacement reaches a critical value. However, the values of Δ_{cr} are again significantly larger than the values from Eq. (2.22). This difference can be attributed to the simplification of the crack path.

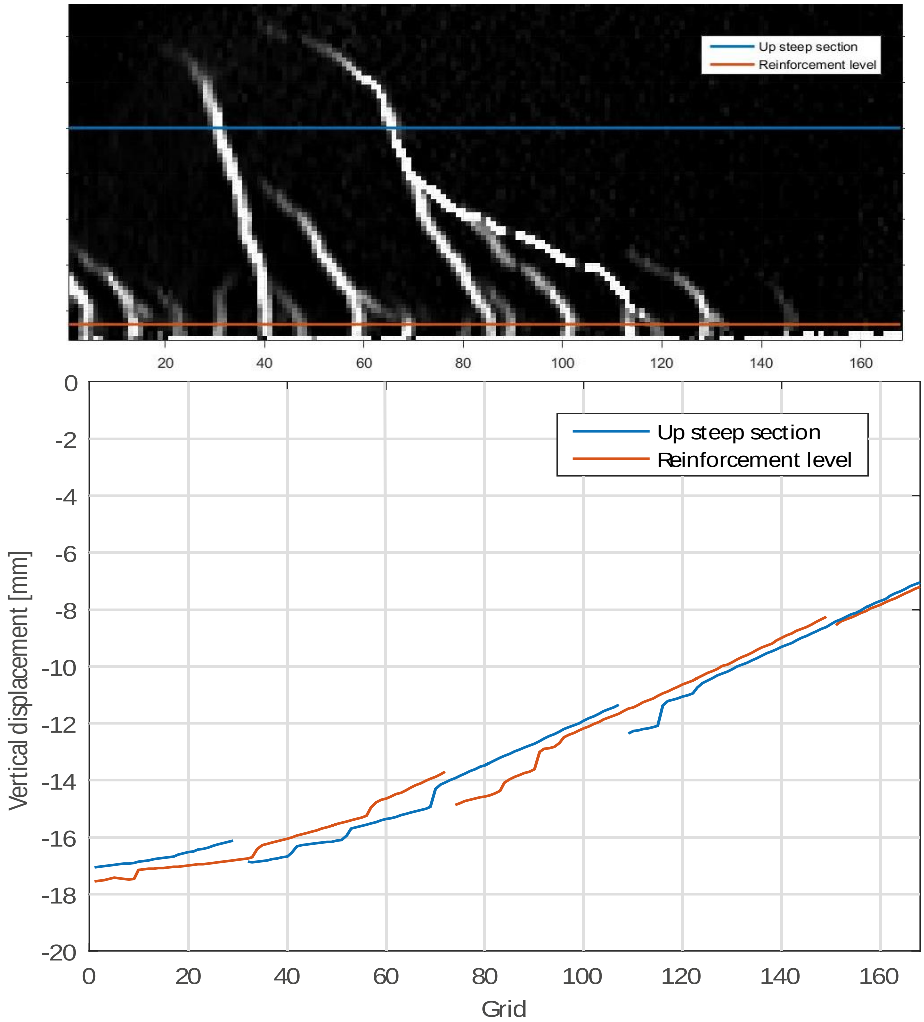

Fig. 6.1.1 Location of levels (Up) and vertical displacement along the longitudinal axis (Down) for specimen H401A

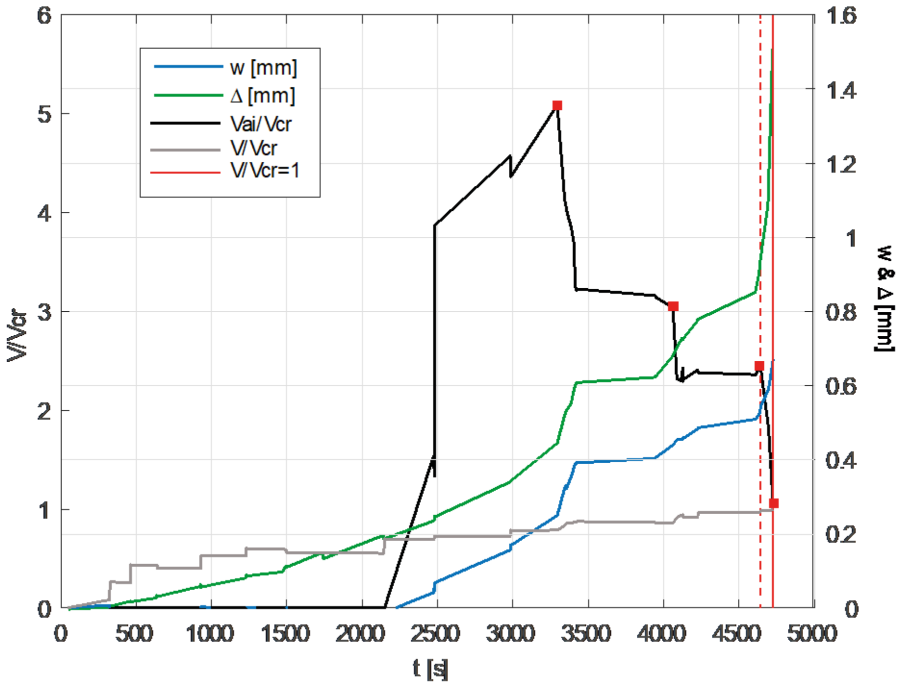

Fig. 6.1.2 Aggregate interlock, crack width and shear displacement vs time for beam H401A

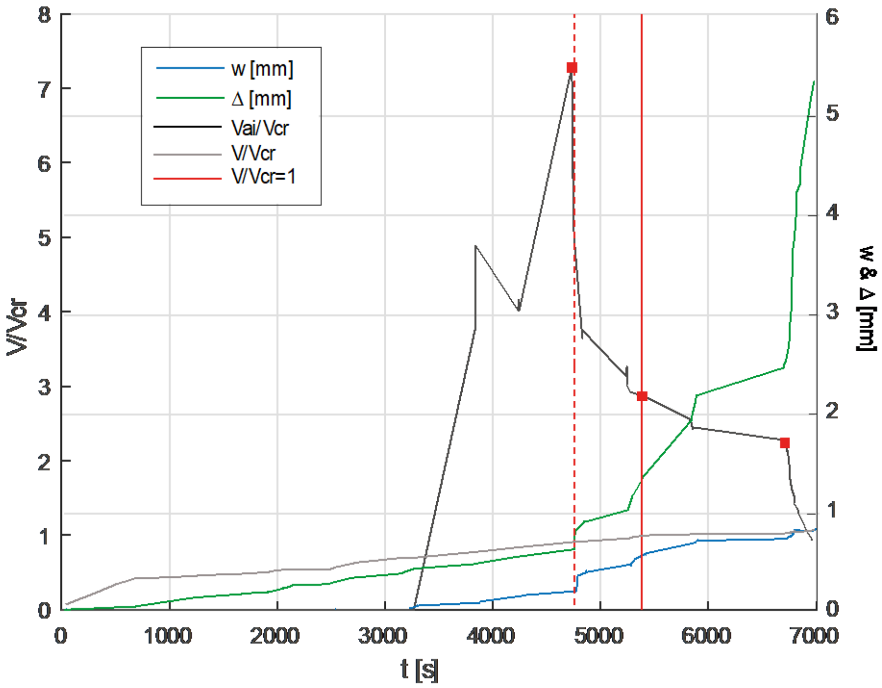

Fig. 6.1.3 Aggregate interlock, crack width and shear displacement vs time for beam H403A

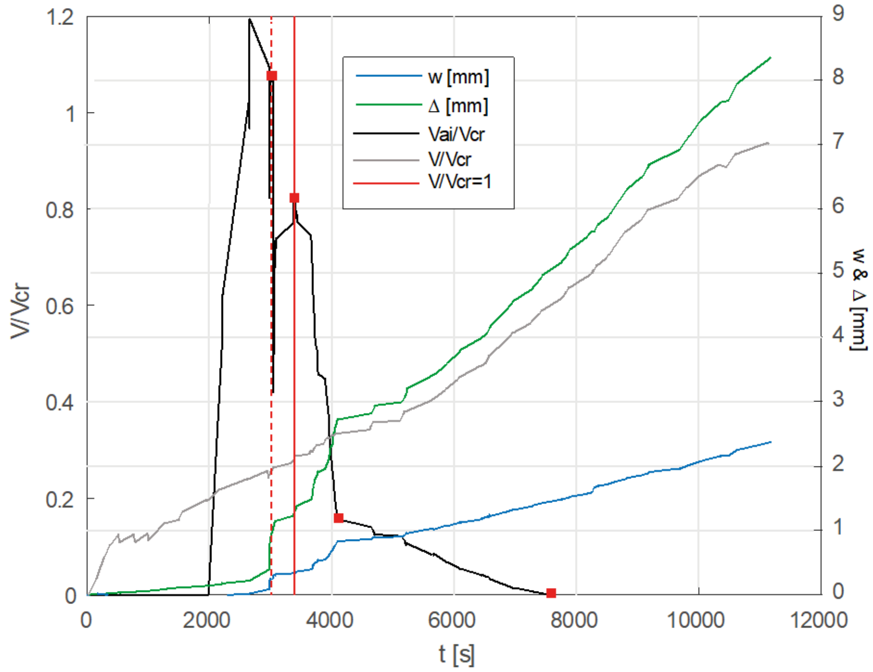

Fig. 6.1.4 Aggregate interlock, crack width and shear displacement vs time for beam H122A

6.2 Crack angle

An important assumption of the CSDT (Yang, 2014) is the crack pattern, which is simplified to two straight lines where the main part of the crack is taken as a straight line at 90º. To improve this simplification, the angles of the flexural cracks found in the specimens were computed and plotted in Fig. 6.2.1 against x_0/d, where x_0 refers to the distance taken from the support to the root of the crack.

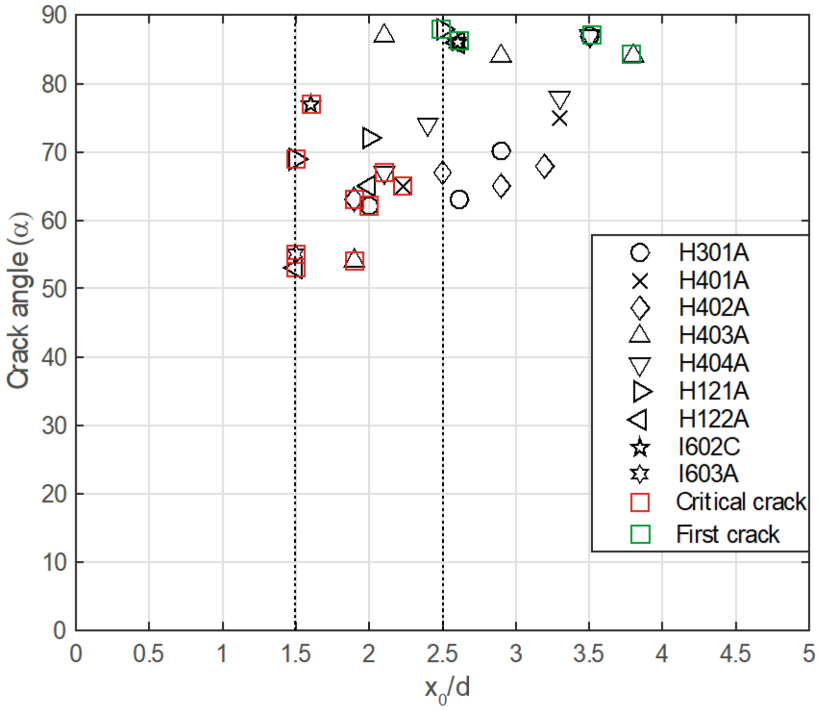

Fig. 6.2.1 Angle of cracks vs x_0/d

This figure shows that the first flexural crack, which is usually located near the point load, has a crack angle that can be approximated to 90º. On the other hand, the critical cracks, which are located in a range between 1.5 and 2.5 x_0/d, present an angle that is in a range between 53º and 75º.

Table 6.2-1 shows a summary of the results from the crack angles for the major cracks. In the table, α denotes the crack angle, α_m refers to the average angle of the major cracks and α_{cr} indicates the angle of the critical inclined crack. $l_{cr,m}$ refers to the crack spacing of the major crack taken at mid-height and x_{cr0} is the distance taken from the support to the root of the critical inclined crack.

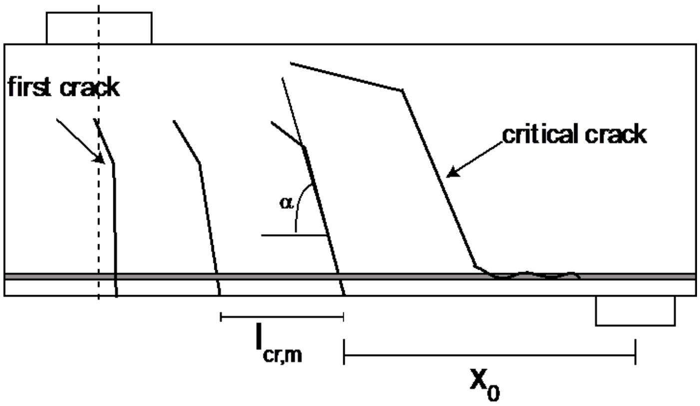

Fig. 6.2.2 Definition of crack angle and distance x_0

Table 6.2-1 Summary of crack angles and distances

Test no.	MV/d	α first flexural crack	α_m	$l_{cr,m}/d$	α_{cr}	x_{cr0}/d
H301A	3.45	87º	65º	0.42	**62º**	**2.0**
H401A	3.88	-	70º	0.50	**65º**	**2.2**
H402A	3.88	-	66º	0.44	**64º**	**2.5**
H403A	3.88	84º	75º	0.40	**54º**	**1.9**
H404A	3.45	87º	73º	0.79	**67º**	**2.1**
H121A	2.60	88º	71º	0.47	**69º**	**1.5**
H122A	2.60	86º	59º	0.47	**53º**	**1.5**
I602C	2.59	86º	77º	0.81	**74º**	**1.6**
I603A	2.59	86º	86º	0.57	**55º**	**1.5**

6.3 Conclusions

In this chapter, the results from DIC and Chapter 5 were used to investigate some of the assumptions made in the CSDT. The simplification of the crack angle was analyzed based on the crack patterns found on the experimental program and the proposed kinematics at failure were validated. From these, some conclusions can be drawn:

1) The simplification of the crack profile should be modified to allow major displacements. It is suggested to be changed to a crack at an angle of a range between 60º and 70º.
2) The crack spacing between major flexural cracks is in a range between 0.4d and 0.8d.
3) The values of Δ_{cr} are significantly larger than the calculated with Eq. (2.22).

The failure mechanism was validated since it was observed that the flexural shear failure occurs when the shear displacement of a major crack reaches a critical value triggering the development of the secondary branches and this is directly related to the decay of the contribution of aggregate interlock stresses.

7 Conclusions and recommendations

An analysis of the failure modes observed in the experimental program was presented based on the DIC measurement. With the measured crack pattern and kinematics, the contribution of the various shear transfer mechanisms was calculated based on known constitutive laws. With the insights gained some improvements to CSDT were proposed. The concluding remarks from this research are presented in this chapter. In addition, some topics that were left out due to the limitation of time are suggested as a future line of research.

7.1 Conclusions

After analyzing the results presented in the previous chapter, the following conclusions can be drawn:

- The displacement field obtained by DIC is able to provide reasonable accuracy since when compared to the LVDT readings a maximum difference of 0.1mm was found.
- The DIC kinematic measurements in combination with the constitutive laws and the methodology considered in this thesis lead to a reasonable explanation of the observed failure modes. A comparison between the experimental results and the sum of the calculated contributions yield a reasonable agreement, with an error of 40% when the flexural shear failure is presented just after the formation of the flexural shear crack.
- The aggregate interlock plays a major role during the failure process, a sudden drop of aggregate interlock usually leads to the failure of the structure or shift of the main load carrying mechanism. Its contribution is mainly concentrated at the steepest parts of the cracks (usually located at the top sections).
- In the case of flexural shear failure, the governing mechanism was aggregate interlock. Its contribution during the loading procedure was found to be up to 90% of the shear strength. The failure was attributed to the loss of aggregate interlock when a sudden increase of the shear displacement of the critical shear crack is observed. However, such decrease occurs earlier before the actual shear failure occurs. Therefore, the actual shear failure mechanism should be studied at an earlier stage.
- When a shear compression failure occurred, the contribution from aggregate interlock was lost when the flexural shear crack opened but the beam was able to carry a higher load because of arch action. However, when the point load is moveable. The arch action is not reliable.
- The contribution from dowel action depends mostly on the reinforcement of the beam. Dowel failure is the most critical failure mode presented in this test series, it is obtained for members with a reinforcement ratio less than 0.4% and it is defined by the opening of the secondary branch of a major flexural crack along

the tensile reinforcement. The development of the dowel cracking results in a relative plastic behaviour with large shear displacements.

- Two simplified assumptions of CSDT were verified by the test results. They are the crack inclination and the critical shear displacement. It is concluded that the simplified crack profile suggested by CSDT should be changed to a crack with an angle between 60º and 70º to allow for larger displacements. The values of Δ_{cr} found in this research are up to 20 times higher than the proposed in the CSDT. The failure criterion assumed in the CSDT was validated, it was demonstrated that an increase of the shear displacement Δ is critical to triggering the shear flexural failure.

7.2 Recommendations

Some recommendations that can be interesting for further study are:

- It would be useful to improve the post-processing of the data obtained from the DIC in terms of simplicity of the program and develop a better algorithm to filter the cracks.
- Real-time display of the displacements and strains on live image would be useful, thus some improvements to the DIC algorithm could be implemented to show real-time measurements during the testing of the specimens.
- This project reveals that some of the simplifications suggested by the CSDT are not consistent with the experimental observations. They are the crack inclination and the value of the critical shear displacement. This input can be used as a starting point to develop a simple kinematic model which is consistent with the Critical Shear Displacement theory, where the recommendations are implemented.
- Although the failure process of the newly observed dowel failure was explained phenomenologically, a mechanical model would be more helpful for the engineering practice. A suggestion of such model is given in Fig. 7.2.1. In such model, rotation of the crack is assumed at the crack tip of the major crack. The contribution of aggregate interlock can be neglected, and the dowel action can be assumed to be constant. The failure process could be modeled relating the shear displacement with propagation of the dowel crack and the rotation as illustrated in the following figure:

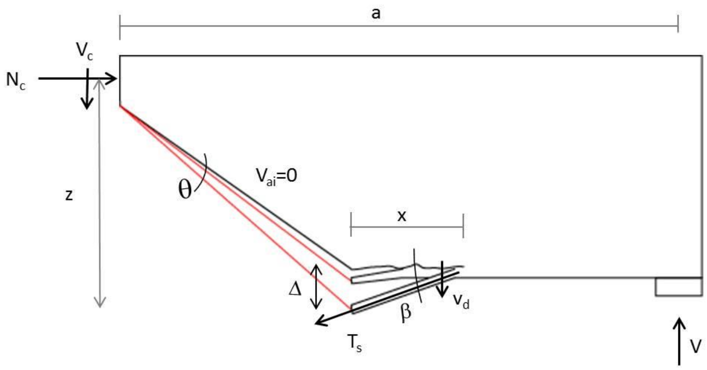

Fig. 7.2.1 Proposed dowel failure model

- A study on the influence of the crack trajectory to the shear capacity of aggregate interlock could provide a better understanding of the fact that comparable shear capacities are found with different crack patterns.

Appendix A

In this appendix, the results from additional beams are presented.

H402A

A special case was beam H402A, where the critical shear crack was formed by the merged of three major cracks. The analysis from the main results showed that in general, the major crack with the larger tangential displacements will develop to be the critical shear crack. Fig. A 2 presents the results from the development of Δ for the four major cracks, for comparison, the shear force is also plotted and the DIC strain distributions are shown in Fig. A 1. It can be observed that at the reinforcement level the crack with the larger shear displacements is Crack 3 but at the top section is Crack 2. The measurements of relative displacements show that before the opening of the shear crack large aggregate interlock stresses could be activated at the mid-section of the beam (see Fig. A 3), as a result, the horizontal crack joining the major cracks 2 and 3 suddenly developed. At that moment, the aggregate interlock forces dropped, and failure was triggered by the sudden development of the secondary branches.

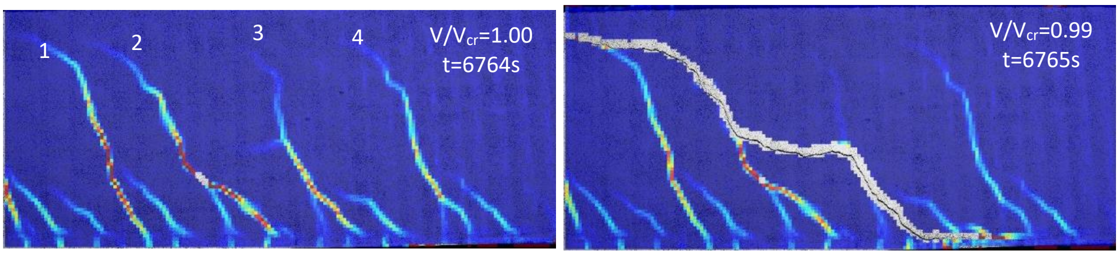

Fig. A 1Stain distributions at representative load levels for beam H402A

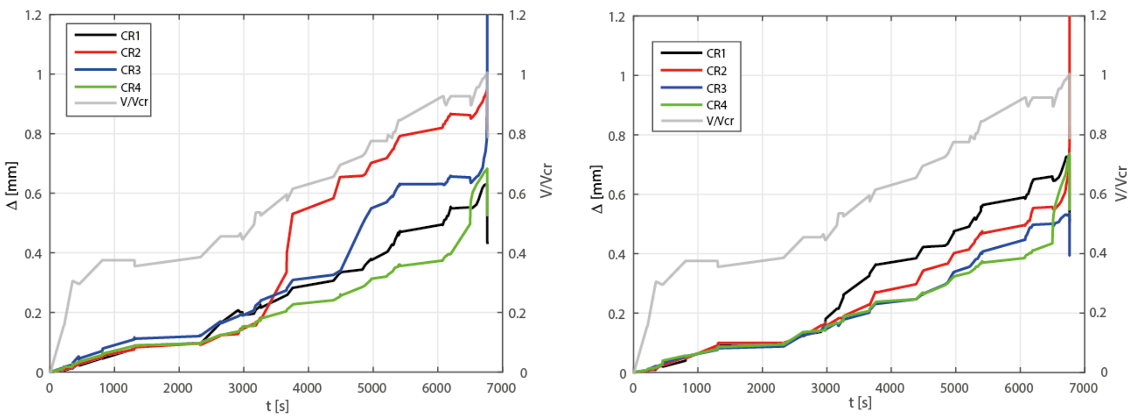

Fig. A 2 Shear displacement for H402A at reinforcement level (Left) and upper section of crack (Right)

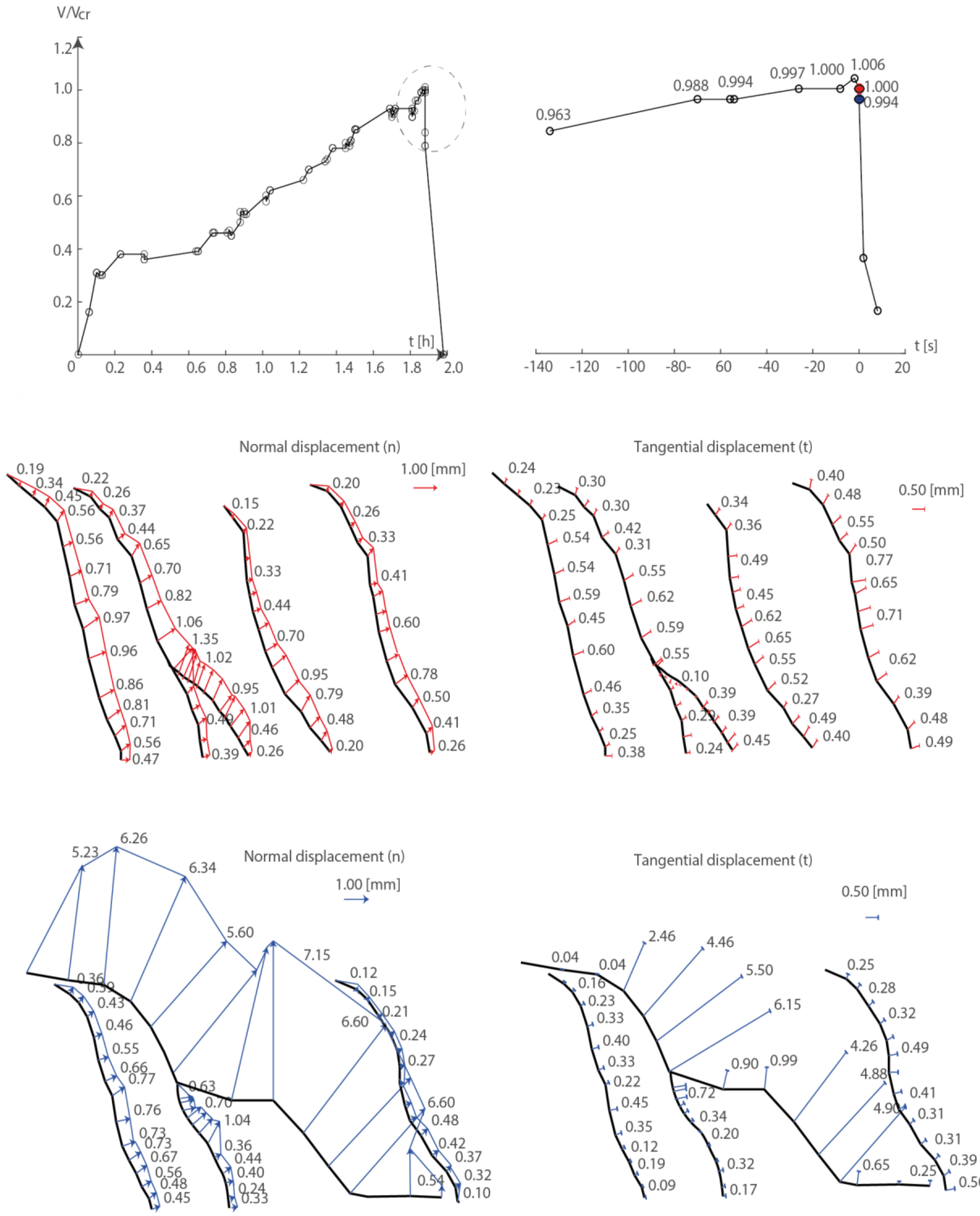

Fig. A 3 Loading procedure (up) and development of normal (left) and tangential displacements (right) for beam H402A

I123A

The loading protocol for specimens I123A was determined to implement acoustic emission (AE), which is a measurement technique to monitor the acoustic signals emitted during the loading process. The results from AE are out of the scope of this project, however, the DIC results will be presented. This specimen was reinforced with plain bars and had a reinforcement ratio of 1.14% (8Φ25). Fig. A 4 shows the loading procedure and the moments of the photo shooting.

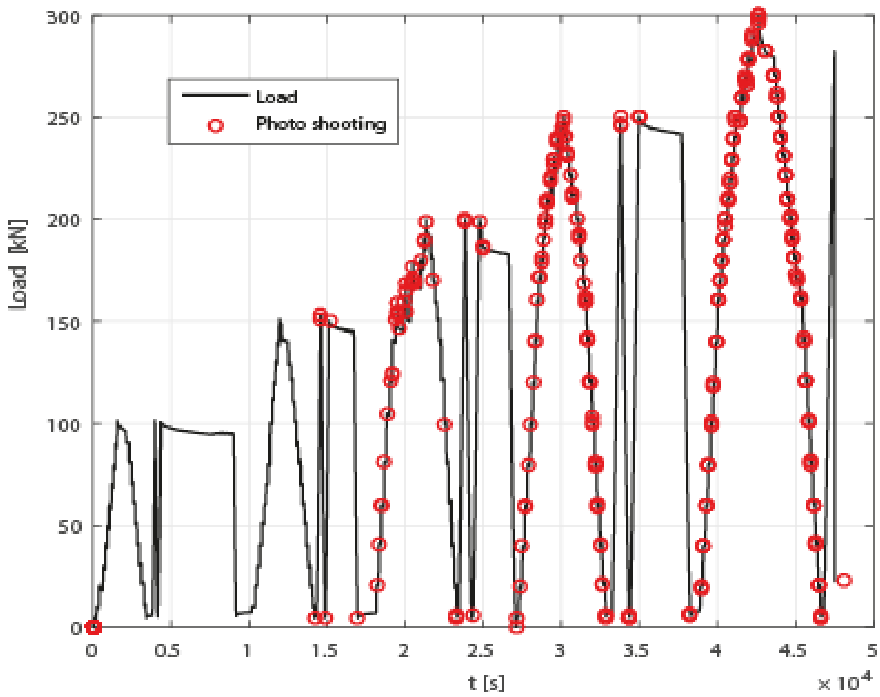

Fig. A 4 Loading scheme (applied load vs time) and the moment of the photo shooting for test I23A

In Fig. A 5 the crack width and the shear displacements at a height equal to 590 mm from the top fiber are plotted, for comparison, the loading procedure is also given. It can be observed that Crack 4 presented larger shear displacements. Fig. A 6 shows the results of the crack width and shear displacement for the critical crack as well as the loading protocol. The strain distributions obtained from the DIC at the representative load levels are given in Fig. A 7. It can be observed that the point where the maximum shear displacements are presented corresponds to the beginning of the opening of the unstable crack along the tensile reinforcement.

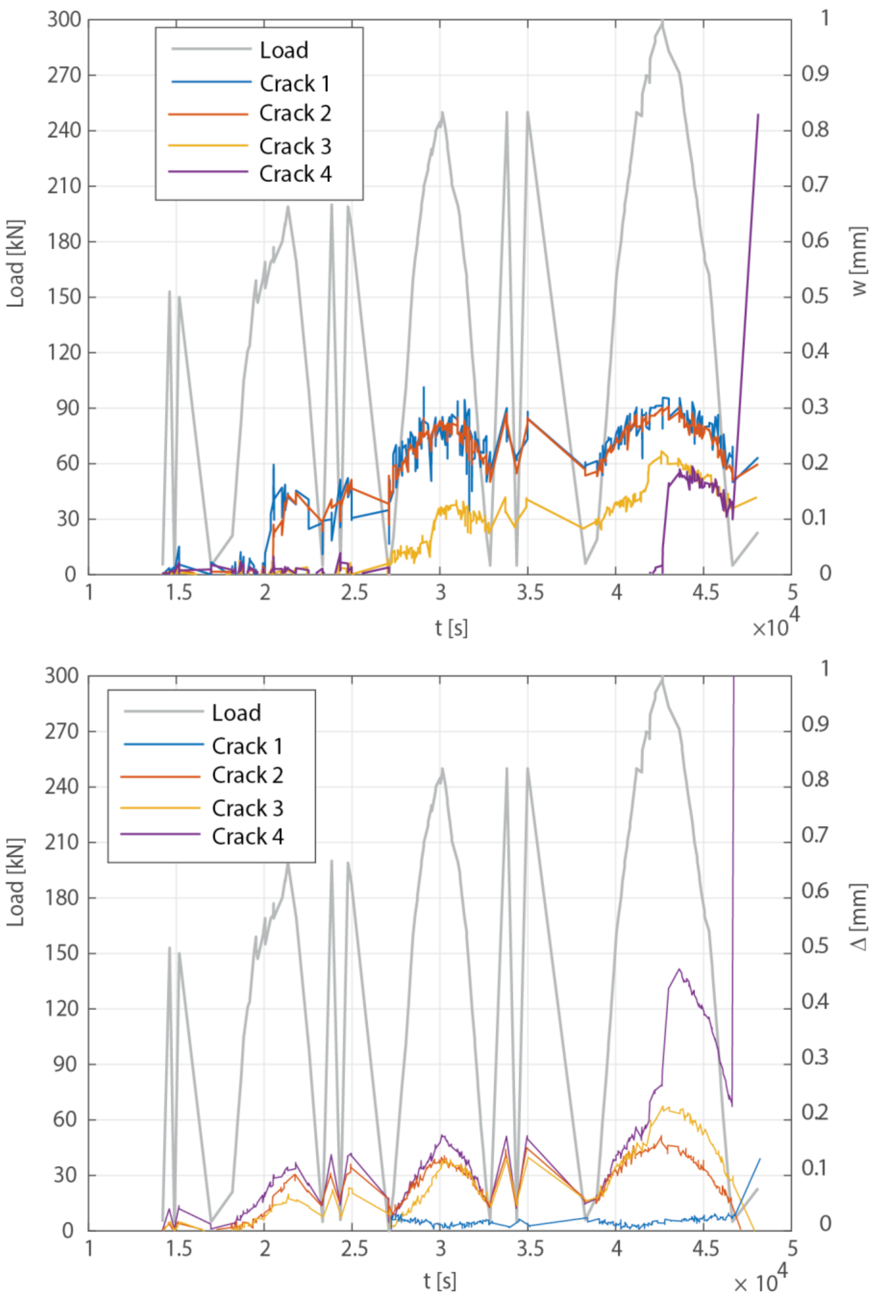

Fig. A 5 Crack width (up) and shear displacement (down) vs time for beam I123A

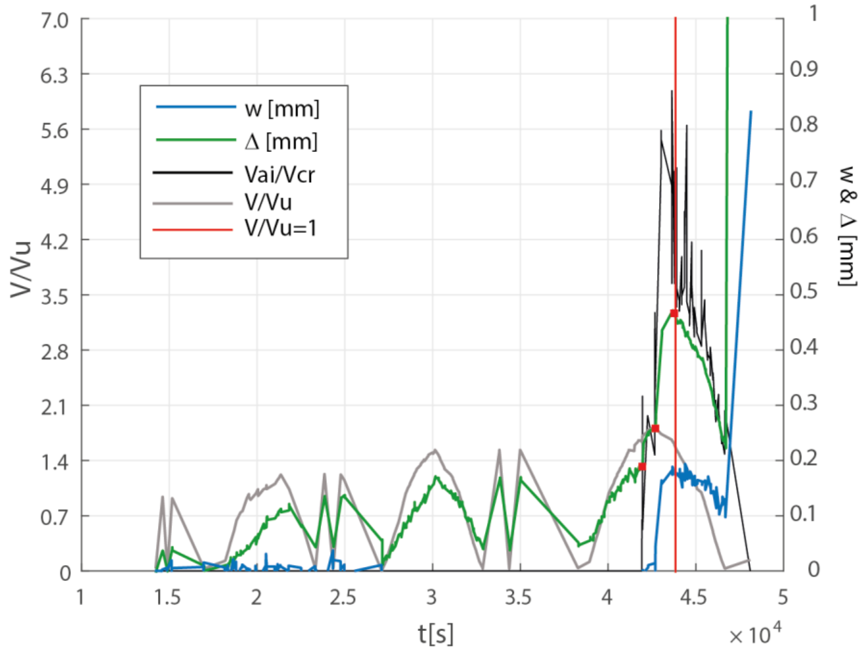

Fig. A 6 Aggregate interlock, crack width and shear displacement vs time for critical crack

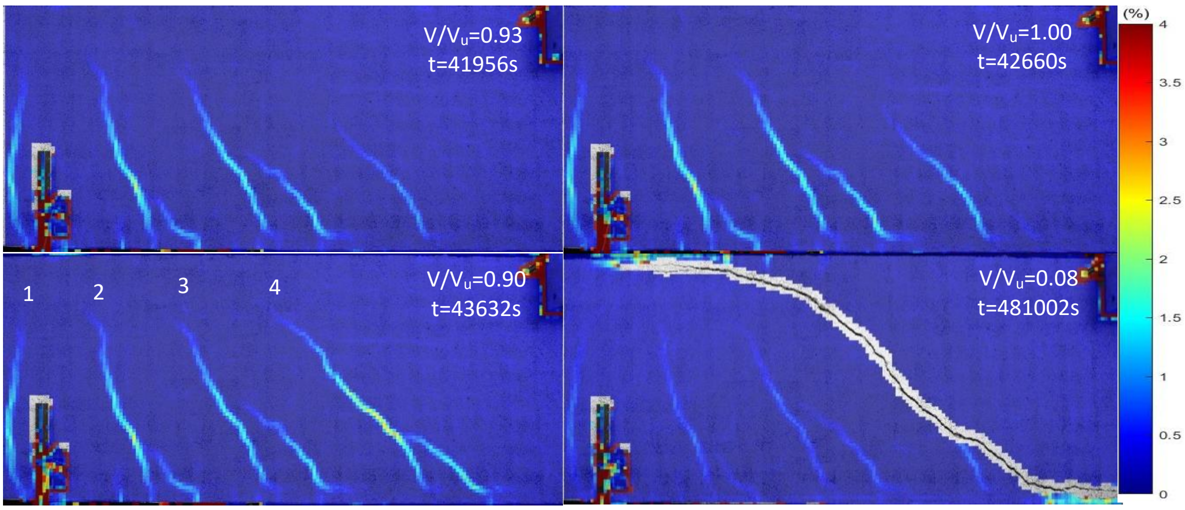

Fig. A 7 Strain distribution at representative load levels for beam I123A

References

ACI Commitee 437. (2013). Code Requirements for Load Testing of Existing Concrete Structures (ACI 437.2 M-13) and Commentary. 24. Farmington Hills, MA.

AN-1701, C. A. (n.d.). Speckle pattern fundamentals.

Bauman, T. a. (1970). Versuche zum studien del verd¨belungswirkung der biegezugbewehrung eines stahlbetonbalkens [Experimental study on dowel action in reinforced concrete beams]. *Deutscher Ausschuss für Stahlbeton (DAfStb)*.

Bentz, E., Vecchio, F., & Collins, M. (2006). Simplified Modified Compression Field Theory for Calculating Shear Strength of Reinforced Concrete Elements. *Structural Journal*, *103*(4).

Campana, S., Férnandez Ruiz, M., Anastasi, A., & Muttoni, A. (2013). Analysis of shear-transfer actions on one-way RC members based on measured cracking pattern and failure kinematics . *Magazine of Concrete Research*.

Cavagnis, F., Fernández Ruiz, M., & Muttoni, A. (2017). An analysis of the shear-transfer actions in reinforced concrete members without transverse reinforcement based on refined experimental measurements. *Structural concrete*, 1-16.

Evans, R., & Marathe, M. (1968). Microcracking and stress-strain curves for concrete in tension. *Materials and Construction, 1*(1), 61-64.

Fenwick, R., & Pauley, T. (1968). Mechanism of Shear resistance of Concrete Beams. *Journal of the Structural Division, 94*(10), 2325-2350.

Fernández Ruiz, M., Muttoni, A., & Sageseta, J. (2015). Shear strength of concrete members without transverse reinforcement: A mechanical approach to consistently account for size and strain effects. *Engineering Structures*, *99*, 360-372.

Friberg, B. (1940). Design of dowels in transverse joints of concrete pavements. *Transactions*, 105:1076-116.

Gambarova, P., & Karakoc, C. (1983). A new approach to the analysis of the confinement role in regularly cracked concrete elements. *Transactions of the 7. international conference on structural mechanics in reactor technology, H*, 251-261.

Gustafsson, P., & Hillerborg, A. (1988). Sensitivity in Shear Strength of Longitudinally Reinforced Concrete Beams to Fracture Energy of Concrete. *ACI Structural Journal*, *85*(3).

Hillerborg, A., Modéer, M., & Petersson, P.-E. (1976). Analysis of crack formation and crack growth in concrete by means of fracture mechanics and finite elements. *Cement and Concrete Research, 6*(6), 773-781.

Hordijk, D. (1991). Local Approach to Fatigue of Concrete. Delft: Delft University of Technology.

Houde, J., & Mirza, M. S. (1974). A finite element analysis of shear strength of reinforced concrete beam. (A. C. Institute, Ed.) *ACI Special Publication , 42*(1), 103-128.

Huber, P., Huber, T., & Kollegger, J. (2016). Investigation of the shear behavior of RC beams on the basis of measured crack kinematics. *Engineering Structures, 113*, 41-58.

Jenq, Y., & Shah, S. (1990). Shear Resistance of Reinforced Concrete Beams--A Fracture Mechanics Approach. *ACI Special Publication, 118*.

Jones, E. (2015). Documentation for Matlab-based DIC code. Urbana-Champaign: University of Illinois.

Kani, G. (1964). The Riddle of Shear Failure and Its Solution. *64(3)*, 441-467. ACI Journal.

Keuser, W., & Walraven, J. (1989). Fracture of Plain Concrete Under Mixed Mode Conditions. *Proceedings of Recent Developments in the Fracture of Concrete and Rock*, 625-634.

Koekkoek, R., & Yang, Y. (2016). *Measurement Report on the transition between flexural and shear failure of RC beams without shear reinforcement.* Delft University of Technology.

Krefeld, W., & Thurston, C. (1966). Contribution of longitudinal steel to shear resistance of reinforced concrete beams. *ACI Journal Proceedings*, *63*(3), 325-344.

L Reu, P., Sutton, M., Wang, Y., & J Miller, T. (2009). *Uncertainty quantification for digital image correlation.*

Marti, P. (1985). Basic tools of reinforced concrete beam design. *ACI Journal*, *82*, 46-56.

Mihaylov, B. (2014). Five-spring model for complete shear behaviour of deep beams. *Structural concrete, 16*(1), 71-83.

Mihaylov, B., Bentz, E., & Collins, M. (2013). Two-Parameter Kinematic Theory for Shear Behavior of Deep Beams. *ACI Structural Journal*, *110*(3), 447-455.

Mihaylov, B., Bentz, E., & Collins, M. (2013). Two-Parameter Kinematic Theory for Shear Behavior of Deep Beams. *Structural Journal*, *110*(3).

Mihaylov, B., Hannewald, P., & Beyer, K. (2016). Three-Parameter Kinematic Theory for Shear-Dominated Reinforced Concrete Walls. *Structural Engineering, 142*(7).

Mörsch, E. (1909). Der Eisenbetonbau [Concrete-steel construction]. *Engineering News Publishing*.

Muttoni, A. (2008). Punching Shear Strength of Reinforced Concrete Slabs without Transverse Reinforcement. *Structural Journal, 105*(4).

Muttoni, A., & Fernández Ruiz, M. (2008). Shear strength of members without transverse reinforcement as function of critical shear crack width. *ACI Structural Journal, 105*(2), 163-175.

Muttoni, A., & Fernández Ruiz, M. (2008). Shear strength of members without transverse reinforcement as function of critical shear crack width. *ACI Structural Journal, 105*(2), 163-175.

Muttoni, A., & Schwartz, J. (1991). Behavior of Beams and Punching in Slabs without Shear Reinforcement. *IABSE Colloquium, 62*, 703-8.

Pan, B., Qian, K., Xie, H., & Asundi, A. (2009). Two-dimensional digital image correlation for in-plane displacement and strain measurement: a review. *Measurement Science and Technology, 20*(6).

Pan, B., Xie, H., Guo, Z., & Hua, T. (2007). Full-field strain measurement using a two-dimensional Savitzky-Golay digital differentiator in digital image correlation. *Optical Engineering, 46*.

Pan, B., Xie, H., Wang, Z., Qian, K., & Wang, Z. (2008). Study on subset size selection in digital image correlation for speckle patterns. *Opt. Express, 16*, 7037-7048.

Paulay , T., Park, R., & Phillips , M. (1974). Horizontal construction joints in cast in place reinforced concrete. *ACI Special Publications 42, 51*, 599-616.

Reineck, K.-H. (1991). Ultimate Shear Force of Structural Concrete members without Transverse Reinforcement Derived from a Mechanical Model. *88(5)*, 867-875. ACI Structural Journal.

Schlaich, J., Schafter, I., & Jennewein, M. (1987). Towards a consistent design of structural concrete. *PCI Journal, 32*, 74-150.

Sherwood, E., Bentz, E., & Collins, M. (2007). Effect of Aggregate Size on Beam-Shear Strength. *ACI Structural Journal, 104*(2).

Soroushian , P., Kienuwa , O., & Maximo, C. (1987). Bearing Strength and Stiffness of Concrete Under Reinforcing Bars. *Materials Journal, 84*(3).

Stahlbeton, D. A. (2000). DAfStb-Guideline:Load tests on concrete structures. 7. Deutscher Ausschuss für Stahlbeton.

Taylor, H. (1969). *Investigation of the Dowel Shear Forces Carried by the Tensile Steel in Reinforced Concrete Beams.* London: Cement and Concrete Association.

Taylor, H. (1974). The Fundamental Behavior of Reinforced Concrete Beams in Bending and Shear. *ACI Special Publication, 42*.

Transportation Research Board. (2006). *Simplified Shear Design of Structural Concrete Members: Appendixes.* Washington, D.C.: The National Academies Press. doi:10.17226/13555

Tung, S., Shih, M., & Sung, W. (2008). Development of digital image correlation method to analyze crack variations of masonry wall. *Sadhana*.

Vecchio, F., & Collins, M. (1986). The modified compression-field theory for reinforced concrete elements subjected to shear. *ACI J. Proc.*(2), 219-231.

Vintzeleou, E., & Tassios, T. (1986). *Mathematical models for dowel action under monotonic and cyclic conditions* (Vol. 38:134). Magazine of Concrete Research.

Walraven, J. (1978). *Mechanisms of Shear Transfer in Cracks in Concrete- A Survey of Literature* (Vols. Report 5-78-12). Stevin Laboratory: Delft University of Technology.

Walraven, J. C. (1981). Fundamental analysis of aggregate interlock. *J.Struct. Eng.*(107(ST11)), 2245-2270.

Yang, Y. (2014). *Shear Behaviour of Reinforced Concrete Members without Shear Reinforcement, A New Look to at an Old Problem.* Delft: Ph.D. Thesis.

Yang, Y. (2016). Transition between flexural and shear failure on RC members without shear reinforcement. TU Delft.

Yang, Y., den Ujil, J., & Walraven, J. (2012). Shear capacity of reinforced concrete beams under complex loading conditions. *Proc. 9th Fib Int. Ph.D. Symp. Karlsruhe Institute of Technology*, 43-48.

Yang, Y., den Ujil, J., & Walraven, J. (2016). Critical shear displacement theory: on the way to extending the scope of shear design and assessment for members without shear reinforcement.

Yang, Y., van der Veen, C., Hordijk, D., & de Boer, A. (2016). The shear capacity of reinforced concrete members with plain bars. *Structural Faults and Repair 2016*.

Yang, Y., Walraven, J., & Den Uijl, J. (2016). Shear Behavior of Reinforced Concrete Beams without Transverse Reinforcement-Based on Critical Shear Displacement. *Journal of Structural engineering, 04016146*, 1-13.

Zarate Garnica, G., & Yang, Y. (2018). *Measurement report on the shear behaviour of 1.2m deep RC slab strips.*